UNIVERSITÀ DEGLI STUDI DI PADOVA

Dipartimento di Ingegneria Elettrica

Scuola di Dottorato di Ricerca in Ingegneria Industriale
Indirizzo Energetica
Ciclo XXII

PASSIVE PROTECTIONS AGAINST BREAKDOWN EFFECTS IN NEUTRAL BEAM INJECTION DEVICES FOR NUCLEAR FUSION EXPERIMENTS

Direttore della Scuola: Ch.mo Prof. Paolo Bariani

Coordinatore di Indirizzo: Ch.mo Prof. Alberto Mirandola

Supervisore: Ch.mo Prof. Giorgio Rostagni

Tutor: Dott. Ing. Antonio De Lorenzi

Dottorando: Alberto Pesce

01 Febbraio 2010

We are not what we think we are,
but what we think, we are.

"Rovering to success"
Sir Robert Baden-Powell Lord of Gilwell

Per Elisa

Contents

Sommario

L'esigenza di nuove tecnologie per la produzione di energia, compatibili con l'ambiente, e le normative sulle emissioni di anidride carbonica stanno spingendo la ricerca sulla fusione nucleare come possibile alternativa futura.

Da questo punto di vista il prossimo esperimento in via di costruzione in Francia, ITER (acronimo di *International Thermonuclear Experimental Reactor*, frutto di una collaborazione internazionale tra Unione Europea, Giappone, Russia, India, Cina, Corea del Sud e Stati Uniti d'America), dovrà dare delle risposte sull'effettiva fattibilità della fusione nucleare, e in particolare sul controllo della stabilità di plasma per lunghi tempi e ad alte temperature, sulla possibilità di funzionamento in regime stazionario e sull'effettivo raggiungimento della temperatura di fusione.

Uno dei dispositivi necessari per il riscaldamento del plasma è l'iniettore di neutri, concetto sviluppato già in diverse macchine operanti fino ad oggi. Il principio è semplice: si tratta di "bombardare" il plasma con un fascio di atomi neutri (quindi insensibili ai forti campi magnetici presenti) ad alta energia cinetica in modo da trasferire mediante collisioni l'energia agli ioni del plasma stesso. Nel contempo il fascio aiuta anche il sostenimento della corrente di plasma, necessaria per il confinamento nella camera di scarica in configurazione "tokamak".

Le prestazioni ingegneristiche richieste all'iniettore di neutri di ITER sono molto gravose, sia dal punto di vista delle sollecitazioni meccaniche e termiche che da quelle elettriche. In particolare, la potenza del fascio di atomi neutri richiesto è di 16.5 MW mentre l'energia di accelerazione del fascio di ioni negativi di deuterio o idrogeno, a monte della neutralizzazione, è di 1 MeV. La tensione di accelerazione corrispondente è perciò di 1 MV.

Uno dei punti più critici dell'intero sistema è dato dalle condizioni operative molto vicine ai limiti di scarica per le griglie di accelerazione, tanto che la scarica stessa non è considerata un fenomeno di guasto bensì una normale condizione di funzionamento del sistema.

Il lavoro esposto in questa tesi di dottorato, svolto principalmente presso il Consorzio RFX, si inserisce in questo contesto. In particolare vengono analizzati gli effetti dell'arco tra le griglie sia in termini di energia d'arco depositata sulle griglie stesse che dei transitori di tensione e corrente che si propagano nei vari punti del sistema. Riguardo all'energia d'arco, essa dev'essere limitata al di sotto di un certo valore per evitare il danneggiamento irreversibile delle griglie stesse con conseguente decondizionamento del sistema, perdita delle proprietà di tenuta della tensione e quindi il verificarsi della scarica a tensioni più basse. I transitori di tensione invece possono essere dannosi, sia perché possono

indurre sovratensioni in punti delicati del sistema con conseguente perdita dell'isolamento, sia perché sono fonte di disturbi elettromagnetici (EMI) per le varie apparecchiature diagnostiche presenti, legati alle alte frequenze in gioco dell'ordine dei MHz.

Vengono in questa sede proposte alcune soluzioni progettuali per limitare tali effetti, corroborate da opportune simulazioni circuitali o da validazione sperimentale. I dispositivi esposti sono alternativi a quelli fino ad oggi impiegati, presentando una strategia d'insieme per la protezione. In più, sono di tipo passivo in quanto devono intervenire istantaneamente al verificarsi della scarica per poter essere efficaci, contrariamente alle protezioni attive che necessitano di un certo tempo di intervento legato all'acquisizione di un segnale comprovante la scarica. La tesi è articolata nel modo seguente.

Nel *capitolo 1* viene introdotto l'iniettore di neutri di ITER nell'ambito delle ricerche sulla fusione nucleare; ne vengono descritti schematicamente i principi di funzionamento e i componenti principali. Infine viene presentata l'installazione sperimentale in via di costruzione a Padova, costituita da due esperimenti, ovvero una sorgente di ioni negativi in scala 1:1 rispetto a quella di ITER, con un unico stadio di accelerazione del fascio a -100 kV, e un iniettore vero e proprio, identico a quello che verrà installato su ITER.

Il *capitolo 2* presenta dapprima le condizioni operative previste per l'iniettore di neutri dal punto di vista elettrico. In particolare vengono introdotte le problematiche della tenuta alla tensione e del processo di condizionamento in vuoto; quindi viene descritta una possibile modellazione circuitale per l'arco elettrico su lunghe distanze, considerando il fenomeno dell'irraggiamento come preponderante per la dissipazione dell'energia d'arco. Infine vengono presentate le attuali soluzioni contro gli effetti della scarica, ovvero uno snubber magnetico concentrato alle estremità della linea di trasmissione dell'iniettore e le protezioni di tipo attivo.

Nel *capitolo 3* vengono introdotti due nuovi concetti di protezioni passive. Il primo è un resistore di smorzamento che collega l'ultima griglia di accelerazione del fascio di ioni (la griglia di terra) con la cassa esterna dell'iniettore (messa a terra) in modo da smorzare la corrente d'arco che interessa tale griglia e si richiude sul conduttore di ritorno della linea di trasmissione. Vengono descritti il progetto e la costruzione di un prototipo installato presso il laboratorio francese del CEA (*Commissariat à l'Énergie Atomique*) di Cadarache, dove dovrà essere testato. L'impianto di prova di tale laboratorio viene poi modellato nel dettaglio per poter confrontare i risultati sperimentali e poterli interpretare. Il secondo dispositivo è uno snubber magnetico distribuito lungo tutto lo sviluppo della linea di trasmissione, in modo da smorzare al meglio ogni possibile guasto con un minor ingombro sul sistema e una struttura più semplice ed efficace. I risultati di una prova sperimentale su un modello in scala ridotta sono presentati a supporto della proposta.

Il *capitolo 4* delinea un esempio di progetto integrato di protezioni passive su un intero sistema. In particolare, per l'esperimento della sorgente di ioni negativi, vengono proposti, studiati e ottimizzati su un opportuno circuito equivalente gli effetti positivi del resistore di smorzamento, dello snubber magnetico distribuito e di un'impedenza L–R parallelo interposta tra alimentatore e linea di trasmissione. Infine viene descritto il progetto dello snubber, costituito da una serie di nuclei magnetici equispaziati lungo la linea e polarizzati da un opportuno circuito.

Abstract

The necessity of new and clean technologies for energy production from one hand and the carbon dioxide emission regulations on the other are inducing nuclear fusion research to speed towards a possible future energy source.

So the next experiment, which is being built in France, called ITER (acronym for *International Thermonuclear Experimental Reactor*, an international collaboration between European Union, Japan, Russian Federation, India, China, South Korea and United States of America) has to give an answer on the real feasibility to achieve nuclear fusion, and in particular on the possibility to control the plasma stability for long time at high temperature, to maintain the stationary phase and to reach fusion temperature.

One of the components necessary to heat the plasma is the Neutral Beam Injector; the concept has been developed for many years up to the present experiments. The principle is basic: the plasma is hit by a neutral atoms beam (not affected by the high magnetic field of the system) at high kinetic energy so that this energy is transferred by collisions to the ions of the plasma. Meanwhile the beam helps to drive the plasma current, necessary for the plasma confinement inside the vessel in a "tokamak" configuration.

The engineering requirements for the ITER NBI are very demanding, as it is subjected by severe mechanical, thermic and electrical stress. In particular, the neutral beam power requested is 16.5 MW while the energy of the deuterium or hydrogen negative ions, accelerated before neutralization, is in the order of 1 MeV. This involves a total accelerating voltage equal to 1 MV.

So one of the most critical topic for the whole system is the operation very close to the breakdown limits for the accelerating grids, so that breakdown is not considered as a fault but a common working condition for the system.

The activity reported in this doctoral thesis, mainly carried out at Consorzio RFX, deals on this matter. In particular the effects of arc between the grids are analyzed, both in terms of arc energy deposition on the grids and in terms of the current and voltage transient propagation on different locations of the system. Arc energy has to be limited below a certain threshold value in order to avoid an irreversible grids damage; this would cause the de-conditioning and the loss of high voltage holding with a breakdown occurrence at lower voltage level. Instead the fast voltage transients are dangerous because they can induce overvoltages on some tricky points and therefore lead to unexpected insulation losses; in addition they are source of electromagnetic noise (EMI) due to high frequencies in the order of MHz, a problem if we consider the large number of diagnostic devices.

In this thesis some design solutions to limit these effects are explained; they are sup-

ported by proper circuital simulations or experimental validation. The devices presented are alternative to the present adopted solutions, as they form a comprehensive protection strategy. Then, they are passive protections because we need an instantaneous intervention after breakdown to be effective, contrary to active protections which need some delay due to the signal acquisition demonstrating the arc occurrence. The thesis is organized as follows.

In the *chapter 1* the ITER neutral beam injector is presented, in the framework of the nuclear fusion research; the operation principles and the main components are basically described. Finally the test facility being built in Padua is shown; it is constituted by two experiments, a ITER full-scale negative ion sources, with a single -100 kV accelerating stage, and a full-scale injector, identical to that which will be installed in ITER.

The *chapter 2* shows at first the operating conditions, from the electrical point of view, foreseen for the neutral beam injector. In particular high voltage holding issues are presented, together with the conditioning process in vacuum; then a tentative vacuum arc modeling for long gap is described, considering arc energy dissipation due mainly to radiation phenomenon. At last present countermeasures against breakdown effects are shown, namely a concentrated core snubber at the injector transmission line ends and the active protections.

In the *chapter 3* two new concepts for passive protections are introduced. The first is a damping resistor connecting the last accelerating grid (the so called grounded grid) with the vacuum vessel (grounded) of the injector with the aim to damp the arc current involving this grid and the return conductor of the transmission line. Then the design and the assembly of a prototype are described; this is installed at the French laboratory of CEA (*Commissariat à l'Énergie Atomique*) in Cadarache, where it will be tested. The detailed circuital modeling of this test bed is reported; the model is useful to compare and understand experimental results. The second device is a distributed core snubber along the whole transmission line to damp the breakdown with a less cumbersome element and a simpler, more effective structure. The results on a small-scale example are presented to support this proposal.

The *chapter 4* outlines an integration of a comprehensive design for passive protections on a whole system. In particular, for the experimental negative ion source the positive effects of some devices are proposed, studied and optimized, i.e. a damper resistor, a distributed core snubber and a L–R parallel input impedance between the power supply and the transmission line. Finally the core snubber design is described, constituted by a series of magnetic cores evenly distributed on the transmission line and polarized by a proper biasing circuit.

1

Neutral beam injection background

1.1 The Energy problem

The energetic system is the base of the modern society in all its main aspects: social, cultural, economic and technological. It is well known that humankind is going through a critical and unstable period regarding the energy resources. What's more, this matter belongs to a wider range of problems like climate, food, minerals and so on. So the solution for the energy problem has to intercept the solutions of the other problems, in order to guarantee the sustainable development of our society. Today, most of the worldwide electricity demand is satisfied by oil (41 %), natural gas (22 %), coal (16 %), nuclear (15 %) and renewables (6 %). Between these technologies only renewables and nuclear fission can limit the CO_2 emissions. The renewables, even if they will contribute much more in the future, won't be able to satisfy the total demand. About nuclear fission, it is a long term energy source (at least when produced by means of the breeder reactors) with known impacts to the economics and environmental cycles. There are however some unsolved problems, related mainly on the waste treatment and storage, on power plant intrinsic security and on future uranium supplying which still limit the spread of nuclear plants. At the end it will depend on the public appreciation of options and alternatives.

So nowadays, more than in every other moment of our history, secure and sustainable energy sources are required for the development of humankind. As a consequence, researchers from all over the world are working to develop a range of environmentally acceptable, safe and sustainable energy technologies. It is also crucial try to diversify the energetic sources for the production of energy – in particular electric – giving priority to the more available fuels, to the more advanced technologies and to the sources free from altering-climate emission. Nuclear fusion is one of these possibilities.

The primary fuels for nuclear fusion are deuterium (an isotope of hydrogen) and lithium. Deuterium can be extracted from sea water while lithium is abundant in the Earth upper crust. In a power plant lithium is used to breed the tritium (another hydrogen isotope), which fuses together with deuterium producing helium, a noble gas. Only 150 kg deuterium and 2–3 tonnes of lithium are needed for a full year electricity supplying one million people. Fusion power plants will be particularly suited for base load energy generation, to serve the needs of densely populated areas and industrial zones. They can also produce hydrogen for a "hydrogen economy", in order to substitute polluting fuels for transport, as a clean energy carrier.

1.2 Thermonuclear magnetic controlled fusion

Nuclear fusion is the process that powers the sun and other stars – providing heat and light to sustain life on Earth. Basically, fusion is the nuclear reaction among two light nuclei that fuse into a heavier one, releasing a net energy gain and other reaction products such as neutrons. For many decades researchers have studied the possibility to achieve controlled fusion reactions on Earth, in order to produce energy for peaceful purposes. Two light nuclei can fuse together if they are brought sufficiently close for the short-range attractive nuclear force to overcome the Coulomb repulsion among them: this is possible if the two nuclei collide with high enough kinetic energy. For a significant fraction of fusion reactions to occur matter has to be brought to sufficiently high density and temperature (in the order of 100 million degrees), for a sufficiently long time. In such conditions matter is in the plasma state, a quasi-neutral ensemble of ions and electrons. While gravity confines the hot plasma in the stars, on Earth instead strong magnetic fields can be used to hold the plasma inside a chamber (the so called magnetic confinement approach). It is well known that a charged particle in a magnetic field makes a spiraling motion around the magnetic field lines. In absence of collisions and using closed magnetic geometry it is thus possible to confine plasmas for relatively long times.

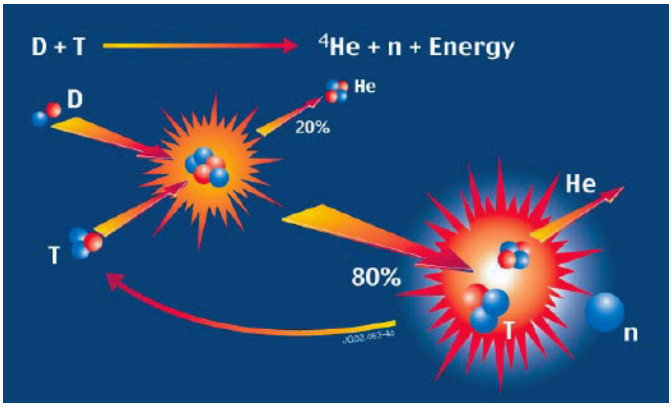

Figure 1.1: The nuclear fusion reaction [1]

The most promising reaction involves light nuclei as deuterium (^2_1D), tritium (^3_1T) and

helium ${}^3_2He$ (see fig. 1.1), because it has the highest reaction rates at lower temperature ($\lesssim$ 20 keV, see fig. 1.2). This is:

$$ {}^2_1D + {}^3_1T \rightarrow {}^4_2He + {}^1_0n + 17.6 \text{ MeV} \tag{1.1} $$

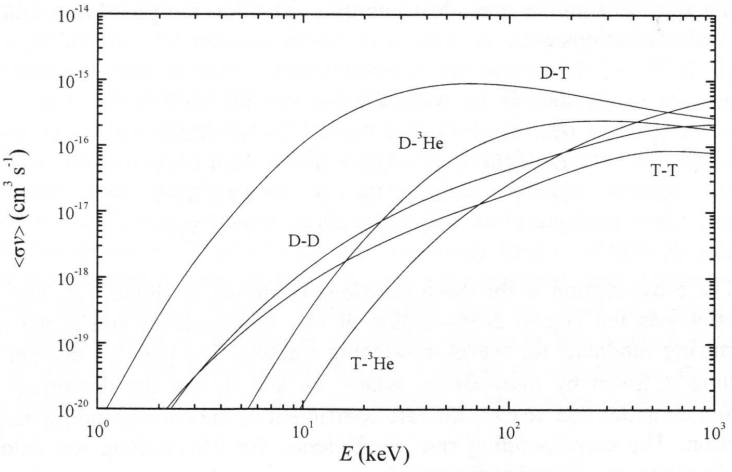

Figure 1.2: Fusion reaction rate $\langle \sigma v \rangle$ for couples of reactants

Deuterium resources on Earth are practically endless, 0.0015 of hydrogen atoms in water being deuterium, even though extraction methods are not yet affordable. Tritium is also an isotope of hydrogen but it occurs naturally in only negligible amounts, due to its radioactive half-life of only 12.3 years. Tritium can be obtained from the two following reactions with lithium:

$$ {}^6_3Li + {}^1_0n \rightarrow {}^3_1T + {}^4_2He + 4.8 \text{ MeV} \tag{1.2} $$

$$ {}^7_3Li + {}^1_0n \rightarrow {}^3_1T + {}^4_2He + {}^1_0n - 2.5 \text{ MeV} \tag{1.3} $$

The adoption of a lithium blanket on the vacuum vessel of fusion reactors should be adequate to provide the necessary tritium source for an unlimited period of time, based on the present lithium resources. Compared to fossil fuel power plant, there is no production of greenhouses gases, since the main natural product of the fusion reaction is helium, which is completely harmless to life and doesn't contribute to global warming. In addition, in a fusion reactor, unlike fission ones, there is no risk of uncontrolled runaway of the reaction. The tentative scheme for a fusion reactor plant is shown in fig. 1.3.

1.2.1 The burning criteria

For the balance of a fusion reactor to be positive, the energy produced by fusion reactions has to exceed that required to create and sustain the plasma itself. One form of energy loss for a $D-T$ plasma, with electron density $n_e (n_D = n_T = n_e/2)$ and temperature

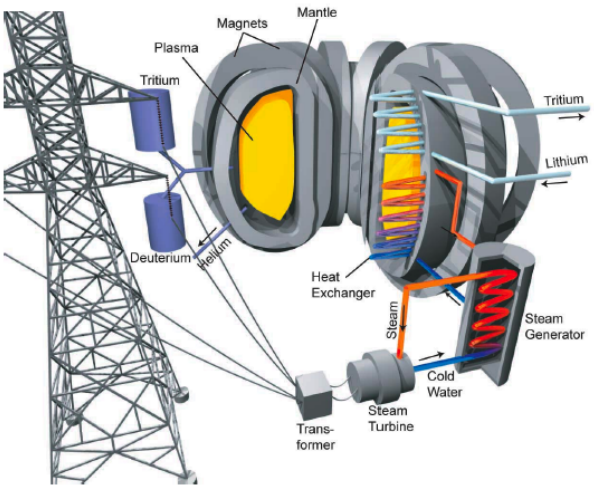

Figure 1.3: Schematic of a future fusion reactor

T_i is bremsstrahlung radiation. The power lost per unit volume due to bremsstrahlung emission is $P_b = bn^2T^{1/2}$, where b is a function of the effective charge $Z_{eff} = n_i^{-1}\sum_i n_i Z^2$ in a multi-species plasma. In addition, power losses due to confinement degradation, e.g. through collisional and turbulent transport phenomena, have to be considered in the power balance. A simple estimate of the energy losses due to mechanism different from bremsstrahlung can be made as $P_t = 3nT/\tau_E$, by introducing the average energy confinement time τ_E. The power generated by fusion reactions can be written as $P_n = W_{DT}n^2\frac{\langle\sigma v\rangle_{T_i}}{4}$, where $W_{DT} = 17.6$ MeV is the energy released after a single $D-T$ reaction and $\langle\sigma v\rangle_{T_i}$ is the $D-T$ fusion reaction rate, which is the function of the temperature T_i. Assuming that the reaction power P_n can be converted in electric power with an efficiency η, then re-injected in the reactor in order to balance the energy losses, the self-sustainment condition is:

$$P_b + P_t \leq \eta(P_b + P_t - P_n) \tag{1.4}$$

which can be rewritten as:

$$n\tau_E \geq 3T\left(\frac{\eta}{1-\eta}\frac{W_{DT}}{4}\langle\sigma v\rangle_{T_i} - b\sqrt{T_i}\right)^{-1} \tag{1.5}$$

This last expression is also known as Lawson's criterion. The right end side of equation 1.5 depends only on temperature, hence the product $n\tau_E$ where the equality is satisfied can be plotted as a function of T_i. The curve with efficiency $\eta = 30\%$ has a minimum at $T_i \simeq 20$ keV.

The most probable reactor scenario is one in which the α particles (^4_2He nuclei) produced by fusion reactions are confined by the magnetic field and replace all the energy losses by transferring their energy to the plasma, whereas neutrons escape the plasma

volume and their energy is converted to electric energy. In this case, the Lawson's criterion must be modified; it is called ignition criterion and is written as $P_b + P_t \leq P_\alpha$ which can be expressed as:

$$n\tau_E \geq 3T\left(\frac{W_\alpha}{4}\langle\sigma v\rangle_{T_i} - b\sqrt{T_i}\right)^{-1} \tag{1.6}$$

where $W_\alpha = W_{DT}/5$ is the energy of a single α particle after a fusion reaction. The $n\tau_E$ curve that corresponds to the equality is shown in fig. 1.4. As the Lawson's criterion curve, the ignition curve has a minimum at $T_i \simeq 20$ keV. Isolating the temperature dependence in the right term of equation 1.6 we obtain the classical form of the so called *triple product*:

$$n\tau_E T_i \geq 3 \cdot 10^{21}\ \mathrm{m}^{-3}\ \mathrm{s\ keV} \tag{1.7}$$

For temperatures $T_i \simeq 20$ keV and electron densities $n_e \simeq 10^{20}$ m^{-3}, which are expected in a fusion reactor, the energy confinement time τ_E must be greater than 1 s. Fig. 1.4 shows the values of the triple product reached in fusion devices since the beginning of experiments in plasma physics. The trend shows the improvement in confinement achieved up to now and the goal that the scientific community must reach to provide a fusion power plant.

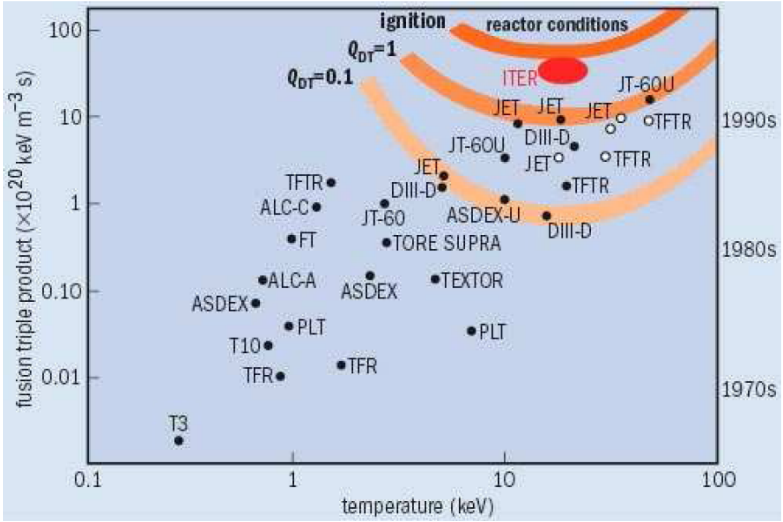

Figure 1.4: Values of the fusion triple product as a function of ion temperature for existing experiments and ITER

1.3 ITER project

The large experimental database obtained in the last thirty years on magnetic confinement experiments, and the improving capability of numerical simulations, have provided

to the international community the physics basis for the design of a burning plasma experiment based on the "tokamak" concept, which is called ITER. The name is the acronym for *International Thermonuclear Experimental Reactor*, but it means also *the way* in latin, because it is also considered the experimental way towards controlled fusion as a peaceful power energy source. The tokamak has been the most successful concept to confine fusion plasmas up to now. Alternative concepts, like Reversed Field Pinch and Stellarator, are also developed to prepare for fusion power plants.

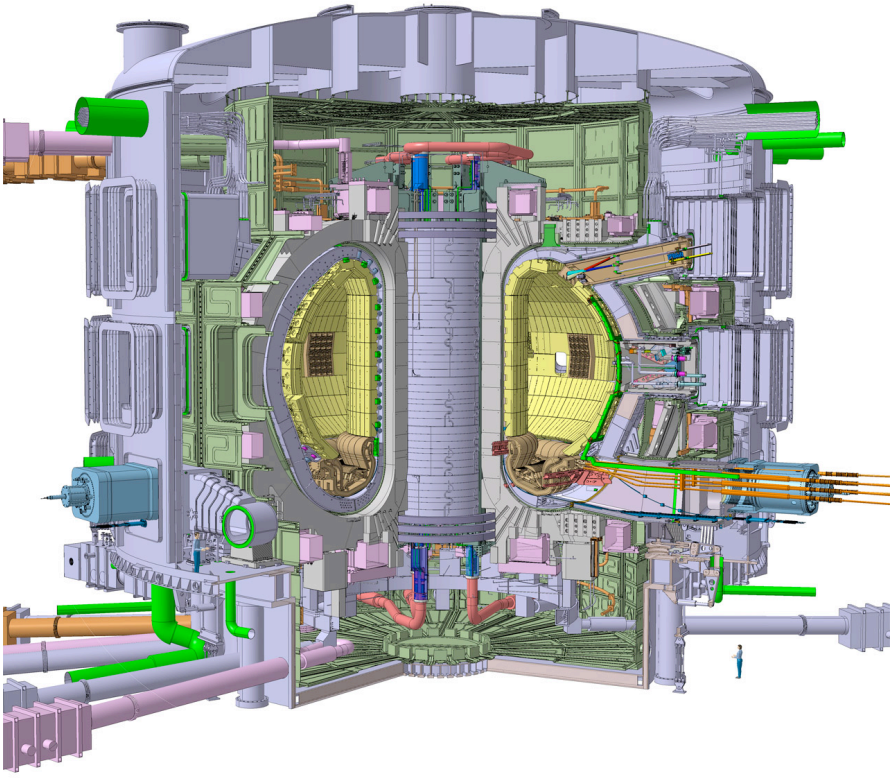

Figure 1.5: Schematic overview of the *International Thermonuclear Experimental Reactor* [2]

ITER (see fig. 1.5) is an international tokamak research project, which is intended to be an experimental setup between present studies of plasma physics and future electricity-producing fusion power plants. It will be built upon research conducted with devices such as ASDEX Upgrade (D), DIII-D and TFTR(US), EAST (RC), JET (EU), T-15 (RUS), and will be considerably larger than any of them.

On November 21, 2006, the seven participants (European Union, Japan, Russian Federation, People's Republic of China, South Korea, India and United States of America) formally agreed to fund the project. The program is anticipated to last for 30 years – 10 years for construction and 20 years of operation – and the cost approximately

10 billions € makes it one of the most expensive modern techno-scientific projects. It will be based in Cadarache, France. It is technically ready to start construction and the first plasma operation is expected in 2018.

The principal aims for ITER are:

- to achieve extended burn in inductively-driven plasmas with $Q = \frac{Q_{fus}}{Q_{aux}} \geq 10$, at a nominal fusion power output of about 500 MW for a range of operating scenarios and with a duration sufficient ($\sim$ 400 s) to achieve stationary conditions;
- the fusion of 0.5 g of deuterium/tritium mixture in its approximately 840 m^3 reactor chamber;
- to aim at demonstrating steady state operation using non-inductive current drive with a ratio of fusion power to input power for current drive of at least 5;
- the possibility of high Q operation exploitation, if favorable confinement conditions can be achieved.

The main parameters of ITER are the following:

- $P_{out} = 500$ MW nominal;
- major radius $R_0 = 6.2$ m;
- minor radius $a = 2$ m;
- maximum toroidal field $B_{max} = 5.3$ T;
- plasma current $I_p = 15$ MA.

ITER is predicted to produce inductively driven $D - T$ plasmas. These plasmas will be with density $n_e \approx 10^{20}$ m^{-3} and core electron and ion tempeartures of $T_e \approx 8.8$ keV and $T_i \approx 8$ keV. New physical regimes will be explored with ITER. For example, conditions in which the α particles contribute significantly to the plasma pressure, with a class of plasma instabilities which can be studied in depth only with this new device. Again, a variety of technological issues could also be studied in ITER, like the test of advanced materials facing very large heat and particle fluxes, the test of concepts for a tritium breeding module, the superconducting technology under high neutron flux and many others. The auxiliary systems needed to achieve the conditions expected in ITER are an external heating and current drive capability of 73 MW and several advanced diagnostics for both analysis and plasma control. All of these requirements are expected to solve many of the scientific and engineering issues concerning a burning plasma and could allow to make a straightforward step towards the demonstration of a tokamak power plant.

1.3.1 Heating and Current Drive

The heating and current drive (H&CD) systems for ITER are an appropriate combination of neutral beam injectors (NBI) and radio-frequency (RF) antennas, operating at the electron cyclotron (EC), ion cyclotron (IC) and intermediate lower hybrid (LH) frequency (fig. 1.7). The concept is shown in fig. 1.6.

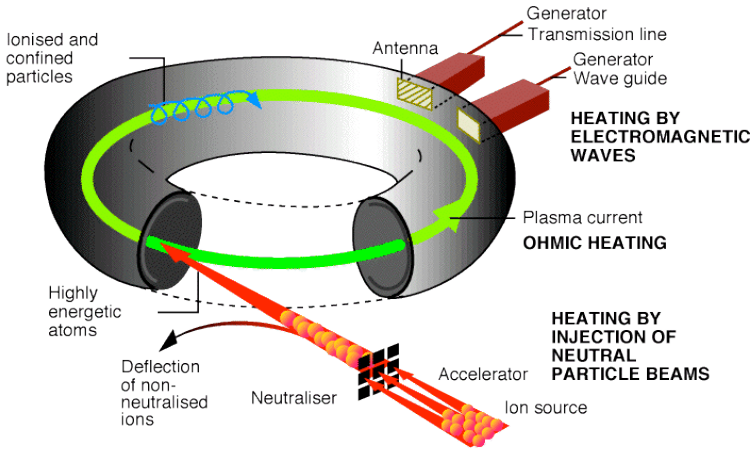

Figure 1.6: Heating and Current Drive systems

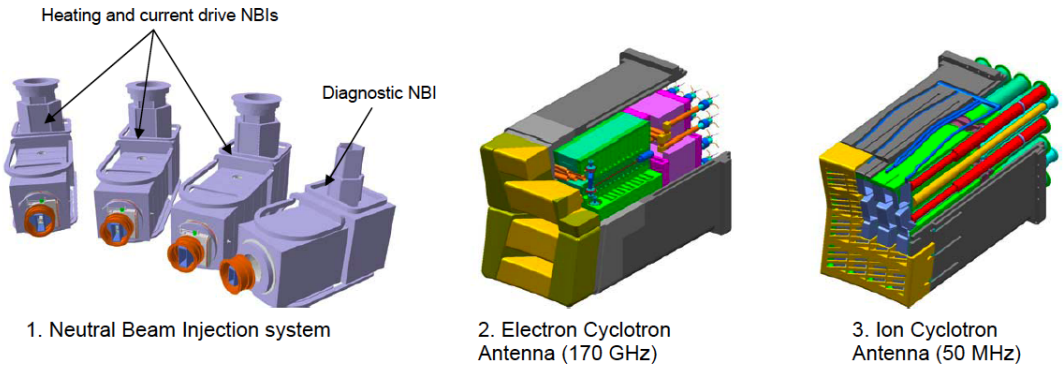

Figure 1.7: Overview of the ITER Heating and Current Drive systems

They aim at providing an active control on all the key phases of the operating scenarios:

- the plasma temperature rise, while density is increased to allow the requisite fusion power;
- the achievement of a steady burn;
- the control of the excursions about the operating point;

- the suppression of instabilities;
- the achievement of a soft termination.

The neutral beam system design consists, at present, of two heating and current drive injectors and one diagnostic neutral beam injector. Each heating neutral beam injector will deliver a deuterium beam of 16.5 MW (total 33 MW), with an energy of 1 MeV, and will be able to operate for long pulses (up to 3600 s for steady state operation).

1.4 Neutral beam heating

Neutral beam heating is considered up to now the most important method for plasma heating in many fusion experiments around the world. The concept is straightforward: neutral atoms can penetrate through the confining magnetic field and are ionized in the plasma via collisions with electrons and ions. The fast ions generated in this way are then confined by magnetic field as well. If their kinetic energy is large compared to the plasma temperature they deliver their energy to plasma ions and electrons by collisions, thereby heating up the plasma. Fast neutral atom beams are generated via charge exchange neutralization of ion beams.

1.4.1 Principle

High power neutral beams for heating high temperature plasma are required for the realization of controlled thermonuclear fusion as energy source. The ion sources used for such neutral beam injection (NBI) systems are characterized by high energy (several hundred keV) and high current (several tens of A) and consequently by high power (several tens of MW).

In agreement with most of the literature on this topic, here the term ion source (IS) indicates the assembly of:

1. a plasma source, where the plasma is generated;
2. an extractor, where the ions in the plasma are extracted by means of an electric potential, forming an ion beam;
3. an accelerator, where the ion beam is accelerated to the maximum potential.

The injected beam energy is determined by the expected penetration depth in the target plasma. Beam energy has increased from about 20 keV, for the first experiments on injection into magnetically confined plasmas in 1974, up to about 400 keV at present, as the target plasma size has become larger. In a future fusion reactor the beam energy will need to be up to 2 MeV. The neutral beam is obtained by charge-exchange conversion from an ion beam and at higher energies, above 100 keV per nucleon, the neutralization efficiency for positive ions decreases drastically while it maintains around 60 % efficiency for negative ions. Thus, large scale positive ion sources were developed in the 70s and 80s when the required beam energy was below 80 keV per nucleon, followed by negative

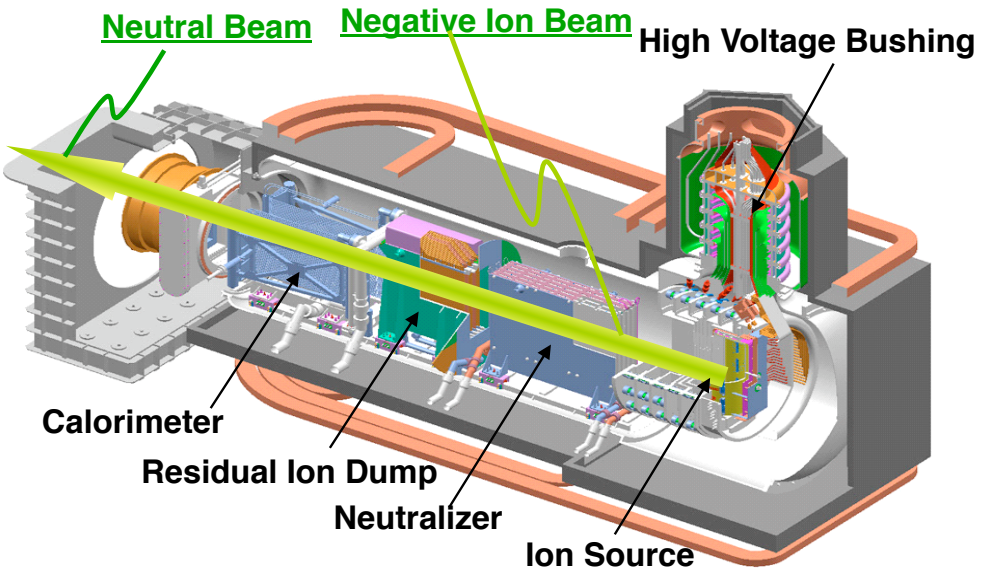

Figure 1.8: Schematic of the ITER Neutral Beam Injector

ion source development for high energy NBI systems aimed at reactor fusion machines. In fig. 1.8 the scheme of the ITER NBI is shown.

1.4.2 Negative Ion Source

The 2001 design of the ion source was based on the arc source concept where tungsten electrodes, placed inside the source, are heated in order to emit electrons. These were accelerated by 100 V so ionizing the filling gas. Recently the design of the plasma source is changed towards a radio-frequency type (fig. 1.9). This is composed by a RF coil, an expansion region, a filament starter and a cesium oven. Usually a RF driver works at a frequency of 1 MHz with electric power up to 200 kW. This choice implies more simplicity, maintaining of the source and a more suitable ions beam modulation, a very important property for the working of the NBI.

The negative ion source has to produce a negative ions flux at the plasma grid, the first grid of the extraction system. The driver has a tungsten starter filament, heated by a current, to initiate the plasma into the source: a first plasma with an energy of about 10 eV is here created. When a sufficient ion density is reached the RF can sustain the plasma transferring energy by inductive effect.

The negative ions are produced either by particle reactions into the plasma or by the surface conversion of charged and neutral particles, hitting the chamber wall covered by cesium. The cesium is vaporized inside the chamber itself, diffusing from the cesium oven and condensing on the colder wall. The cesium is used because it acts as a catalyst of trapped electrons by ions reaction: it lowers the work function of the metal surface, that easily emits an electron when an ion or a neutral atom hits it. The low electron affinity

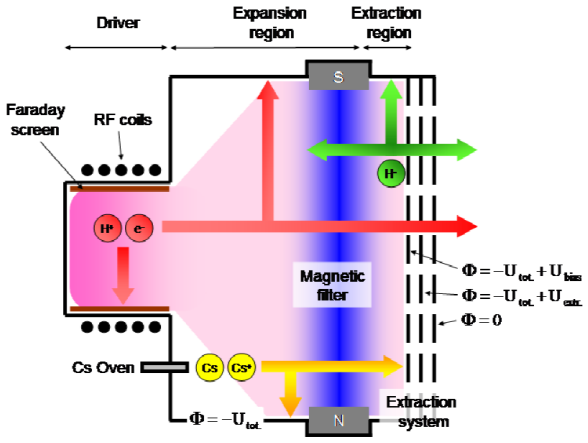

Figure 1.9: RF Ion source principle

is a positive behaviour from one hand because it helps ions to neutralize; from the other hand it is a drawback for the negative ion production because collisions with plasma can easily strip their electrons. So the best place devoted to negative ions production is the plasma grid, i.e. the closest region to the extraction.

The source can work with two different operating gas: hydrogen (H^-) and deuterium (D^-). The same beam source is used for both the HNB (Heating Neutral Beam) and DNB (Diagnostic Neutral Beam) injectors. The main parameters of the beam source are described in the table 1.1.

Table 1.1: Specification of the beam source for the HNB and the DNB

	HNB		DNB
Ion species	D^-	H^-	H^-
Power	< 1 MW	< 1 MW	< 1 MW
Beam current	40 A	60 A	60 A
Pulse length	3600 s	3600 s	3600 s, modulated as necessary
Source filling pressure	0.3 Pa	0.3 Pa	0.3 Pa
Extracted electron to accelerated ratio	< 1	< 0.5	< 0.5

In a different behaviour from positive ion sources, a great limit for negative ones is the easy extraction of electrons in consequence of ion collisions. We need to remove the co-extracted electrons: the solution is the utilization of magnetic filters. In particular, embedded magnets in the accelerating grids allow to suppress electrons downstream the source. These are placed inside the wall of ion source, creating a multi-cusp magnetic configuration.

The main challenge of the ion source for ITER is the plasma uniformity in space, to be maintained within 10 % in a wide area – about one hundred cm^2 – and generating a

total current of tens of Amperes. To achieve this target 8 RF driver for plasma generation are used.

1.4.3 Extraction

The extractor is constituted by two grids, called plasma and extraction grids. The second is at a potential of 12 kV, referred to the source. Grids are drilled with cylindrical or conical profile holes which extract beamlets from the ion source. The gap between the grids and the hole aperture are important parameters to allow a proper focus to the extracted beam. Each grid of the ITER NBI is divided in 4 segments, each with 320 apertures for a surface of 2000 cm^2. Each segment contains 4 groups of apertures, arranged in a regular 5 x 16 rectangular array. To reduce the unavoidable co-extracted electron current a polarization of the plasma grid respect to the plasma potential is applied. Electrons are also created in the space between the two grids by stripping, i.e. the loss of an electron by collision of a negative ion with the gas molecules in the extractor. Suppression of electrons leaked from the extractor to the accelerator is extremely important, as acceleration of electrons to high energy would drastically reduce the efficiency of the acceleration system; so the magnetic field, generated around the plasma grid, deflects the electrons onto the extraction grid. It minimizes then the number of electrons and prevent them to be accelerated to higher energies.

1.4.4 Acceleration

At the moment the NBI reference acceleration stage is designed as a Multi Aperture Multi Gap (MAMuG) system. In the past, another concept was proposed by the European team, called Single Aperture Single Gap (SINGAP). See fig. 1.10 for a schematic view of the two grids system. In the MAMuG concept 5 grids are used to energize the negative extracted beam up to 1 MV in steps of 200 kV; instead on the SINGAP there are a pre-acceleration grid at 60 kV and then a single stage to accelerate the ions beam up to 1 MV. Even if this configuration is simpler than the former it is strongly worst considering the very high rate of electron stripping and fully accelerated up to 1 MV. With the MAMuG configuration this is avoided, thanks to the intermediate stage grids: each grid has a magnet embedded to steer the stripped electrons from the main beam. Present design of MAMuG and SINGAP accelerators use very different mechanical concepts for the supports, the connections to the high voltage bushing and the bushing itself.

1.4.5 Neutralization

At the energy required for the NBI, as already reported, the efficiency of ion neutralization is greater for negative charged ions than the positive ones, see fig. 1.11. The neutralization of the accelerated negative ion beam is achieved by exchange charge collisions between the beam and D_2 in a structure called neutralizer.

The pressure in this component has to be high enough to provide a high neutralization efficiency but no so high because the gas can diffuse and affect the beam stripping losses

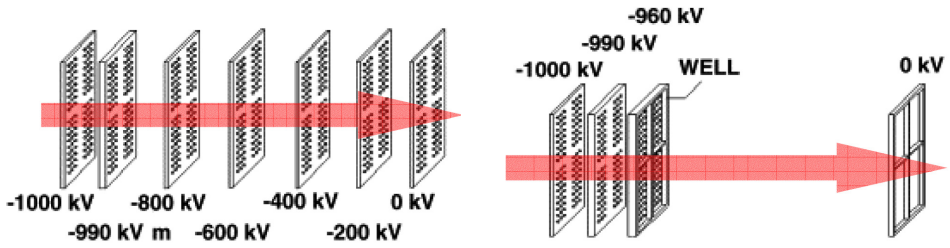

(a) (b)

Figure 1.10: Overview of the two concepts for the ITER Neutral Beam Injector: (a) MAMuG; (b) SINGAP

in the acceleration stages. This device is composed of 4 vertical channel, between which the beam flows and in which the gas is injected approximately midway along the beam path. The neutral gas is pumped by cryopumps in order to control the pressure for a proper neutralization.

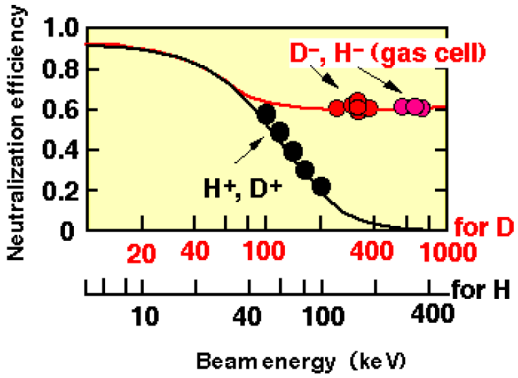

Figure 1.11: Neutralization efficiency for positive and negative deuterium and hydrogen ions against beam energy per nucleon

1.4.6 Residual Ion Dumping and Deflection system

The efficiency of the neutralizer is about 20 %, so the fraction of charged particles downstream the neutralizer has to be removed from the beam. This is worked out by a component called Residual Ion Dump (RID). In the present design an electrical field is applied between the panels of RID; a new concept is now studied, to achieve the steering effect by magnetic field. The D^0 beam is unaffected by the electric field in the RID so it proceeds to the plasma through a duct, connecting the injector and the tokamak.

1.4.7 Power supply

The NBI power supply system has to provide the electrical power for the accelerating grids, the ion source and the auxiliary systems [3]. The part devoted to the accelerating grids is called accelerating grid power supply (AGPS). It is referred to ground and it is placed in a power supply building. The ion source power supplies instead are housed in an air insulated Faraday cage called high voltage deck 1 (HVD1), referred to -1 MV to ground. Electric power to the NBI is supplied by a multi-conductors transmission line (TL). The NBI TL is a multipolar transmission line (for the MAMuG configuration) composed by 2 coaxial conductors, with the inner one at -1 MV respect to the grounded external one, and some conductors placed in the interspace with potential of -800, -600, -400 and -200 kV. These potentials are supplied by the AGPS with the aim to feed the electrostatic acceleration stages of the NBI. The volume inside the TL is filled by an insulating gas, sulphur hexafluoride (SF_6) pressurized at 6 bar [4], able to withstand the very high electric field strength, due to the 1 MV voltage between the inner and the outer TL conductors [5]. A scheme of the connection between power supplies and the injector, with the utilization of different insulating materials, is shown in fig. 1.12.

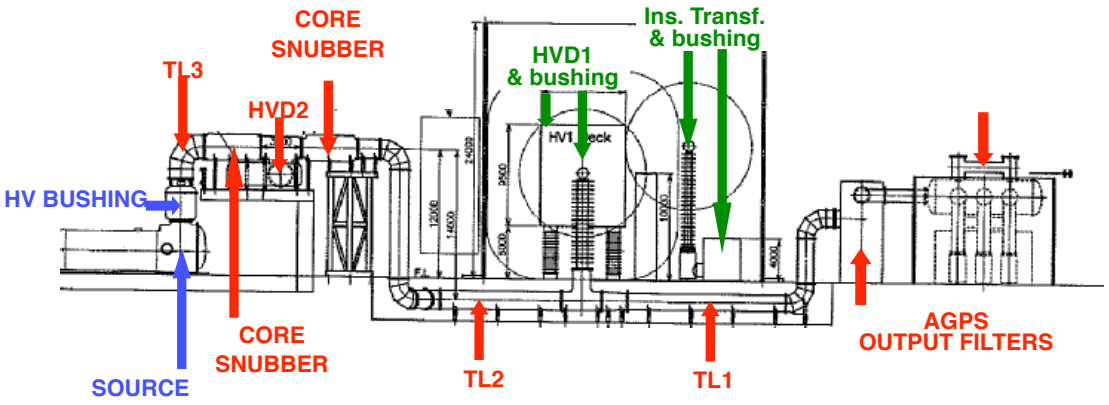

Figure 1.12: Scheme of the power supply connection to the injector; colors are associated to different insulation material: green for oil–air, red for SF_6 and blue for vacuum

Auxiliary systems (cooling water and gas) are supplied to the ion source through an access near the source and known as high voltage deck 2 (HVD2). The TL is composed by 3 sections, named TL1, TL2 and TL3. The first section TL1 connects the AGPS with the HVD1, the second section TL2 connects HVD1 with HVD2 and the third section TL3 connects HVD2 with the IS through a bushing. This bushing separates the SF_6 area inside the TL from the vacuum area inside the injectors. The TL3 runs inside the tokamak building so it is subjected to high energetic neutron, X and γ radiations. All the connections to supply the IS for electric power, gas and cooling water are hosted inside the -1 MV conductor of TL2 and TL3. The three sections of the TL have different

dimensions. A large part of the TL is placed underground, except the initial part of TL1 and, in particular, the final part of TL2.

In the fig. 1.13 the scheme of the power supply design for the MAMuG configuration is shown: AGPS is composed by an input step-down transformer and a thyristor power converter system, followed by five 200 kV dc stages, see table 1.2. Each stage is composed by a step up transformer, a diode voltage rectifier and an output dc filter. The ion source and extraction power supply (ISEPS) is composed by 4 independent RF generators, the extraction grid power supply, the bias and plasma grid filter.

Table 1.2: AGPS rated voltages and currents in the MAMuG configuration stages

parameters	D^- 1 MV 40 A		H^- 870 kV 46 A	
	voltage [kV]	current [A]	voltage [kV]	current [A]
G1	200	59.4	174	62.8
G2	200	56.4	174	60,4
G3	200	51.1	174	56.1
G4	200	48.0	174	53.0
G5	200	45.3	174	50.9
Total AGPS power	52.1 MW		43.9 MW	

1.5 The Padova Neutral Beam test facility

In the framework of the activity planned by the ITER Organization for the research and development of the NBI (construction, operation, solutions for its problems) Padova was chosen to host a test facility, called PRIMA (acronym for *Padova Research on ITER Megavolt Accelerator*); it includes two experiments: a full size plasma source with low voltage extraction and a full size NBI at full beam power (voltage up to 1 MV). The first experiment is called SPIDER (acronym for *Source for Productions of Ions of Deuterium Extracted from Radio-frequency*) while the second is called MITICA (*Megavolt ITER Injector and Concept Advancement*). The layout of this test facility including both experiments is shown in fig. 1.14.

SPIDER

This full-size ITER-like plasma source has to show the performance of such negative ions source, compared to the ITER specification. In particular it has to give information about [6]:

- the current density;
- the current density uniformity;
- the limitation of the electron/ion ratio;

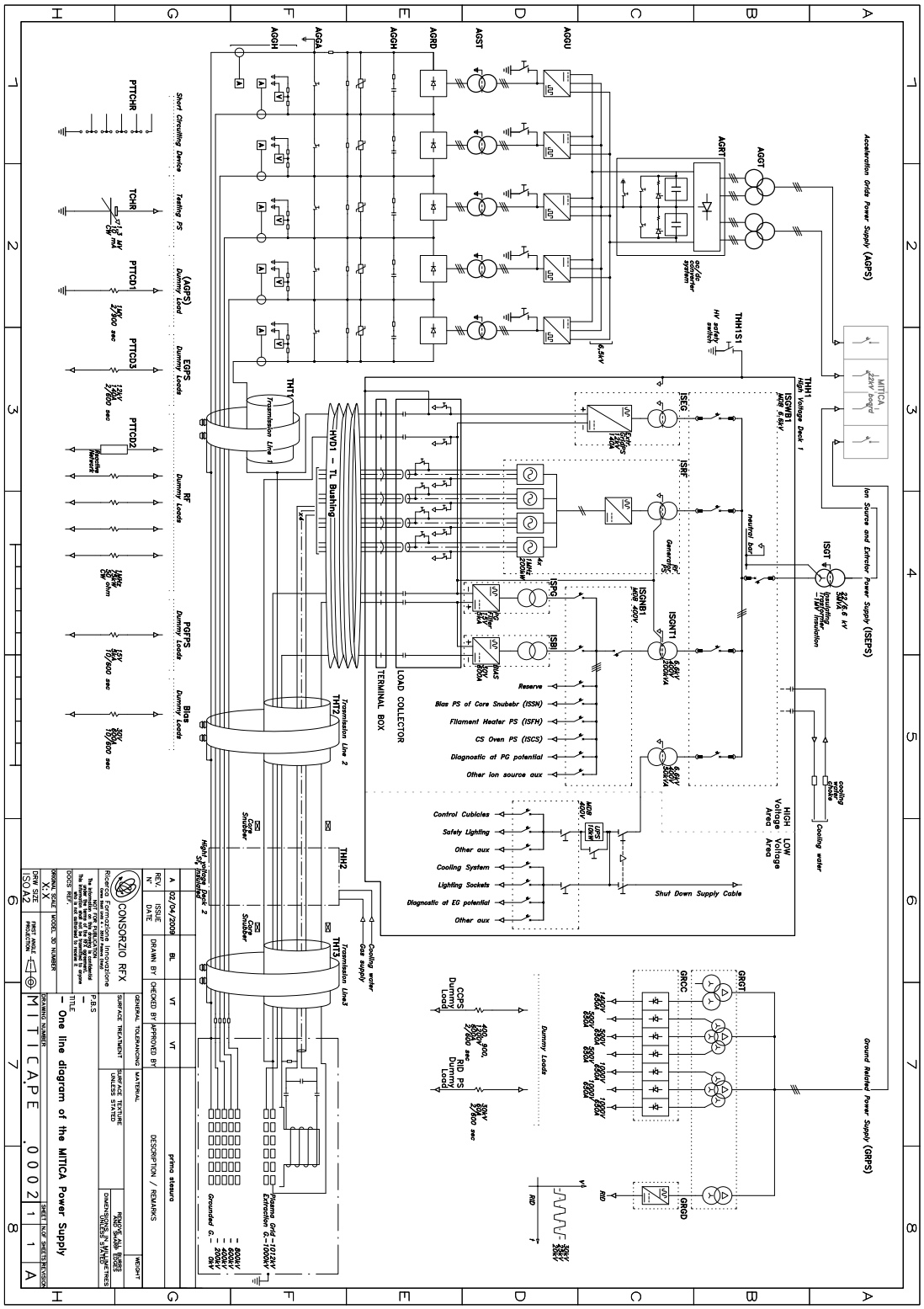

Figure 1.13: Reference scheme for the NBI power supply

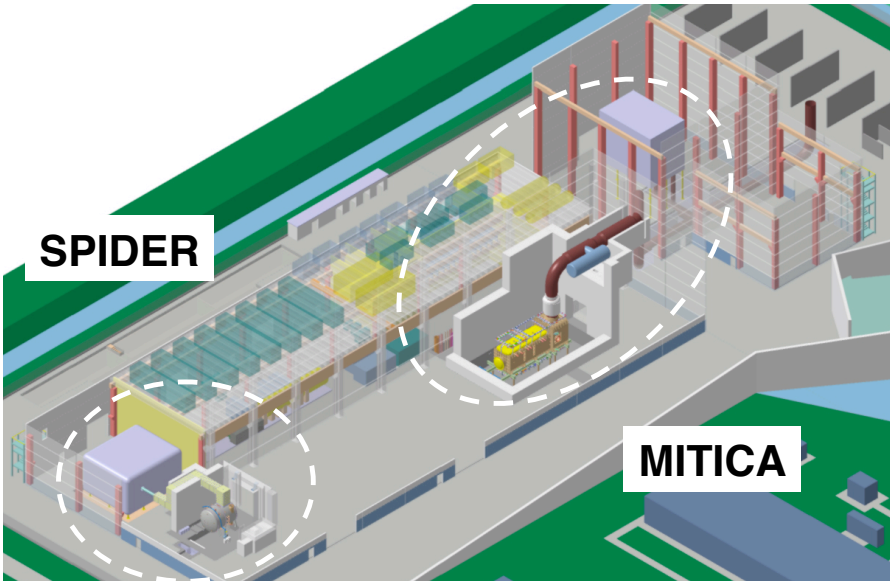

Figure 1.14: PRIMA buildings and layout of plants

- the low source pressure;
- the stationary operation at full current with constant performances up to 1 hour.

The required negative ion current density to be extracted from the plasma source ranges from 290 A/m^2 in D^- and 350 A/m^2 in H^- and these values should be obtained at the lowest admissible neutral pressure in the plasma source volume, which nominal value is 0.3 Pa. The electron to ion ratio should be limited to less than 1 and the admissible ion inhomogeneity, extracted from the grids, should be better than 10 % on the whole plasma cross-section, having a surface exposed to the extraction grid in the order of 1.5 m^2. Another requirement is the production and extraction of a negative ion plasma for one hour, assuring the beam modulation required by ITER full power and diagnostic beam operation. Finally, the capability of optimization of the cesium consumption and the tolerance to the presence of impurities have to be studied. The plasma source is based on the RF concept, including eight RF drivers, operating at 1 MHz. A section of the design is shown in fig. 1.15, while the layout is reported in fig. 1.16.

1.5.1 Power supply

From the electrical point of view the vessel of the experiment is maintained at ground potential while the source is at a voltage of -100 kV. The source requires then a number of power supplies polarized at -100 kV potential hosted in a insulated platform called high voltage deck forming the ion source and extraction power supply system (ISEPS). Since the source is a prototype for the ITER 1 MV injector the source power supplies are identical, ISEPS includes the four 250 kW tunable 1 MHz RF power supplies for the

RF drivers, the starting filaments power supplies, the cesium oven power supplies and the bias power supplies for the extraction grid and the plasma grid. All of these are fed through a 100 kV insulating transformer. In fig. 1.18 the electrical scheme of the power supply system is shown. On the left side the 100 kV power supplies for the low voltage acceleration grid is shown; this has the role to polarize the whole plasma source and to carry the beam current, collected on the grounded components. Instead, the extraction grid power supply has the role to collect the ion current and electron current due to magnetic deflection on the grid itself. The transmission line connects all the high voltage components to their power supplies and to the high voltage deck. It is approximately 30 m long. A 1 x 1 m square shaped grounded screen (made by conductive panels) was chosen, together with a ground conductor dedicated to collect the ground current. The multi-conductor line, instead, is installed inside a 0.5 m conductive screen, polarized at -100 kV. The highest electric field is 0.6 kV/mm.

The crucial aspect of the protection against breakdowns between high voltage and grounded components has to be taken into account.

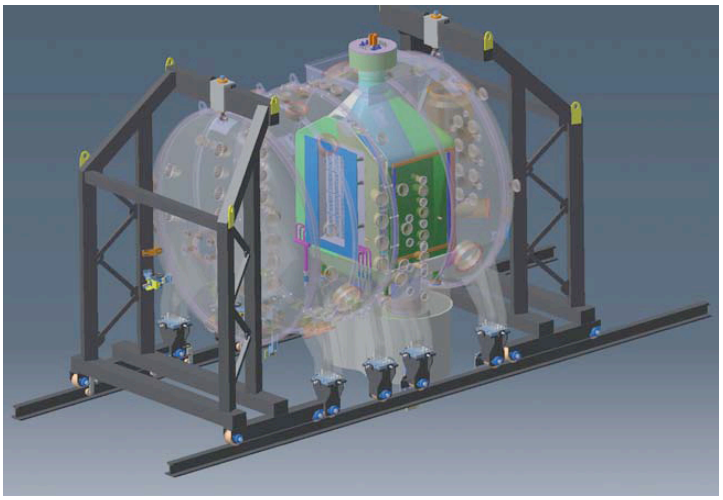

Figure 1.15: SPIDER design

MITICA

MITICA experiment is almost identical to the ITER NBI, so the description presented in 1.4 is applicable. In particular, the electrical power supply scheme is the same of fig. 1.13. The layout of the plant is shown in fig. 1.17.

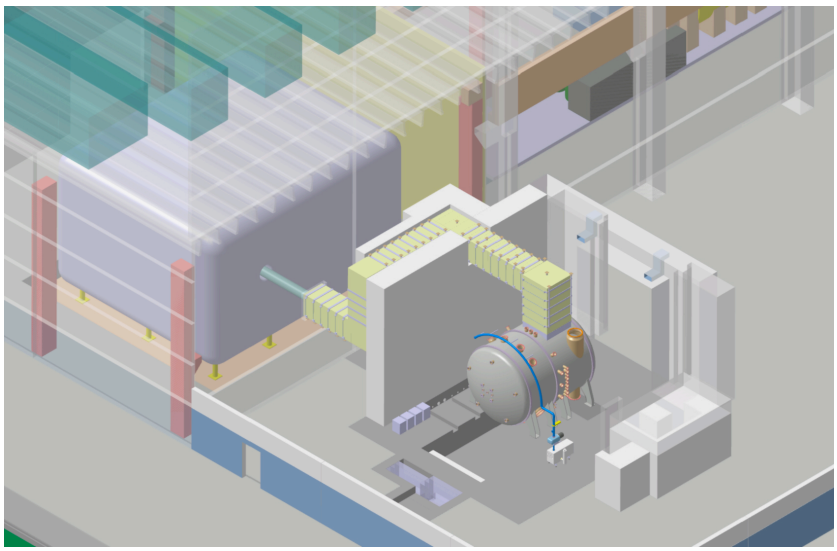

Figure 1.16: SPIDER layout

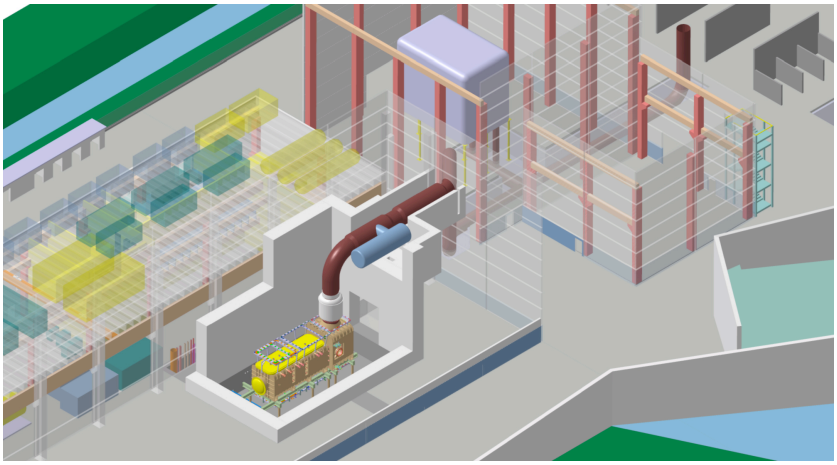

Figure 1.17: MITICA layout

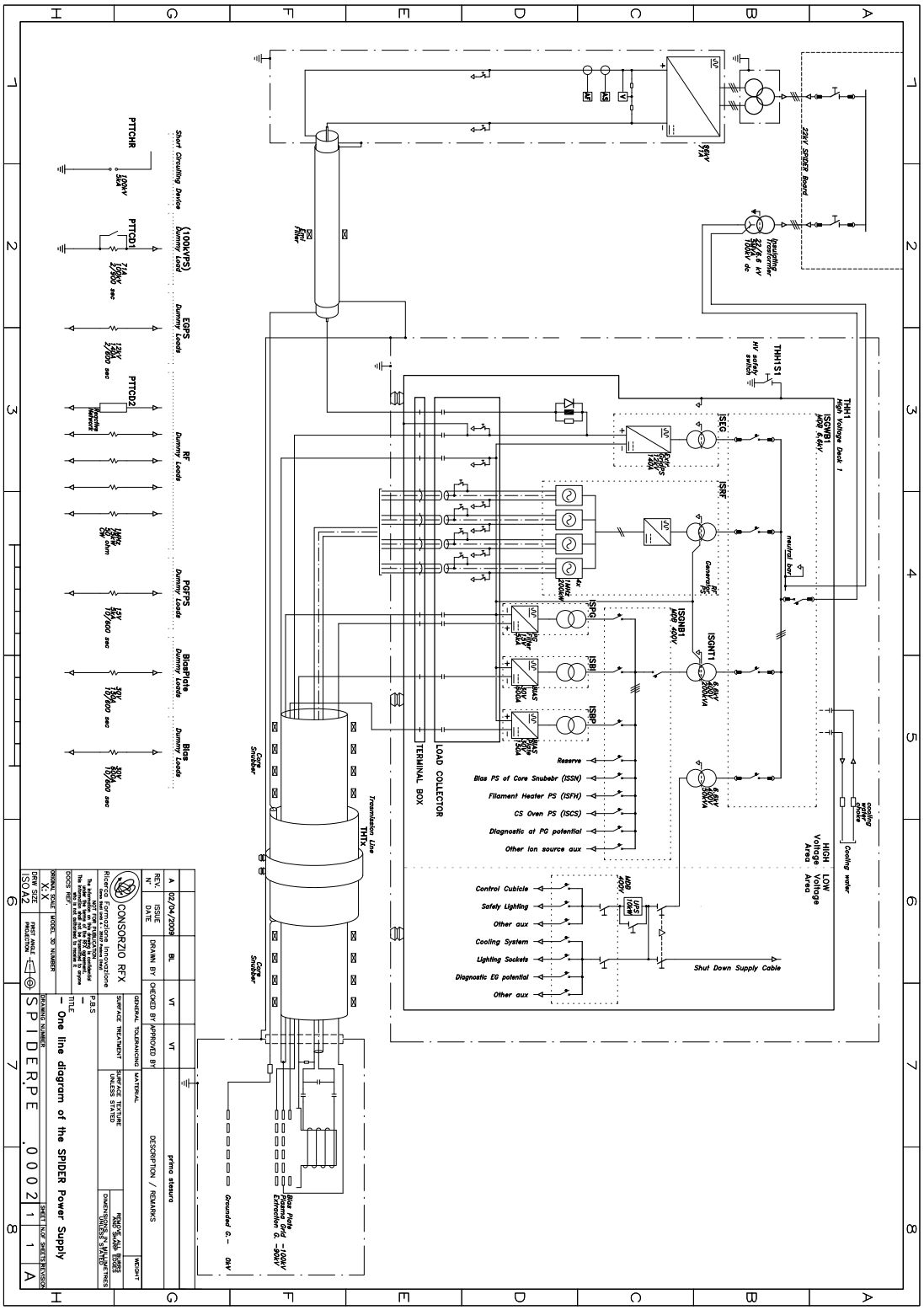

Figure 1.18: SPIDER power supply reference scheme

2

NBI high voltage operating conditions

Neutral beam injector works very close to breakdown limit. For this reason, breakdown between the accelerating grids is not an exceptional fault but it is considered in the ITER NBI a normal operating condition: the expected number of occurrences is in the order of 450000 along its whole life.

Certainly the maximum energy associated to each breakdown must be kept as low as possible, in order to avoid grid surface damaging, which can lead a significant decrease in the inter-electrode gap voltage holding capability. It has been found experimentally that when the deposited energy exceeds a threshold value the breakdown voltage level is reduced. This behaviour is called de-conditioning. The energy sustaining the arc between grids is stored in the capacitances of the system [7]; these capacitances are both concentrated (like in the output filter of the power supplies, the higher value, in the order of 10 kJ) and distributed along the system (i.e. the TL). During grid breakdown only a small fraction of this energy can be transferred to the grids, in order to maintain the voltage holding property to the required value; the highest allowed value is still an open issue, as there's not a large literature on this topic [8]. As a matter of fact, the present experience is mainly related to the relatively small gaps (< 20 mm). However, it seems that the allowed energy is in the order of less than 30 J for stainless steel electrodes and less than 50 J for Cu-Cr electrodes, with no decreasing of breakdown voltage. This is the reason why a proper campaign was proposed to be carried out on the CEA testbed in Cadarache (see par. 3.2).

Countermeasures have to be considered in order to dissipate the energy stored upstream the main bushing (separating transmission line and injector), considering e.g. the insertion of series resistors or implementing concentrated or distributed core snubbers along the transmission lines. On the other hand, up to now no mitigation strategy for the effects of stored energy downstream the bushing (mainly in the source itself) has

been provided.

The high overvoltages appearing across the internal conductors of the transmission line, and between the line and grounding, in consequence of a breakdown can lead also to several insulation problems; e.g. in principle, such overvoltages could introduce currents on the parasitic capacitances across primary and secondary side of step-up transformers, producing voltage and current fluctuations at the primary side, stressing the AGPS components. So these effects can have implications also on the aspects like the power supply protection strategy and the grounding connections.

2.1 High Voltage holding and conditioning in vacuum

The critical issues of the NBI HV insulation are related to different media, such pressurized gas and vacuum, with or without solid insulators. For each insulation type different mechanisms can lead to a breakdown. As far as the vacuum is concerning, some important issues have to be considered, as the reliability of the voltage hold-off and the effective conditioning procedures of very large electrode surfaces (e.g. the beam source); at the same time the system has to face the fast de-conditioning of the vacuum gap, caused by breakdown between the electrodes. The full voltage holding capability of the accelerator is achieved in a gradual process of conditioning, operating initially at a voltage as low as one third of the rated value [9].

As mentioned previously, for devices characterized by vacuum gap of this size, a very poor experimental background is achieved. So the detailed mechanism responsible for breakdown is not well understood yet [10, 11]. However, some works suggest that the maximum voltage insulation capability for large gaps is controlled by the total energy delivered onto the anodic surfaces. The most relevant property seems to be the so called "voltage saturation", or "total voltage" effect, which consists in the succeeding of a maximum voltage for breakdown, independent on the gap size and so on the electric field [12]. The behaviour hypothesized is shown in fig. 2.1, which reports a collection of results on different high voltage holding tests.

Another important effect for large gap is the gas pressure effect [13]: the voltage holding capability increases when the system operates at a pressure nearby 10^{-4} mbar. Maintaining the pressure at this level the performance of the system on voltage holding enhances. In particular, CEA testbed (for SINGAP experiments) has to work at about 7×10^{-4} mbar to avoid intense "dark current" [14]. Unfortunately this pressure level is not compatible with the ITER NBI requirements [15]. The dark current is a problem as it limits seriously high voltage operation (great absorption of power supply energy). Probably it depends on the HV conditioning of the system, and in particular on the surfaces condition (polishing level and imperfections). The physical process which cause this current is not understood yet. It seems however that gas desorption from electrodes can play an important role.

The conditioning procedure consists in the outgassing of electrodes surface by applying high voltage. Other treatments are necessary, as the surfaces have to be micropolished, rinsed and cleaned in ultrasonic bath; the baking in oven up to 500°C allows to

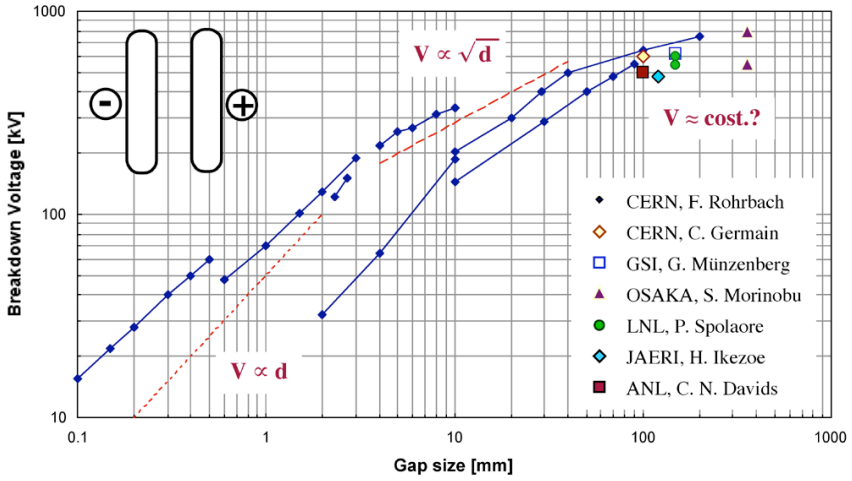

Figure 2.1: Breakdown voltage as a function of the gap distance for plane-parallel electrodes in vacuum

eliminate gas adsorption on surfaces. Some other factors are very important for the high voltage holding, like the choice of materials, both for insulating media (alumina instead of epoxy) and for conductors (stainless steel instead of aluminum). Finally the geometry of the electrodes has to be carefully designed, in order to obtain a nearly uniform distribution of the electric field.

2.2 Arc modeling for breakdowns

Up to now all the evaluations on the neutral beam devices equivalent circuits have been made considering for breakdown a very rough estimation, consisting in a constant voltage drop (in the order of 100 V), sometimes in series with a small resistance (in the order of 1 mΩ). Such assumption is clearly insufficient to study straightforward values like the arc energy dissipation, the arc current peak and the effectiveness of protective components (like core snubbers, series resistors, dampers etc., see chapter 3). A realistic model is then necessary not only to make a reliable evaluation of the high voltage breakdown effects on the different parts of the NBI circuit but also to to support the protection system design.

Circuital arc modeling has been already developed, mainly for power systems studies; in particular, these models simulate the current breaking processes in the circuit breakers (in compressed air, oil, SF_6 or vacuum) or the external flashover of air-insulated structures (bushing, spacers, disconnectors). These models consider arc as an electrical branch composed by a non-linear conductivity G(t), obeying to a particular differential equation and neglecting the inductivity. But, as already stated, presently there is a very few available literature for large gap breakdown modeling. A recent work [16] tried to adapt the available arc models introducing the adaptation to the vacuum environment. Starting from existing arc models (Mayr and Cassie models), a new model has been introduced, in which the main dissipating factor is radiation instead of convection.

2.2.1 The radiative model

The breakdown arcing which could occur inside the NBI accelerator is characterized by long gap (some centimeters) [12] so the radiative mechanism has an important contribution on energy dissipation. The following consideration can be done to assess the minimum length over which radiation overrides convection.

Considering a cylindrical plasma current of radius a, in which a current I flows, the solution of the pressure balance equation $\nabla p = \bar{j} \times \bar{B}$ yields the following pressure expression on the column axis:

$$p(0) = p_a = \frac{1}{4}\mu_0 j^2 a^2 = \frac{\mu_0 I^2}{4\pi^2 a^2} \tag{2.1}$$

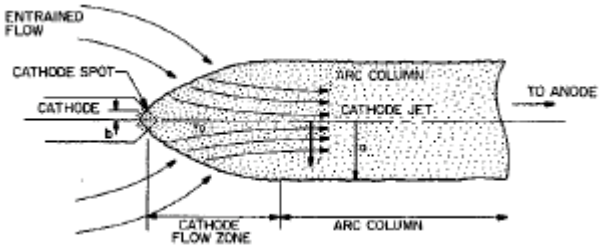

Figure 2.2: Cathode electrode jet flow

The arc starts in the cathode region with a small section spot [17] of radius b, see fig. 2.2; the pressure in this region is larger than in the arc column being expressed by (with $b \ll a$):

$$p_b = \frac{1}{4}\mu_0 j^2 b^2 = \frac{\mu_0 I^2}{4\pi^2 b^2}$$

The large pressure difference causes the flow of external gas developed around the arc cathode spot, which penetrated inside the arc column with the velocity v_{gas}

$$\Delta p = p_b - p_0 = \frac{\mu_0 I^2}{4\pi^2}\left(\frac{1}{b^2} - \frac{1}{a^2}\right) \cong \frac{\mu_0 I^2}{4\pi^2 b^2} = \frac{1}{2}\gamma v_{gas}^2$$

The gas velocity is then a linear function of the current:

$$v_{gas} \cong \frac{I}{\pi b}\sqrt{\frac{\mu_0}{2\gamma}} \tag{2.2}$$

To this gas flow the cooling process of the arc is associated; the power dissipated is then expressed by (from Cassie model [18]):

$$P_{conv} = c \cdot \gamma \cdot A \cdot v_{gas}\,(T_{arc} - T_{gas}) \tag{2.3}$$

In vacuum, the gas available to cool down the arc is substantially formed by metal vapors generated by the arc burning; in such environment the other mechanism responsible for cooling is radiation. Supposing the arc irradiates against a black body (emissivity

$\varepsilon = 1$), the power dissipated has the following expression:

$$P_{irr} = \varepsilon \cdot k_b \cdot A_{ext} \cdot (T_a^4 - T_0^4) \cong k_b \cdot A_{ext} \cdot T^4 \tag{2.4}$$

being $T_a \gg T_0$, where $A_{ext} = 2\pi al$ is the irradiating surface of the arc and k_b is the Boltzmann constant. In order to evaluate the main dissipation mechanism it is necessary to verify which is the arc gap length above which the radiation exceeds convection $P_{irr} \gg P_{conv}$. Substituting the value of v_{gas}, A_{ext} and A, a condition on gap length is derived:

$$l \gg \frac{a}{2} \cdot \frac{I}{\pi b} \cdot \sqrt{\frac{\mu_0}{2\gamma}} \cdot \frac{c\gamma}{k_b T^3} \tag{2.5}$$

The value of vapor gas density γ and of the heat capacity c can be derived from the equations:

$$\gamma = \frac{P_M}{N_A} n_i \qquad c = \frac{2k_b n_i}{\gamma}$$

The table 2.1 reports the value adopted for estimation. Substituting these parameters in eq. 2.5 we obtain:

$$l \gg 5 \text{ cm}$$

As in our case the gap length is in the order of 30 cm, thus the radiative model applies.

Table 2.1: Parameters for radiative versus convective arc estimation [16]

I [A]	Arc current	1000
a [m]	Arc radius	0.005
b [m]	Cathode spot radius	$5 \cdot 10^{-5}$
P_M [kg/mol]	Molar weight	74
T [K]	Arc temperature	5000
N_A [mol^{-1}]	Avogadro number	$6.02 \cdot 10^{23}$
k_b [J/kg]	Boltzmann constant	$1.38 \cdot 10^{-23}$
n_i [m^{-3}]	Ion density	10^{23}

Then starting from the same assumptions of Cassie model [16] (except dissipative mechanism) and in particular from the final differential equation involving the conductance:

$$\frac{1}{G} \cdot \frac{dG}{dt} = \frac{1}{\tau_0} \left(\frac{v^2}{V_0^2} - 1 \right) \tag{2.6}$$

being $A_{ext} = 2l\sqrt{\pi \cdot A}$ and $i = j \cdot A$, after some calculation we obtain:

$$\frac{1}{G} \cdot \frac{dG}{dt} = \frac{1}{\tau_0} \left(\frac{v^2}{V_0^2} - \frac{K}{\sqrt{|i|}} \right) \tag{2.7}$$

where A_0 is a reference column section and [19]

$$K = \sqrt{jA_0} \quad \tau_0 = \frac{c\gamma\sqrt{A_0}}{k_b T^3 2\sqrt{\pi}} \quad V_0 = \sqrt{\frac{l^2 k_b T^4 2\sqrt{\pi}}{\sigma\sqrt{A_0}}} \quad \sigma = \frac{1.53 \cdot 10^{-2} \cdot T^{\frac{3}{2}}}{\ln\left(\frac{1.24 \cdot 10^7 \cdot T^{\frac{3}{2}}}{\sqrt{n_e}} \right)}$$

Referring to a peak current expected I_M the final relationship for the radiative model becomes:

$$\frac{1}{G} \cdot \frac{dG}{dt} = \frac{1}{\tau_0} \left(\frac{v^2}{V_0^2} - \sqrt{\frac{I_M}{|i|}} \right) \tag{2.8}$$

This equation is not valid for current approaching to zero (as it becomes inconsistent). We can note a direct dependance of arc conductance on current. From calculations made in [16] it appears that this model is more realistic and also more conservative than the basic reference model, i.e. a constant 100 V voltage drop. An important part of the experiments on the CEA testbed will be devoted to characterize experimentally the model, by the measure of the voltage–current characteristic of breakdown.

2.3 Present countermeasures against breakdown effects

Up to now, with accelerating voltages up to 200 kV, protection was based on dc circuit breakers, able to disconnect quickly the high voltage power supply from the load. In particular, for the early operation of Jet experiment, a series tetrode was used, equipped in parallel by an ignitron crowbar, triggered in case of failure [20].

ITER AGPS instead will use solid-state inverters, combined with insulating transformer and diode rectifiers. Modern converters have a response much faster than thyristors so an adequate protection can be assured without physically disconnecting the power supply [21]. But, due to the high voltage level (1 MV) a solution with dc breaker would not be applicable with present technology.

Presently, the protection strategy for the highest energy NBI relies, in addition to the fast switch off of the power electronic converters, on the following actions: first, by minimizing the capacitive energy, mainly stored in the high voltage power supplies output filters; secondly, by inserting dissipative components (resistors and magnetic snubbers).

2.3.1 Concentrated Core Snubber

As the timescale of breakdown is beyond the intervention of any active protection, suitable passive components have to be inserted in the circuit. The absence of dc circuit breakers diverting current on resistive paths changes the dynamic of breakdown current. In fact, the presence of diode bridge makes the current driven by the circuit inductance and flowing into the diodes over a longer decay time (see fig. 2.3).

A core snubber consists in a hollow cylinder of ferromagnetic material, surrounding the high voltage inner conductor of the NBI transmission line. A resistor may act as a secondary winding of the core snubber, providing power dissipation. Moreover, a bias circuit is often required to increase the available flux swing before core saturation. A core snubber is represented, in a circuital model, as a saturable inductance and a resistance connected in parallel [22, 23].

In the present design of the ITER NBI two core snubbers are foreseen, a CS1 positioned at the end of transmission line 2 and a CS2 positioned at the end of transmission

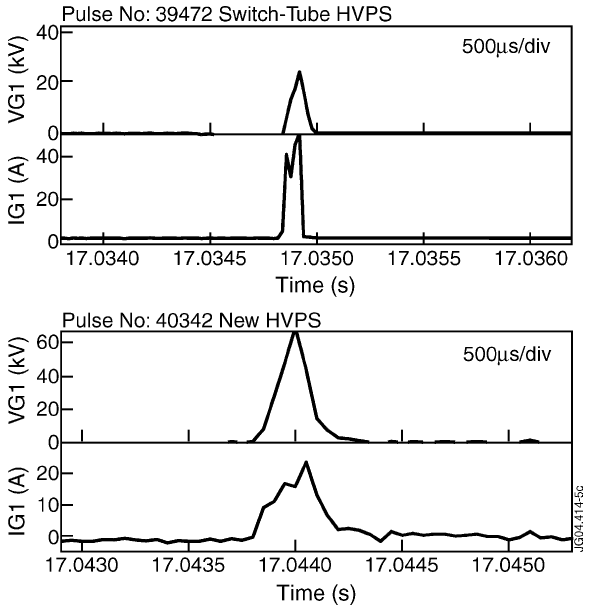

Figure 2.3: Comparison of behaviour between conventional breakers and new switching modules in response to a breakdown for Jet [21]

line 3. Practical constraints don't allow to install other components inside the injectors. This consideration has an impact on the CS design. The capacitive stored energy downstream the CS2, i.e. in the last TL section, in the bushing, in the source and in the accelerator is evaluated in the order of 500 J: when a discharge occurs this energy determines a current peak calculated in the order of 20 kA. Therefore, designing passive protections to reduce the current peak from the protected part of the circuit much below 20 kA would bring little benefit, since the unprotected part of the circuit will cause a 20 kA peak in any event.

A tentative estimation of CS1 and CS2 parameters (with linear inductances) was made in [24], considering 10 kA as maximum current peak due to the portion of the circuit upstream the core snubbers; the snubber resistance calculated is in the order of 100 Ω while the inductance is 140 μH for CS1 and 95 μH for CS2. In the same work the insertion of a 7 Ω resistance in series to the high voltage conductor is suggested, to dissipate part of the energy during the fault and limit to 15 J the arc energy. Further studies [25, 26] on a more detailed MAMuG model provided the following values for core snubbers: 275 Ω and 0.9 mH for the CS1 while 30 Ω and 0.1 mH for CS2; values for the series limiting resistances vary from 50 Ω for return conductor to 400 Ω for 800 kV intermediate conductor. Arc energy is limited within 20 J. The drawback is that high values for series resistances cause a great energy dissipation during stationary phase.

To absorb the energy at the breakdown, a core material which has enough inductance without saturation is required [27]. This means that the magnetic core materials should have high saturation magnetic flux density, see fig. 2.4(a), and high permeability

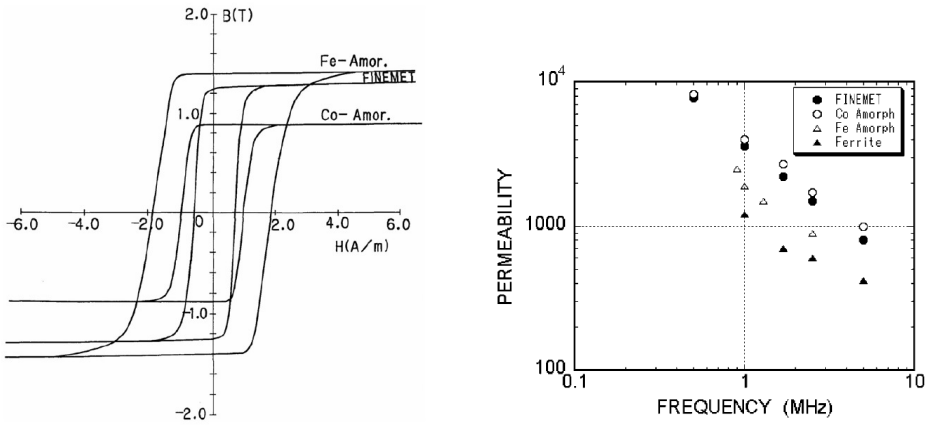

(a) B–H curve (b) Permeability vs. frequency

Figure 2.4: Magnetic properties of materials for the core snubber [3]

for high frequency surges, see fig. 2.4(b). Hence not only saturation magnetic flux is important, but also dynamic magnetic properties (i.e. the dependance of relative magnetic permeability with frequency should be as stable as possible). A work described in [28, 3, 25] compared magnetic properties of different materials. Fe-based nanocrystalline soft magnetic material called Finemet® [29], developed by Hitachi Metglas Ltd.® was chosen as an adequate compromise for the NBI core snubbers.

2.3.2 Active protections

A paramount role is played by the the AGPS inverter for load protection. In principle, in consequence of a grid breakdown the inverter has to remove the AGPS output voltage as quickly as possible. The protective strategy provides the opening of the circuit, instead of shorting, as it allows to feed back to the low voltage side some of the energy of the insulating transformer leakage inductance, by the inverter freewheeling diodes, so reducing the energy transferred downstream to the main circuit.

The speed of response of this system, considering recent devices like Integrated Gate Commutated Thyristors (IGCTs) and taking into account the time needed by the measurement and acquisition systems, can be in the order of 100 μs. The effect of 100 μs inverter switch off was evaluated by NB equivalent circuit [24]: no impact was found as the AGPS short-circuit current grows on a longer time scale. Thus, the additional fault energy delivered by the AGPS during the delay is quite negligible (0.2 J).

3

Passive protections: new concepts

In the present ITER NBI reference design the protection against the grid breakdown relies basically on the concept of the concentrated core snubber, as described in the previous chapter. Actually, this solution appears not fully suitable to cope with the high voltage issues previously described, considering the reliability requirements of the system:

1. in the ITER NBI part of the electrostatic energy (some hundreds Joules) is stored in the stray capacitances of the HV bushing and of the source screen, i.e. downstream the core snubber, so that it cannot limit the breakdown current peak (determined only by the stray inductivity and arc resistance) and will have poor effect on limitation of the energy stored downstream, because the CS decouples the upstream section of electrical circuit (transmission lines, high voltage decks and dc generators) from the downstream section (HV bushing and accelerator);

2. for the same reasons, the CS cannot affect in great extent the EMI occurrence, because of the free (poorly damped) evolution of breakdown current;

3. transmission line internal breakdown will give rise to almost un-damped travelling waves, causing large voltage reversals;

4. it is a huge, heavy and cumbersome component, due to the large amount of magnetic flux (Volt-second) that the core has to sustain without going into saturation;

5. the high value of residual flux for the magnetic core needs a strong biasing circuit (tens of Amperès circuit). This circuit requires to be protected from overvoltages.

Also the use of limiting resistor in series to the main conductors, as reported in [25], has large drawbacks due to the large Joule power dissipation (up to tens kW).

So a different strategy has to be developed for large-scale NBI. An alternative approach is here proposed: it consists on the realization of a comprehensive mitigation strategy, against grid damage, EMI and internal insulation failures, which is based on the resistive connection to ground (by a damping resistor DR) of the last accelerating grid (the grounded grid GG) and on the installation of a distributed core snubber (DCS), evenly installed along the transmission line instead of being concentrated at its end.

3.1 Damping resistor

3.1.1 Concept

The DR concept is based on the fact that in case of a full short circuit of all the accelerating grids AGs (the most severe and the most probable event), arc current is collected by the Grounded Grid GG. The limitation of the current peak and of the arc energy can be then obtained by means of a resistive connection of GG to ground [30]. The main advantage of this solution is that during stationary phase the DR is not loaded by the full beam current (∼40 A), but only by a small fraction (∼10%), carried mainly by the electrons intercepted by the GG, so that the DR is subjected to a moderate dissipation. In fig. 3.1 the breakdown on the circuit is sketched, where the capacitances storing the energy downstream the core snubber are indicated. During breakdown, the GG is subjected to a voltage pulse: for this reason, the GG support has to be appropriately insulated to ground (see the installation inside the vessel in [31], fig. 3.2). The DR value has to be determined as a trade off between the breakdown current reduction and the GG over-voltage.

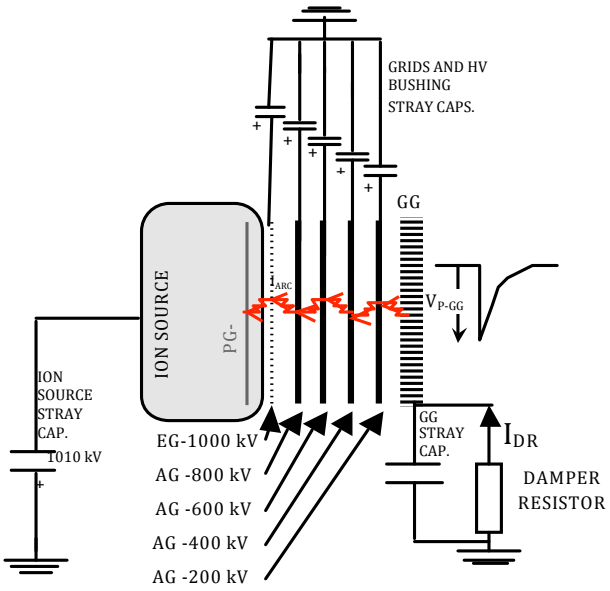

Figure 3.1: Schematic of the damping resistor electrical connections

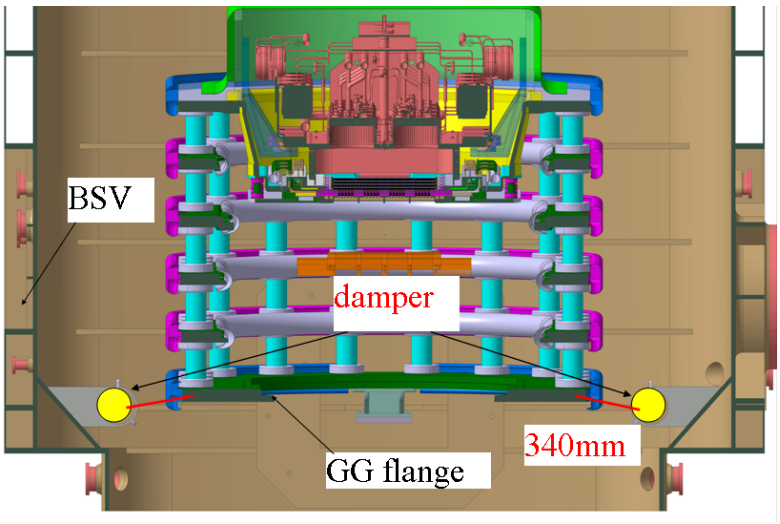

Figure 3.2: Installation of the damper resistors inside the NBI vessel

A rough estimation on the effects of the GG voltage during pulse in presence of beam was done. As a matter of fact, we expect the voltage induced on the GG to drive current not only through its capacitance but also through the space charge in the volume between the GG and the neutralizator. In circuital terms this phenomenon represents a conducting path in parallel to the damper branch, diminishing its effect. The value of calculated current drained by this phenomenon is in the order of 5 % of the current drained by the damper, so its efficiency should be maintained also in presence of the beam.

3.1.2 Integration on the NBI model

The DR effectiveness has been evaluated using a detailed circuital model for fast transient simulations, representing the most up-to-date MITICA circuit arrangement [26]. Three values of DR resistor have been implemented: 20, 40 and 100 Ω. The parameters considered to assess the effectiveness of the DR are:

1. Grid protection: arc current peak and arc energy in each grid (arc modeled as a constant voltage drop);

2. EMI reduction: high-frequency rms current and current peak of the current injected on the grounding system;

3. Insulation protection: overvoltage and voltage reversal across the five stages S200, S400, S600, S800, S1000 of the main HV bushing, connected to the corresponding Accelerating Grids.

Fig. 3.3 shows the first microsecond of the arc current short circuiting the 200 kV grid and the grounded grid. Referring to table 3.1, DR limits the arc current peak in

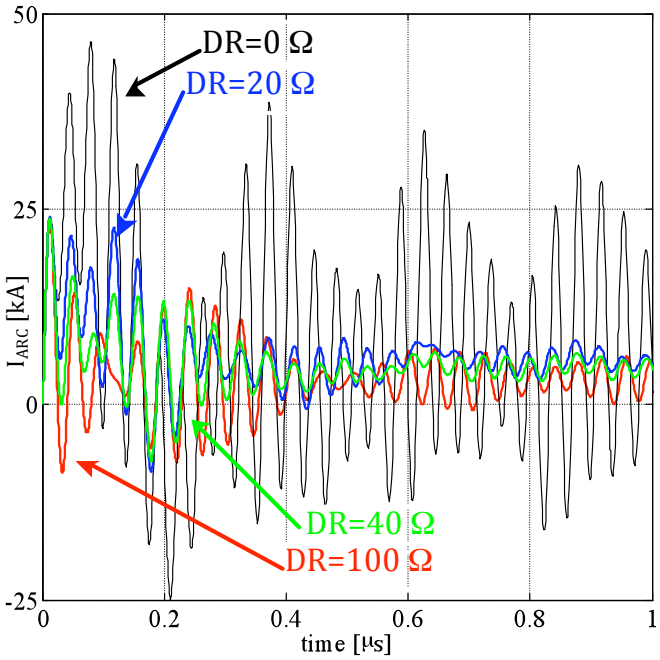

Figure 3.3: Arc current in the gap between 200 kV accelerating grid and grounded grid

the gaps, with a decreasing efficacy from the first gap (AG200-GG) to the others. We can also observe that the arc current peak in the AG200 gap is independent of the DR value: this is because the GG stray capacitance acts as a short circuit in the first tens nanoseconds. As a matter of fact, this current peak will be very likely determined by the initial behaviour of the arc breakdown (highly resistive) and not by the DR. The actual DR efficacy consists in the remarkable increase of the arc current damping, as shown in fig. 3.3, with beneficial effect on the estimated energy. In terms of EMI reduction, the effect of the DR is also positive, both for current peak and for high-frequency rms current injected in the ground system (see tab. 3.3). In terms of voltage stresses in the HV bushing, the damper presence affects only the voltage of the first insulating ring (between S200 and ground), being subjected to over-voltages increasing with the DR value; there is instead a little influence on the voltage reversal across other rings. As far as the energy dissipated in the damper is concerned, the 20 Ω DR dissipates 5.5 kJ, the 40 Ω DR 8 kJ and the 100 Ω 11.5 kJ for each breakdown. The GG overvoltage is 580 kV for DR20, 650 kV for the DR40 and 770 kV for the DR100 (see tab. 3.2). The performed analyses indicate that the efficacy of the damper is remarkable in limiting the arc energy and the EMI level, and it is little sensitive to the DR value. On the contrary, the higher the DR value, the higher are the AG200 and the GG overvoltages: for this reason, the optimum value of the DR is in the range of 20 Ω.

Table 3.1: Synoptic of the damper resistor effects on grids [30]

Case	Grid breakdown				
DR [Ω]	EG1000	AG800	AG600	AG400	AG200
	Arc current peak [kA]				
0	29	46	46	42	46
20	27	39	39	32	24
40	26	37	37	30	24
100	26	35	35	29	24
	Arc energy [J/V]				
0	0.19	0.20	0.18	0.17	0.19
20	0.16	0.15	0.15	0.14	0.11
40	0.15	0.14	0.14	0.13	0.10
100	0.14	0.14	0.13	0.12	0.08

Table 3.2: Synoptic of the damper resistor effects on bushing voltages [30]

Case	HV bushing voltage stresses									
DR [Ω]	S200	S400	S600	S800	S1000	S200	S400	S600	S800	S1000
	Voltage reversal [%]					Overvoltage [%]				
0	80	48	50	67	55	0	0	0	0	0
20	0	50	43	52	56	190	0	0	0	0
40	0	56	45	50	53	250	0	0	0	0
100	0	63	50	51	59	300	0	0	0	0

Table 3.3: Damper resistor effect on ground current [30]

Case	Ground current	
DR [Ω]	$I_{HF\ rms}$ [A]	I_{peak} [kA]
0	550	2.4
20	400	1.6
40	350	1.3
100	250	0.9

3.1.3 Design and assembly for CEA testbed

A first prototype of a damper was designed (see fig. 3.5 and fig. 3.4) and realized (see fig. 3.6) by RFX workshop. In the following the design and the technical description of the damper are reported. This DR was delivered to CEA Cadarache (F) laboratory, where it was assembled on the high voltage testbed to be experienced and tested. The design of the DR was realized according to the testbed constraints, in particular regarding the available space. In addition we started the design taking into account the results of the simulations performed on the equivalent circuit (reported in the section 3.2). With the aim to find suitable values of resistance three different values were chosen (20, 40 and 60 Ω). As a consequence, we needed to design a common mechanical structure with removable resistors instead of building three different dampers. In the tab. 3.4 predicted values of maximum voltage and current stressing damper and of energy dissipated for each pulse are summarized. These values were calculated in the worst case for the plant configuration, i.e. with the maximum level of stored energy.

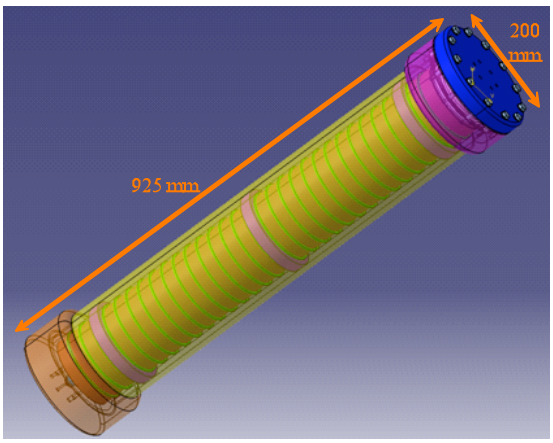

Figure 3.4: Damper resistor CAD model with main dimensions

Table 3.4: Summary of electrical stress for the CEA testbed damper

DR [Ω]	Max current [kA]	Max voltage [kV]	Energy dissipated [J]
20	25	500	1445
40	18	690	1448
60	13	800	1450

3.1.3.1 Choice of resistors

For the choice of number and type of resistors we had to take into account the damper total dimensions constraint: the total length available was 950 mm and the diameter 200 mm; this was not easy because we should have a large number of thin resistors or a small

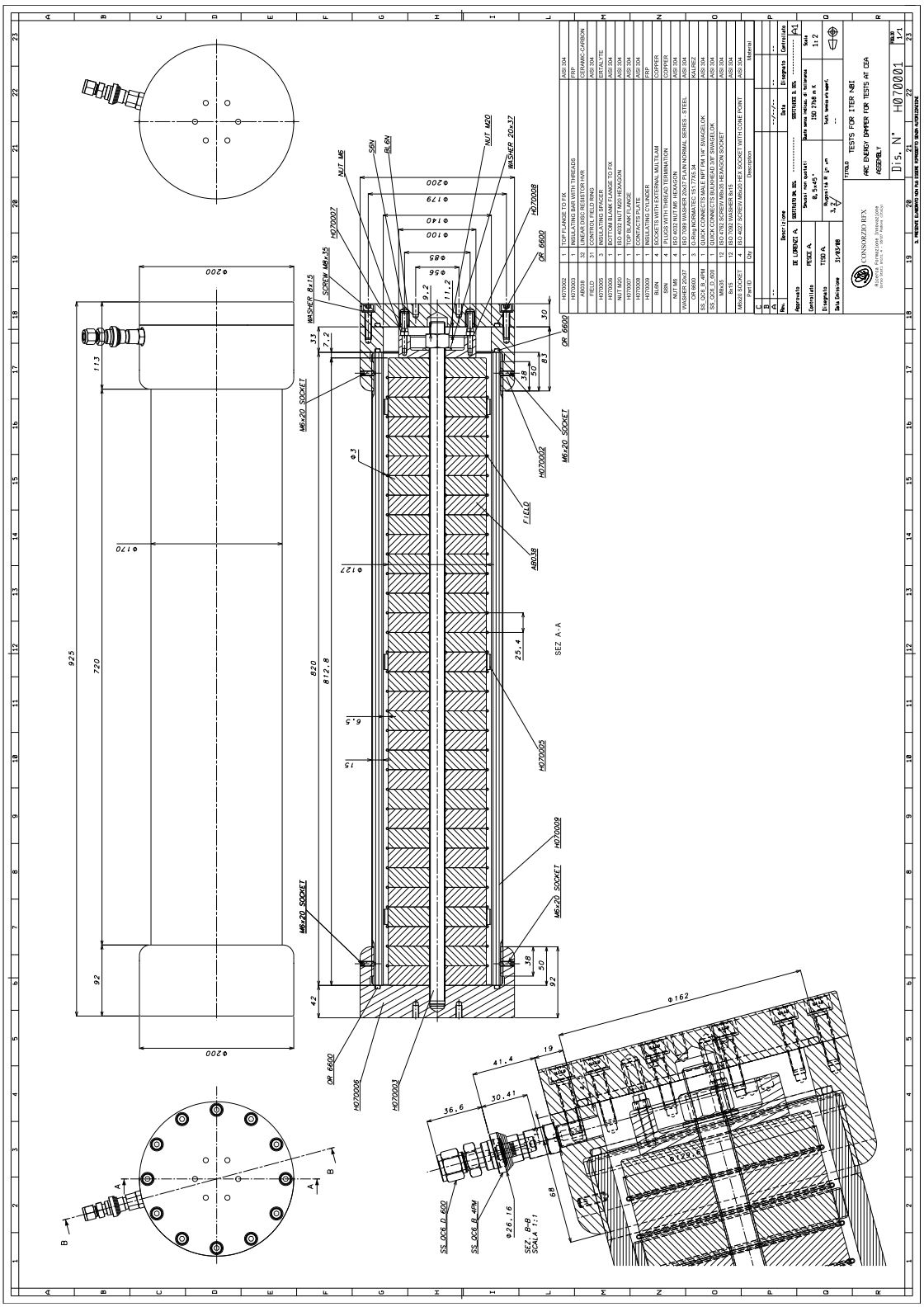

Figure 3.5: Damper resistor final design

Figure 3.6: Picture of the damper resistor assembled

number of wide ones to share such very high voltage as reported in tab. 3.4. Then we had to fix a parameter, the resistors thickness, to the standard value provided by the company HVRinternational® for all the three damper configurations, varying only the value of resistivity. This value is $s_{disk} = 25.4 \pm 0.4$ mm. We chose a number of disk $n_{disk} = 32$ with the largest possible area for the best voltage withstand, within the limit on diameter. This value is defined by the equation:

$$V_{ws} = s_{disk} \cdot C_{ins} \cdot \sqrt[1.2]{\log\left(\frac{\rho}{2.54}\right)}$$

where C_{ins} is a constant value equal to 4.3 for air insulating and 8.0 for SF_6 gas insulating. The disk model chosen was AB038 from HVRint.® [32] catalogue. The outer diameter was $D_0 = 12.7$ cm and the inner $D_i = 2$ cm. The overall length for the stack of resistors became $l_{stack} = s_{disk} \cdot n_{disk} = 25.4 \cdot 32 = 813$ mm. From data-sheet we report the main parameters for resistors:

Volume: $vol = 314$ cm^3

Thermal time constant: $\tau = 3570$ s

Maximum Joules energy: $J_{max} = 78500$ J

Dimensions ratio: $A/L = 48.6$ cm

Weight: $P_{disk} = 0.705$ kg

The following formulas are valid for all the configurations. They are calculated and summarized in tab. 3.5. Uncertainty of resistance is ±10 % for all the three values.

Resistance per disk: $R_{disk} = R_{damper}/n_{disk}$

Resistivity of disk: $\rho = R_{disk} \cdot A/L$

Maximum voltage applied per disk: $V_{disk} = V_{tot}/n_{disk}$

Maximum voltage withstand per disk: $V_{ws-air} = s_{disk} \cdot 4.3 \cdot \sqrt[1.2]{\log\left(\frac{\rho}{2.54}\right)}$ (AIR)

Voltage safety factor: $K_{air} = \frac{V_{ws-air}}{V_{disk}}$

Maximum voltage withstand per disk: $V_{ws-SF6} = s_{disk} \cdot 8 \cdot \sqrt[1.2]{\log\left(\frac{\rho}{2.54}\right)}$ (SF_6)

Voltage safety factor: $K_{SF6} = \frac{V_{ws-SF6}}{V_{disk}}$

Energy dissipated per disk: $E_{disk} = E/n_{disk}$

Temperature rise for each impulse: $\Delta T = \frac{E_{disk}}{vol \cdot c}$

Peak temperature rise (repetitive impulsing hypothesizing a repetition rate $\delta = 60$ s): $\Delta T_f = \frac{\Delta T}{1-e^{-\delta/\tau}}$

Table 3.5: Summary of damper parameters in the three configurations

	20 [Ω]	40 [Ω]	60 [Ω]
R_{disk} [Ω]	0.625	1.25	1.875
ρ [Ωcm]	30.38	60.75	91.125
V_{disk} [kV]	15.6	21.9	25
V_{ws-air} [kV]	11.6	14.3	15.8
K_{air}	0.74	0.65	0.63
V_{ws-SF6} [kV]	21.6	26.6	29.4
K_{SF6}	1.38	1.21	1.18
E_{disk} [J]	45.2	45.3	45.3
ΔT [°C]	0.07	0.07	0.07
ΔT_f [°C]	2	2	2

As far as the energy load is concerned, the three resistors have large safety margin. Instead, the voltage withstand capability is more slight. Looking at the tab. 3.5 air appears not suitable because it assures no safety margin. SF_6 insulation gives instead adequate insulation reliability; as a matter of fact we have the safety factor larger than unity for all cases. In addition, the voltage withstand capability is based on LIWV (light impulse withstand voltage) waveform, which is more strict than our case; so that the actual safety margin would be likely larger. For this reason, even if voltage distribution would be uneven in the range of ±10 % (a great value, in our case) the withstand capability will be in any case assured. In fig. 3.7 a picture of the resistors used is reported.

Figure 3.7: Disk resistors used for the damper

3.1.3.2 Design of mechanical structure

Resistors are stacked along an insulating tie rod, whose diameter is equal to D_i=2 cm. The material should be a fibre reinforced plastic (in our calculations we considered Epoglass®). This stack of resistors is clamped by a proper tightening torque, whose value is provided by the data-sheet. The mounting force to provide good electrical inter-disk contact is:

$$F_{mounting} = 120g \cdot (D_o - D_i)^{0.7} = 6200 \text{ N}$$

Such force is applied as a tensile stress to the tie rod; the corresponding value is:

$$\sigma_{rod} = \frac{F_{mounting}}{\pi \cdot r^2} = 20 \text{ MPa}$$

This value is safe in comparison to the value of resistance to tensile stress for the plastic fibre: $\hat{\sigma}_{tensile} = 270$ MPa. As a precaution we calculated the maximum deflection of the resistors stack around the tie rod without tightening torque (system modeled as beam simply supported at both ends, the worst case) and its correspondent maximum stress:

$$M_{max} = \frac{1}{8} p \cdot L^2 = 23.6 \text{ Nm}$$

$$\text{Moment of inertia: } I = \frac{\pi}{64}\Phi^4 = 7.85 \cdot 10^{-9} \text{ m}^4$$

$$\sigma_{flex} = \pm\frac{M_{max} \cdot r}{I} = 30 \text{ MPa}$$

$$y_{max} = \frac{5}{384} \cdot \frac{p \cdot L^4}{E \cdot I} = 5 \text{ mm}$$

According to these calculations the deflection should be rather low and the tensile stress as well. However, to be safer, we put three insulating perforated Ertalyte® spacers inside the SF_6 space, in order to partially sustain the weight of resistors stack and limit the tie rod deflection. The same material of the inner tie rod was used for the external containing cylinder. This cylinder has to contain the insulating gas SF_6 with a pressure of 1 bar absolute (vacuum outside). The cylinder is subjected to the following tensile tensions:

Longitudinal tension: $\sigma_p = \frac{p \cdot r}{s} = 0.52$ MPa

Stress by closures: $\sigma_{cap} = \frac{p \cdot \pi r^2}{\pi \cdot (r_{ext}^2 - r_{int}^2)}) = 0.21$ MPa

Both are safe enough compared to the value of resistance to tensile stress.

3.1.3.3 Electrical contacts

The electrical contact between the damper and the main circuit is assured by two stainless steel enclosures. The top element is composed by a disk fixed by screws on the top of the top flange. This flange is provided aside of a hole which hosts the valve for air extraction and gas filling. The internal part of the upper disk is equipped by four Multicontact® sockets. The plugs, instead, are inserted on the contacts plate. This is forced to lean on the upper resistor disk to guarantee good electrical contact. Individual link socket–plug is able to sustain current peaks up to 8 kA each. The bottom of the damper is composed by a single steel element, screwed to the insulating cylinder. On the inner part, in the middle, the tie rod is screwed too. Both the top and the bottom steel disks are provided by six holes for the assembly on the external circuit.

3.1.3.4 Vacuum seals

As the damper has been installed in vacuum for the seal of the internal chamber (filled in SF_6, as already described, or also in helium or dry air) three Du Pont Viton® fluoroelastomer O-rings seals have been inserted. Two are inserted on the upper enclosure and one on the lower one. The first has to guarantee sealing between the top blank disk and the top flange (steel-to-steel) while the others between the terminations of the insulating cylinder and the flanges (epoxy-to-steel). Finally, the containing structure was also provided with a valve for air extraction and gas pumping.

3.1.3.5 Weight

The total weight of resistors is nearly 25 kg while solid insulators weight is 15 kg. Instead mechanical stainless steel parts weight is 25 kg. Total weight is then about 65 kg.

3.2 CEA testbed modeling and simulation results

To test the effectiveness of the damper resistor an experimental campaign was settled up on the 1 MV vacuum testbed at CEA Cadarache (ex SINGAP). The damper was required also to limit the strong currents foreseen for the arc tests. The main aim of the campaign is the study of the effects of energy deposition by arcing on the electrodes and, secondarily, the evaluation of a proper arc model for long gaps. The plant has very large dimensions (some m long), and in the past reached high voltage up to 800 kV. The nominal power for the power supply is in the order of some kW. The distance between the electrodes is adjustable from few centimeters to some tens centimeters, by means of a movable cathode fixed to a trolley, in order to study the effects of gap length on the discharge.

Due to the large dimensions it was soon clear it would be difficult to obtain a high accurate model of equivalent circuit only by measuring the present circuit. A bad model could drive to make experiments less precise. So we decided to implement an equivalent circuit by analytical calculations starting from physical geometry, prior to the experimental phase, and then perform calculations in different scenarios. A further comparison between results and experimental data would validate the model. The SimPowerSystem tool of Matlab Simulink® code was used to build the model and perform simulations.

We subdivided the model of the plant in different subgroup, as the geometry is quite complicated. The overall view of the plant, split in the different parts, is reported in fig. 3.9, while a CAD model is in fig. 3.8.

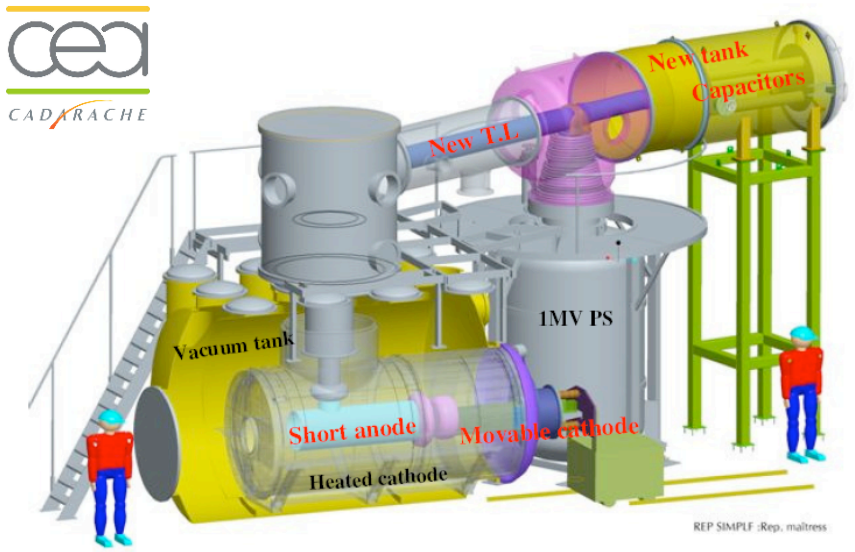

Figure 3.8: CAD model of CEA testbed

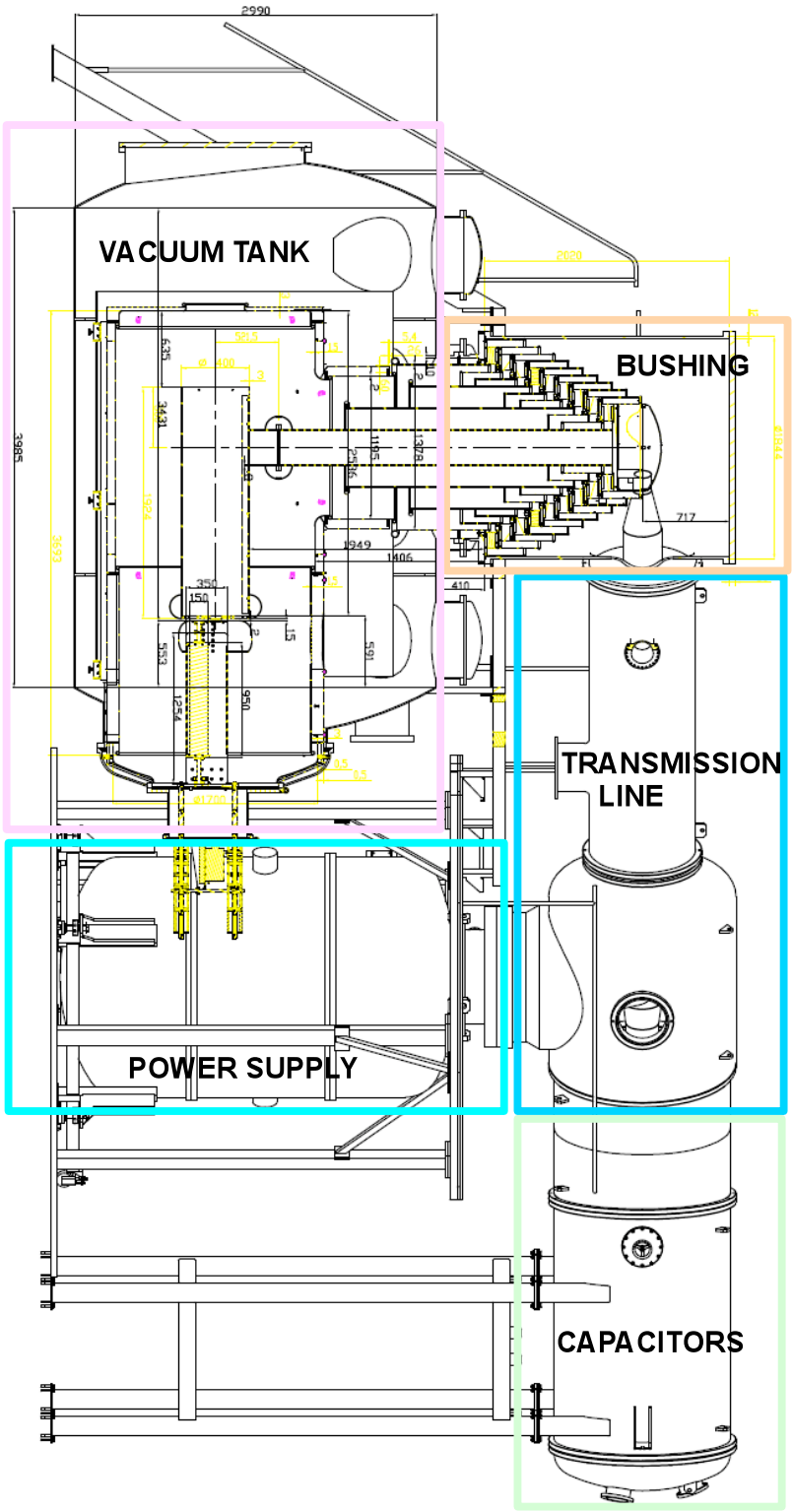

Figure 3.9: Overall scheme of CEA experimental testbed

3.2.1 Power supply and Transmission line

The power supply system was modeled as a series of a 1 MV dc generator and 1 MΩ resistor, in parallel to an external additional capacitor with a capacitance adjustable between 400 pF and 2.2 nF. Analyses were done with the highest value (the worst in terms of electrostatic energy stored). Fig. 3.10 shows the transmission line, about 4 m long. It was subdivided in three parts: two tanks connecting the line to the bushings at the ends, modeled as pure capacitances, and the line itself, modeled as a "T" cell. The resulting model for the power supply and transmission line is reported in fig. 3.11, while tab. 3.6 summarizes the values analytically calculated.

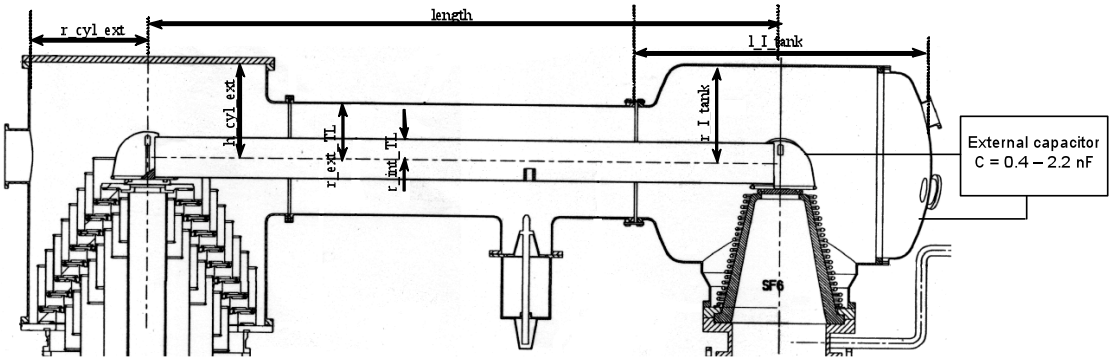

Figure 3.10: Overall view of the transmission line

Table 3.6: Electrical parameters for CEA power supply and transmission line model

Name	Value
C_I_tank	91 pF
C_cyl	68 pF
C_TL	190 pF
L_TL_1 = L_TL_2	348 nH
R_TL_1 = R_TL_2	305 $\mu\Omega$
L_I_tank	408 nH
R_I_tank	132 $\mu\Omega$
L_input	628 nH
R_input	29 $\mu\Omega$
C_input	2.2 nF
R_series	1 MΩ
Voltage	1 MV

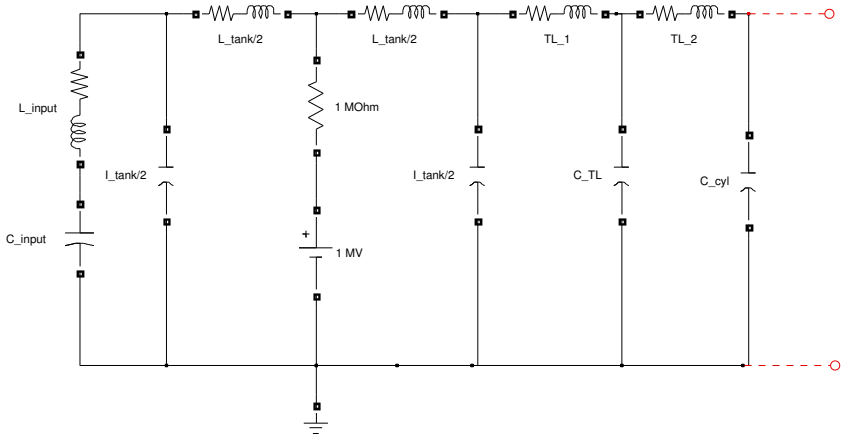

Figure 3.11: Power supply and transmission line electrical model

3.2.2 Main bushing

The main bushing is a very complex structure because it is not cylindrical but conical shaped, with 9 stages and with conductors and shields not fully faced each other. Fig. 3.12 shows a section of the bushing, while fig. 3.13 plots the equivalent electrical model. The 9 insulating stages are each subjected to a voltage equal to $1000/9 = 111$ kV. Insulating rings of stages are made of epoxy resin, with a a dielectric constant equal to 4. In parallel to each epoxy ring an equivalent resistance of 100 MΩ is inserted, with the aim to control the distribution of voltage during the dc phase. To control electrical field nearby the insulating rings some metallic shields at both sides are installed (see fig. 3.12). Tab. 3.7 summarizes the parameters of the bushing model, where "Cgr_ij" represents the capacitance of the i^{th} external shield toward ground, "Chv_st$k$ the capacitance of the k^{th} internal shield toward the inner high voltage conductor and "C_stage_l" the capacitance due to the l^{th} insulating ring.

3.2.3 Vacuum tank

The inner conductor of the vacuum tank is the anode, coaxial with the cathode, connected to the grounded external shield, the tank (see fig. 3.9 in the pink box "vacuum tank"). The external tank and the cathode are cylindrical but not coaxial. We made a simplification on geometry and considered separately the cylindrical structure with vertical axis and the horizontal axis part lying on the floor. The vertical was considered as tripe coaxial structure with the outer connected to the middle one in one point. The model used was as a "Π" cell. Instead the horizontal was modeled with "T" cells. A simple 2D fem calculation was done, in order to calculate electrical parameters (as they cannot be made analytically due to the non-coaxiality of conductors). Tab. 3.8 summarizes the parameters of the tank electrical model of fig. 3.14 and fig. 3.15, where "C_hv_mi" are

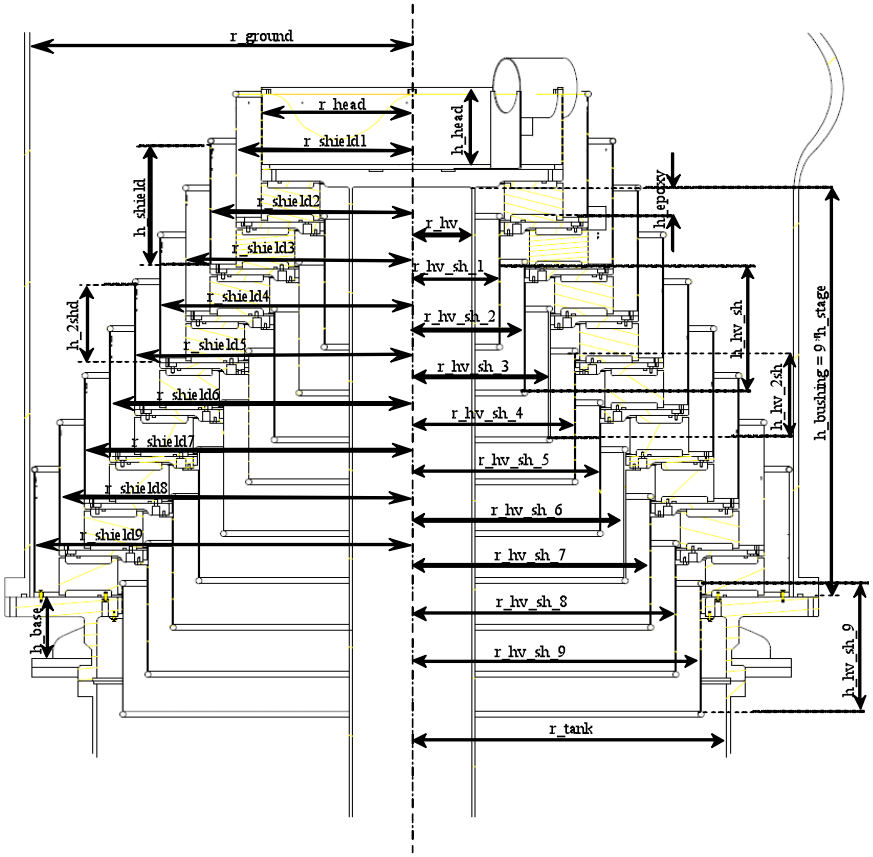

Figure 3.12: Section of the main bushing

Table 3.7: Electrical parameters for CEA bushing line model ($j = 1 \ldots 9$)

Name	Value	Name	Value	Name	Value
C_gr1	12 pF	Chv_st1	18 pF	C_stage_1	205 pF
C_gr12	22 pF	Chv_st2	54 pF	C_stage_2	291 pF
C_gr23	27 pF	Chv_st3	30 pF	C_stage_3	343 pF
C_gr34	33 pF	Chv_st4	23 pF	C_stage_4	391 pF
C_gr45	41 pF	Chv_st5	19 pF	C_stage_5	444 pF
C_gr56	53 pF	Chv_st6	16 pF	C_stage_6	504 pF
C_gr67	72 pF	Chv_st7	15 pF	C_stage_7	540 pF
C_gr78	110 pF	Chv_st8	13 pF	C_stage_8	600 pF
C_gr89	210 pF	Chv_st9	12 pF	C_stage_9	650 pF
		Chv_st10			
L_stage_j	43 nH	R_L_stage_j	11 $\mu\Omega$	R_C_stage_j	100 MΩ
L_stage_10	56 nH	R_L_stage_10	15 $\mu\Omega$		

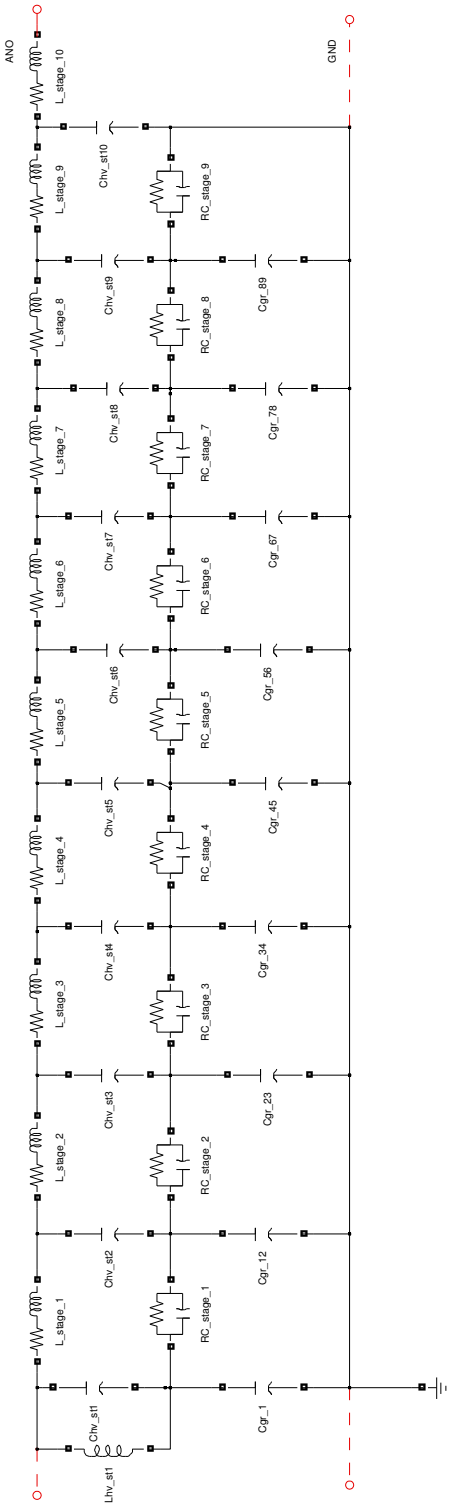

Figure 3.13: Bushing electrical model

the capacitances between the anode and the cathode, "C_m_lv$i$" between cathode and the tank and similarly for the inductances: "L_hv$j$" for the anode and "L_mj" for the cathode, both respect to ground tank. Instead values of resistances consider also the contribution of the external tank, added to the branches corresponding to anode and cathode.

Connections between cathode and external tank were modeled as low inductances (L_R_gnd$j$ = 50 nH) and small resistances (R_gnd$j$ = 10 $\mu\Omega$), like short-circuits. Then a short-circuit connection between the external tank and the inner cathode was added at the top of the vertical section to allow the current return mainly in the internal cathode. This was modeled as a small inductance L_short = 100 nH. We performed analyses with different connections between anode, cathode and tank in order to find the best solution for the experimental campaign (i.e. reduction of noise for the local ground reference conductor). Finally, a resistance corresponding to the damping resistor was inserted between the anode and the cathode. Three values were studied: 20, 40 and 60 Ω.

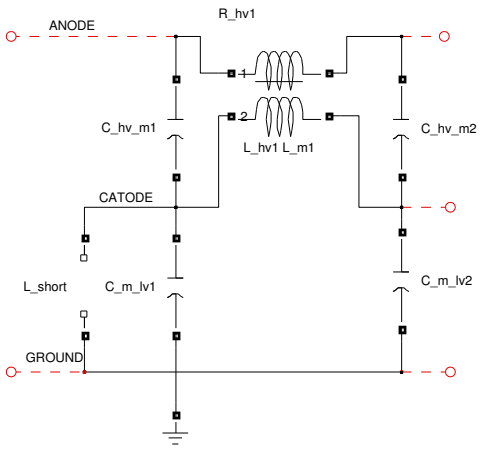

Figure 3.14: Vertical vacuum tank section electrical model

3.2.4 Results from short-circuit simulations

Joining the different sub-models together we started the short-circuit simulations. We performed different series to study the effect of damper. Short-circuit was modeled as an ideal switch, waiting for a proper circuital arc model. For each simulation we evaluated the main breakdown current, the voltage between anode and cathode, the potential of floating cathode to ground, the transient length, the voltage of the 9 bushing stages and the energy dissipated by the damper (values reported in tab. 3.4). A summary of the values calculated is reported in tab. 3.9. A sequence of plots for the 20 Ω damper case is presented: the breakdown current in fig. 3.16, the voltage between cathode and anode in fig. 3.17 and the voltage on the bushing stages in fig. 3.18.

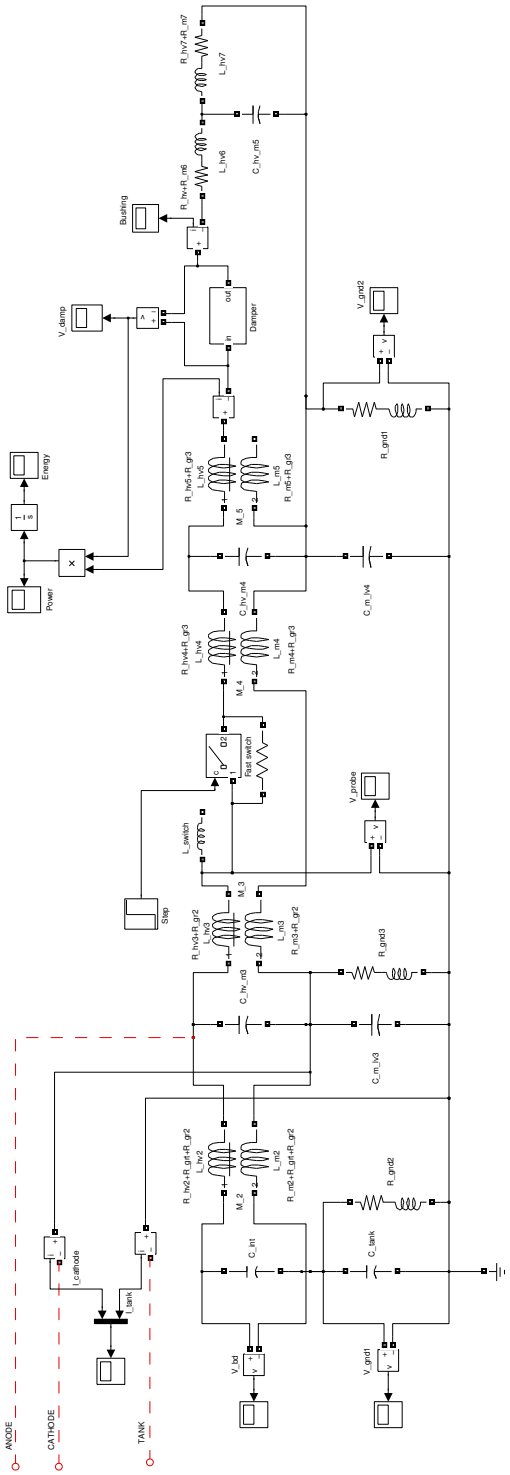

Figure 3.15: Horizontal vacuum tank section electrical model

Table 3.8: Electrical parameters for CEA vacuum tank model

Name	Value	Name	Value
L_hv1	973 nH	L_m1 = M_1	362 nH
C_hv_m1 = C_hv_m2	35 pF	C_m_lv1 = C_m_lv2	112 pF
C_int	3 pF	C_tank	19 pF
C_hv_m3	97 pF	C_m_lv3	273 pF
C_hv_m4	13 pF	C_m_lv4	65 pF
C_hv_m5	13 pF		
L_hv2 = L_hv3	362 nH	L_m2 = L_m3 = M_2 = M_3	150 nH
L_hv4 = L_hv5	169 nH	L_m4 = L_m5 = M_4 = M_5	36 nH
L_hv6 = L_hv7	135 nH		
R_hv1	186 $\mu\Omega$	R_m1	125 $\mu\Omega$
R_hv2 = R_hv3	135 $\mu\Omega$	R_m2 = R_m3	88 $\mu\Omega$
R_hv4 = R_hv5	39 $\mu\Omega$	R_m4 = R_m5	21 $\mu\Omega$
R_hv6 = R_hv7	39 $\mu\Omega$	R_m6 = R_m7	20 $\mu\Omega$
R_gr1	6 $\mu\Omega$	R_grt	8 $\mu\Omega$
R_gr2	10 $\mu\Omega$	R_gr3	3 $\mu\Omega$

Table 3.9: Summary of simulations on CEA testbed electrical model

Damping resistance [Ω]	Current peak [kA]	Voltage reversal [kV]	Cathode potential [V]	Transient time [μs]
0	35	900	2000	>500
20	22	250	1500	15
40	16	140	1100	10
60	12	80	800	5

We can point out some observations on the results. First of all, oscillation frequencies are in the order of some MHz, as expected. Then, the introduction of damper has a positive effect for all the quantities: current peak decreases from 30 to 60 % (depending on the resistance value), voltage reversal is limited from the full voltage value almost to zero while also the cathode potential is strongly reduced. So the damper seems to be very effective to limit the fast transient effects. An interesting observation can be done considering the energy dissipation on the damper itself, as it seems to be not dependent on the resistance value (see tab. 3.4): the higher the resistance, the higher is the breakdown current but lower the damper voltage drop. So these effects counterbalance.

Finally, another interesting result is the uneven voltage distribution on bushing stages both during the early fast transient and after its ending; in particular the first stage (near the transmission line) is more stressed while other stages are stressed with lower values but different polarities. This behaviour is quite anomalous and dangerous because it can lead to unexpected breakdowns on the first stages of bushing.

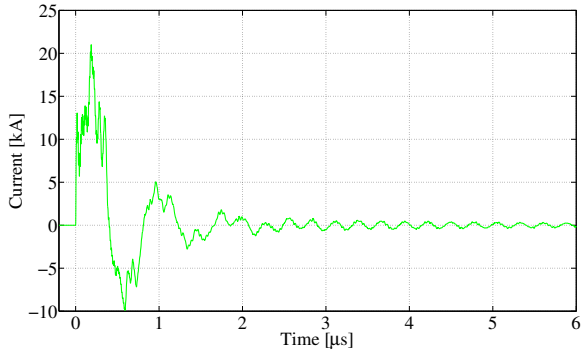

Figure 3.16: Breakdown current for the 20 Ω damper case

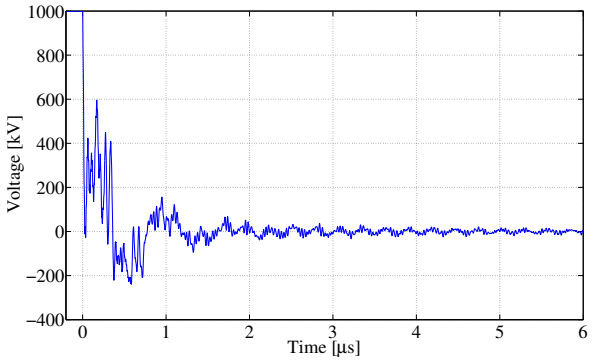

Figure 3.17: Voltage between cathode and anode for the 20 Ω damper case

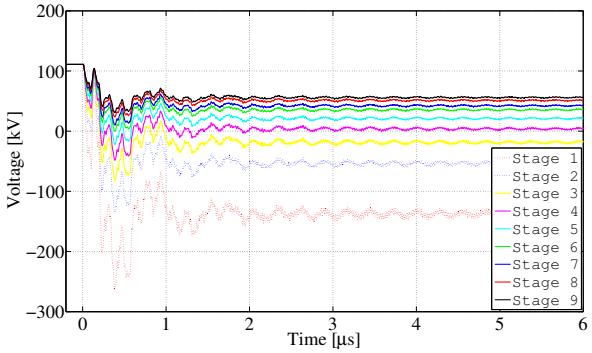

Figure 3.18: Voltage between bushing stages

3.2.5 Circuit validation

In order to validate the equivalent circuit, as the breakdown is not a known element, we need firstly to perform some tests using a fast triggered making-switch, instead of the gap breakdown. The plant can be insulated in air, since there are no changes in the value of impedances. To use such static switch the voltage needs to be lowered in the order of some tens kV. We provided a SCR solid-state switch built by Behlke® (model HTS 320-800-SCR, maximum voltage 32 kV and maximum current 8 kA). It was also provided by a diode in anti-parallel connection to allow re-circulating of reverse current in case of oscillations. We chose a value of 20 kV as maximum applicable, to have sufficient safety margin. The circuit was then updated with the value of impedance estimated for the switch (approximately 400 nH). Simulations were made on this circuit.

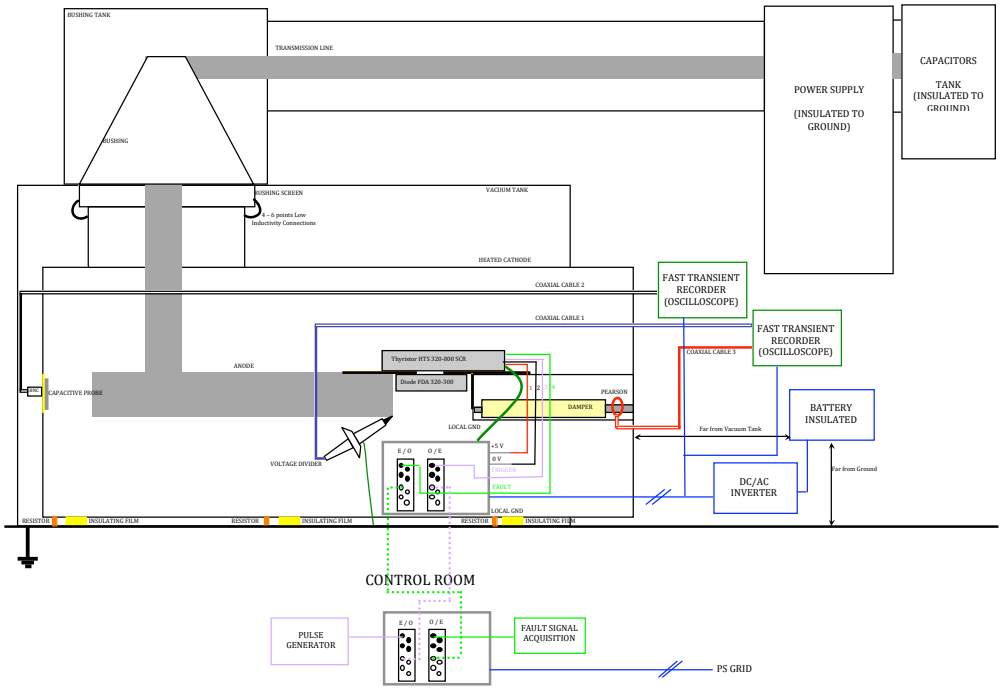

Figure 3.19: Scheme of electrical connections for the experimental tests

Fig. 3.19 shows the electrical connections of the circuit for the validation test phase. In particular we can see the three acquisition foreseen: a Pearson® current probe, a Tektronix® voltage probe and a fast transient capacitive probe. Last two signals need to be routed to different scopes, in order to avoid ground loops. Plots of the waveforms expected from the three acquisition devices in a a switch test with a 60 Ω damper are shown from fig. 3.20 to fig. 3.22. Voltage waveforms from the two voltage probes are substantially identical, so there is not a great effect of the different position of probe installation. Current is limited within 250 A. Obviously installing a different resistance damper the value would increase.

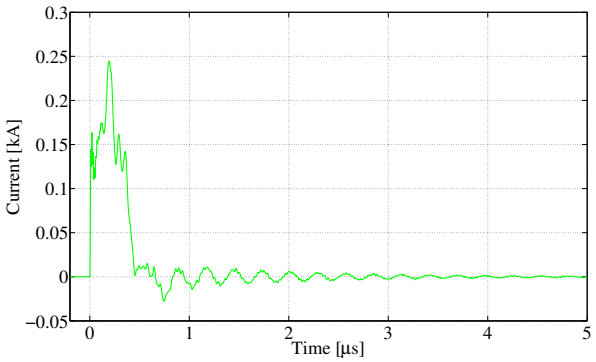

Figure 3.20: Current expected in low voltage test for circuit validation

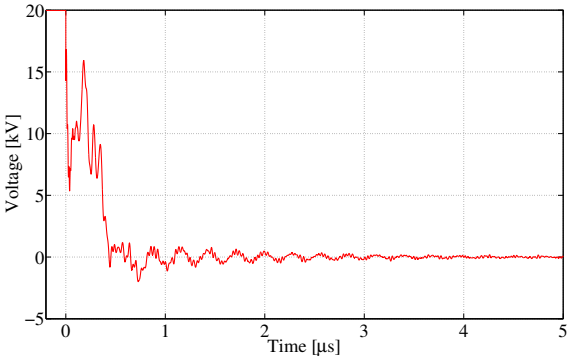

Figure 3.21: Voltage expected from high-voltage probe in low voltage test for circuit validation

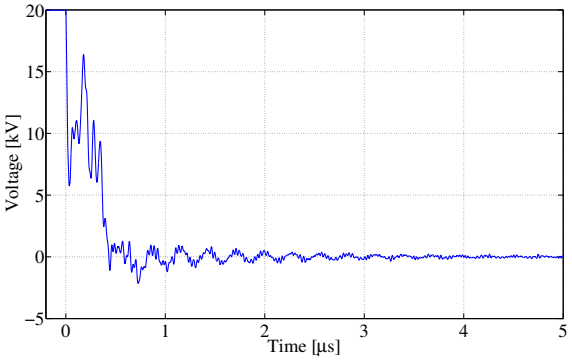

Figure 3.22: Voltage expected from capacitive probe in low voltage test for circuit validation

3.3 Distributed Core Snubber

3.3.1 Concept

Basically, the DCS concept derives from the observation that for the large NBI (i.e. those, having large electrostatic energy stored downstream the concentrated core snubber CCS, in the order of 1 nF) it is not possible to control the breakdown current peak, being determined only by the downstream stray capacitances and by the arc electrical parameters (inductivity and non linear resistance). As a consequence, the current limitation design input is not applicable. The oscillation damping capability becomes the design driver for the core snubber: as a matter of fact, appropriate damping reduces EMI and arc energy, provided the energy is proportional to the flowed absolute electric charge. In this sense the DCS, being an impedance ladder network, should have superior performances with respect to the CCS – a lumped impedance [30].

The structure of such DCS is quite simple. It consists of two cylinders coaxial to the inner high voltage central conductor (1 MV for the full voltage injector), shown in fig. 3.25: the inner made of ferromagnetic (insulated) material and the outer made of resistive material. Order of magnitude for parameters used to obtain sufficient damping is 1–10 μH/m and 1–10 Ω/m. This solution offers some advantages like simplicity – because it is not cumbersome so it can be easily integrated in the transmission line – and the un-necessity of pre-biasing of the core.

3.3.2 Integration on NBI

As a demonstration example of the concept a simple circuit was implemented, shown in fig. 3.23. We report a comparison between a concentrated core snubber CCS ($L = 1$ mH inductance in parallel to $R = 1$ kΩ resistance) with two DCS, one with the impedance split into five sections and the other split into 20, with $L_{DCS} = L_{CCS}/N$, $R_{DCS} = R_{CCS}/N$. These core snubbers protect against a breakdown from the energy stored in the capacitance of the 70 m transmission line (1 kJ at 1 MV, similar to the NBI case). The stored energy downstream the high voltage bushing is 400 J while the overall inductivity seen by the arc current is assumed to be 1 μH: this is a simple assumption with the order of magnitude of the values according to the circuit model presented in a recent work [26].

The model shows that the current peak is the same, whilst the oscillation is damped much more efficiently: arc extinguishes in less than 2 μs using DCS, lasting up to 10 μs using CCS; furthermore, it is interesting to observe that the damping effectiveness is almost equal for the two DCS solutions. In terms of magnetic flux (Φ, in VoltSecond), it results nearly evenly shared among the DCS sections ($\Phi_{CCS}/\Phi_{DCS-5} = 4.5$ and $\Phi_{CCS}/\Phi_{DCS-20} = 18$ for the DCS section closer to the accelerator).

The DCS solution has also the advantage to reduce the amplitude of the traveling waves in consequence of insulation failure of gas insulated components (transmission lines mainly and high voltage decks) [5], so avoiding the risk of multiple insulation faults. Fig. 3.24 shows the simulated case of a breakdown inside the transmission line, located at the high voltage power supply end. A DCS with $l = 1$ μ/m and a $r = 1$ Ω/m has been

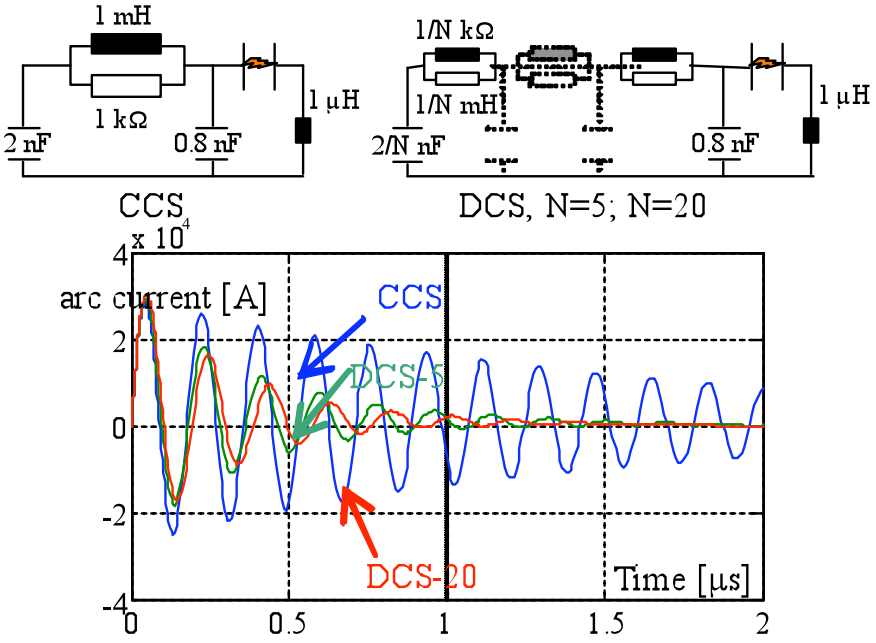

Figure 3.23: Arc current with CCS, $N = 5$ and $N = 20$ DCS

compared with the CCS having $L = 100$ μH and $R = 100$ Ω. The ability of the DCS to damp the voltage oscillation is evident, reducing also the voltage reversal (dangerous in the high voltage dc systems–HVDC) from 100 % to less than 50 %.

The DCS construction results much easier, being the ferromagnetic core much smaller and lighter. Furthermore, this allows the use of cores with lower permeability and hysteresis (solution not possible with the CCS, to keep the dimension acceptable), with the possibility to avoid the installation of the core resetting circuit. The smaller core also allows the use of more "smart" solution for the resistor, which can be realized in coaxial shape, as sketched in fig. 3.25. Using the gapped-core technology (e.g., having $\mu_r = 240$ at 1 MHz, $B_{sat} = 1.56$ T and $B_{res} \sim 0$, with a core thickness of 20 mm, resistor thickness 15 mm and inner conductor diameter 400 mm) 5 μH/m at 1 MHz and 1 Ω/m can be achieved.

3.3.3 Experimental validation campaign

A campaign over a small-scale transmission line with a DCS was made to study the effects of the core snubber when subjected to a fast transient [30]. A short coaxial line short-circuited at one end was realized. The design of DCS was based on properties of these two materials (magnetic and resistive):

- Amorphous alloy 2605SA1 ribbon, employed to build the Microlite® HF distributed gap cores (by Metglas®);

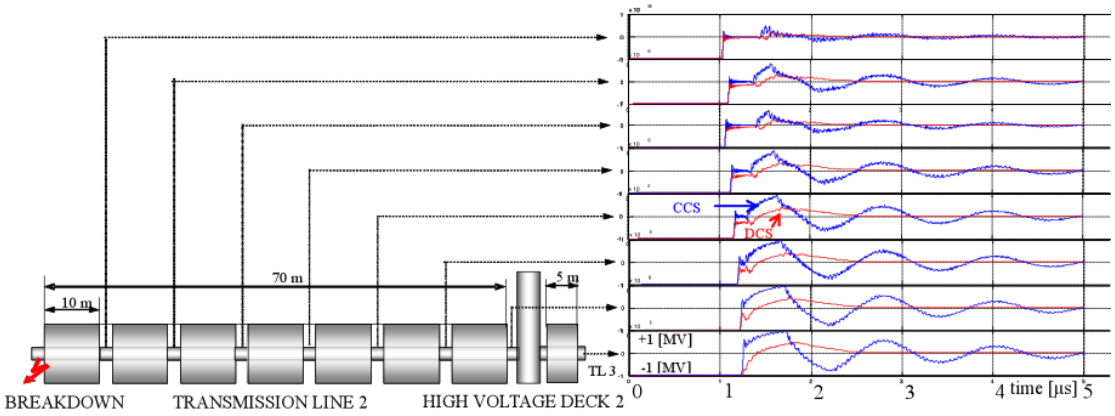

Figure 3.24: Voltage propagation inside the transmission line comparing the effects of CCS and DCS

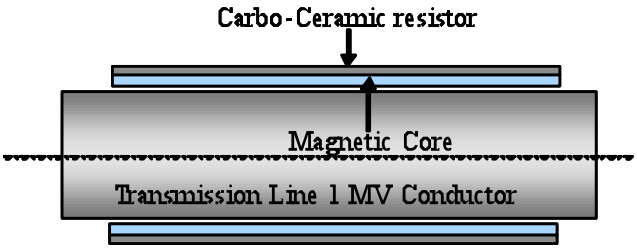

Figure 3.25: Sketch of full coaxial DCS

- Clay-alumina-carbon mixture, used to produce carbo-ceramic resistors (by HVR International Ltd.®).

The two cylinders constituting the coaxial line and the short-circuitiing ring were realized by stainless steel AISI 304 (whose resistivity is $\rho_{SS} = 720$ nΩ/m). The core snubber was made with coaxial stacks of 13 toroidal cores and 6 carboceramic disks, centred inside the line around the inner conductor. Carboceramic disks used were of two types, matching with two different resistance values (2.2 Ω/disk or 10 Ω/disk). An outline of the experimental setup is shown in fig. 3.26. Parameters of the elements were derived from material data-sheet, but a measurement was done anyway. The following list summarizes element properties:

- Metglas toroidal core MP7548MDCG
  - Nominal permeability: $\mu_r = 245$
  - Saturation flux density: $B_{sat} = 1.56$ T
  - Inductance per turn: $L_{turm} = 177$ nH/N^2
  - External diameter: $D_e = 30$ mm
  - Internal diameter: $D_i = 20.5$ mm
  - Width: $H = 10$ mm
  - Weight: $P = 0.028$ kg
  - Curie temperature: $T_{Curie} = 395$°C
- HVR resistors M004B — AB403
  - Nominal resistance: 2.2 $\Omega \pm 20\,\%$ and 10 $\Omega \pm 10\,\%$
  - External diameter: $D_e = 112$ mm
  - Internal diameter: $D_i = 34$ mm
  - Width: $L = 25.4$ mm
  - Weight: $P = 0.515$ kg
  - Dielectric permittivity: $\varepsilon_r = 5$
  - Electrical resistivity: $\rho_{2.2} = 0.77$ Ωm and $\rho_{10} = 3.52$ Ωm

Core snubber assembly, without outer conductor, is shown in fig. 3.27. Magnetic toroidal cores are epoxy insulated, so useful magnetic dimensions were a bit lower than nominal (in particular width $H = 9.525$ mm). The snubber stack was pressed by a threaded steel rod, tightened at both ends by nuts over two insulating plates. Dimensions of the final assembly were the following (see fig. 3.28):

- Total length: $d = 500$ mm
- Core snubber length: $d_s = 153$ mm

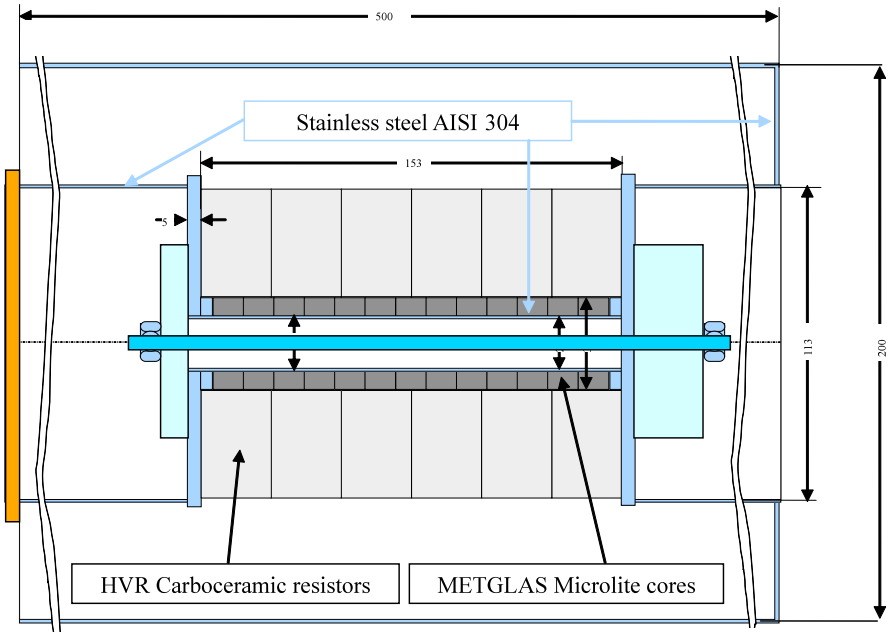

Figure 3.26: Quoted model of the experimental set-up

- External length: $d_c = 168.5$ mm
- Effective iron length: $d_{Fe} = 13$ x $9.525 \approx 124$ mm
- Internal conductor radius: $a_i = 10$ mm
- External magnetic cores radius: $a_{Fe} = 15$ mm
- External resistors and middle conductor radius: $a_c = 56$ mm
- External conductor radius: $a_e = 100$ mm
- Internal conductor thickness: $s_i = 0.5$ mm
- Middle conductor thickness: $s_c = 1$ mm
- External conductor thickness: $s_e = 2$ mm

3.3.3.1 Magnetic cores properties

The data-sheet of the Metglas Microlite material provides magnetic permeability dependence on frequency only up to 1 MHz (see fig. 3.29). For our experiment voltage rise-time was in the order of some hundreds ns so we needed to extend permeability dependence upon frequency at least until 10 MHz.

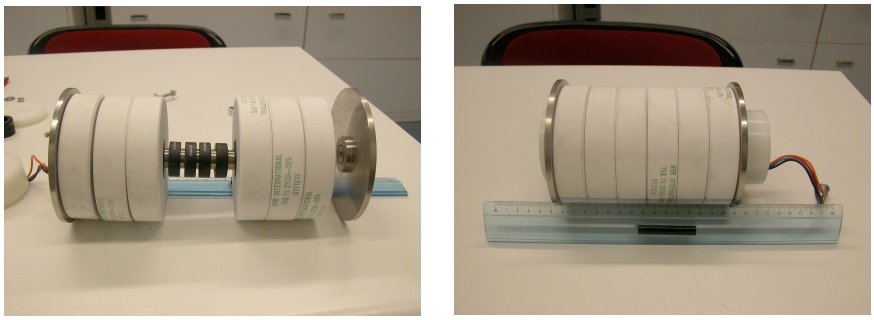

(a) Open stack (b) Closed ctack

Figure 3.27: Core snubber assembly

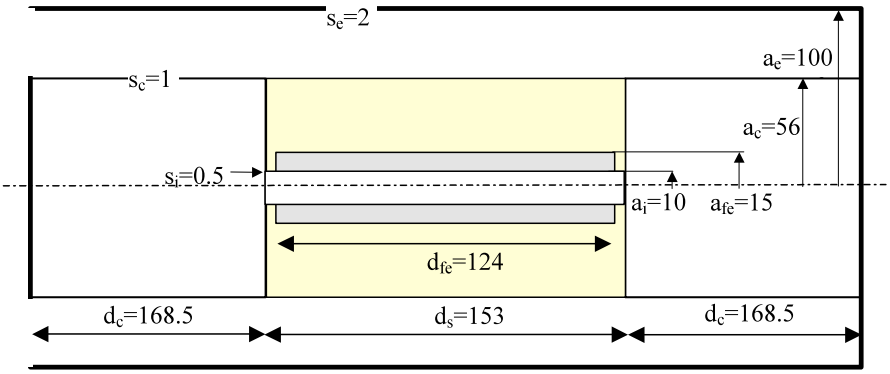

Figure 3.28: Schematic assembly with dimensions

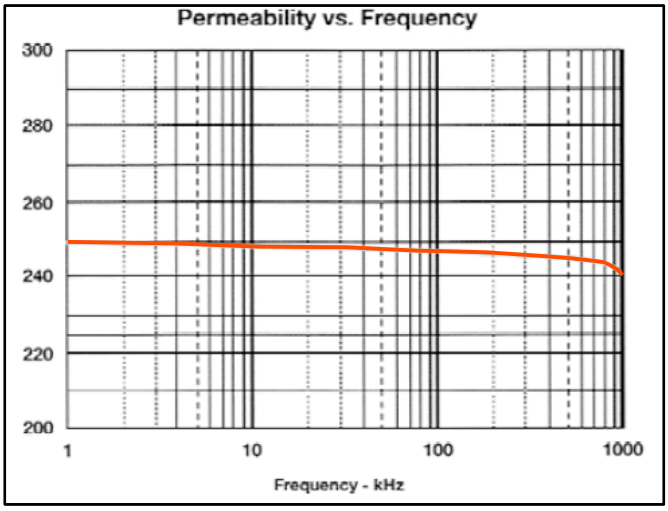

Figure 3.29: Microlite permeability vs. frequency (by Metglas®)

A core was wrapped with 58 turns of copper wire; then we realized an impedance measurement between frequencies of 10 kHz and 100 MHz, using an impedance/gain-phase analyzer HP 4194A. This instrument was used also to obtain the parameters of the equivalent circuit RLC, i.e. the parallel between a RL series branch and a C branch. Capacity was that between turns while resistance included resistive losses (on copper) and iron losses (on magnetic core). For each frequency the impedance analyzer gave two values (impedance and phase), and then calculated parameters of the equivalent circuit which best fit with measures. The parameters calculated at lowest frequency (with still no variation of permeability) are:

- $R = 4.3\ \Omega$
- $C = 12.34$ pF
- $L = 550\ \mu$H

We assume the only parameter not changing with frequency is the capacity C. Then we can see in fig. 3.30 and fig. 3.31 some resonances over 10 MHz, not having reference to the equivalent circuit. So we chose to use this model with sufficient reliability only up to 10 MHz.

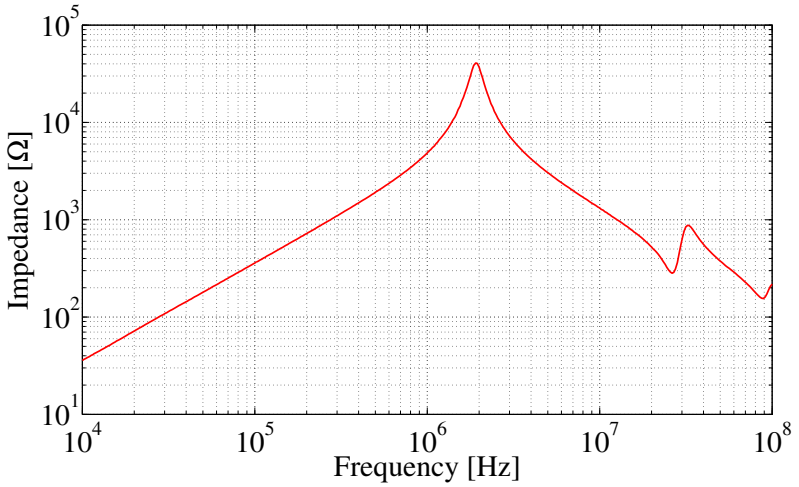

Figure 3.30: Measured impedance of magnetic core

The procedure for permeability calculation is the following. For each frequency we took from the impedance analyzer the values of impedance and phase, then we wrote the system of two equations in two unknown quantities (resistance R and inductance L). We fixed the capacitance $C = 12.34$ pF on the previous value given by the equivalent circuit

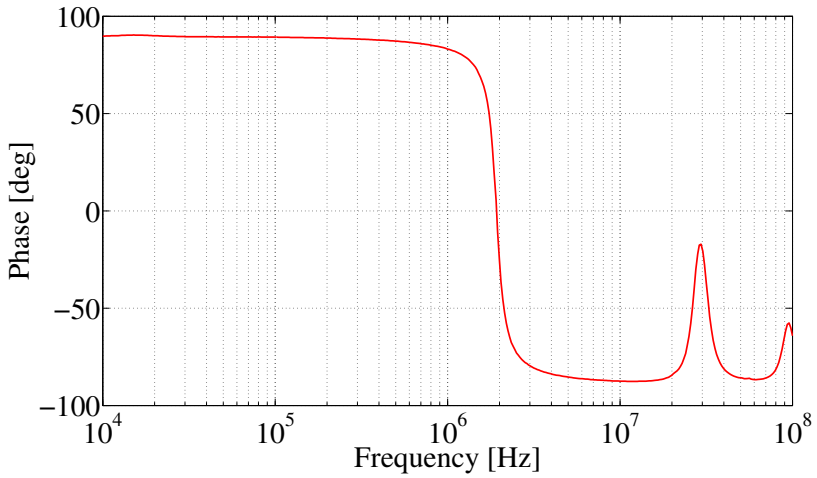

Figure 3.31: Measured phase of magnetic core

of impedance analyzer at low frequency. The following equation of the circuit

$$\dot{Z} = \frac{(R + j\omega L) \cdot \left(\frac{-j}{\omega C}\right)}{R + j\left(\omega L - \frac{1}{\omega C}\right)} \tag{3.1}$$

can be separated into a system of two equations, one for modulus, the other for phase:

$$\begin{cases} Z^2 = |\dot{Z}|^2 = \dfrac{\omega^2 L^2 + R^2}{\omega^2 C^2 R^2 + (\omega^2 LC - 1)^2} \\ \tan\varphi = \angle Z = \dfrac{-\omega^3 L^2 C - \omega C R^2 + \omega L}{R} \end{cases} \tag{3.2}$$

Finally, we rewrote the system considering the two unknown quantities R and L, as stated before:

$$\begin{cases} \omega^3 C L^2 - \omega L + \omega C R^2 + \tan\varphi \cdot R = 0 \\ (\omega^2 - \omega^4 C^2 Z^2) \cdot L^2 + 2\omega^2 C L Z^2 + (1 - \omega^2 C^2 Z^2) \cdot R^2 - Z^2 = 0 \end{cases} \tag{3.3}$$

Solving system for each frequency we obtained two vectors, one with values of equivalent resistance and the other of inductance. For each value of inductance we calculated the corresponding value of relative magnetic permeability, through the equation:

$$L = N^2 \cdot L_{one\,turn} \cdot \frac{\mu_r}{\mu_{r\,nom}} \Rightarrow \mu_r = \frac{L}{N^2 \cdot L_{one\,turn}} \cdot \mu_{r\,nom} \tag{3.4}$$

where $N = 58$ turns, $L_{one\,turn} = 177$ nH (nominal value), $\mu_{r\,nom} = 245$. We used Matlab® code to solve eq. 3.3, then we calculated permeability according to 3.4 and

plotted results. As already reported, we didn't calculate the solution beyond 10 MHz, as some convergence problems also arose. Final results are shown in fig. 3.32: there is a great decrease of permeability beyond 1 MHz. At 5 MHz this value turns from nominal value 245 to 180, falling down to 100 at 10 MHz.

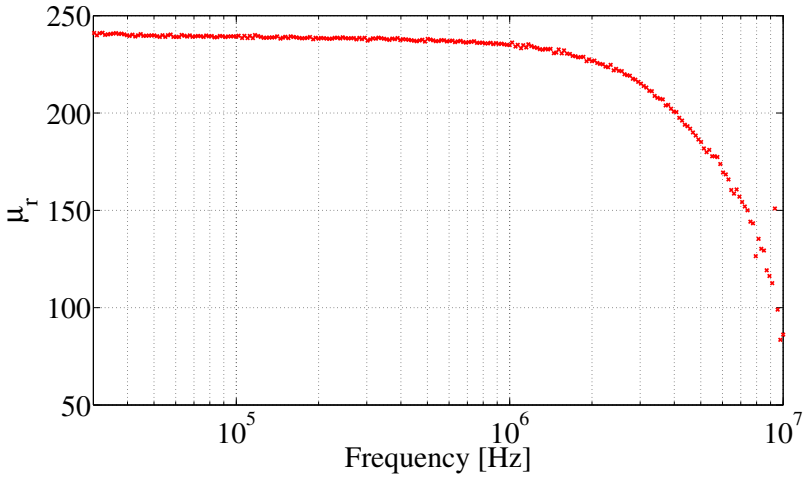

Figure 3.32: Calculated Microlite® magnetic core permeability

We evaluated then the saturation flux value for the magnetic cores, an important parameter for the DCS effectiveness. The minimum value corresponds to the flux bringing into saturation the inner part of magnetic core, while the maximum value corresponds to the flux bringing into saturation the whole core.

$$\Phi_{sat-min} = \int v_p \, \mathrm{d}t = B_{sat} \cdot \ln\left(\frac{a_{Fe}}{a_i}\right) \cdot a_i \cdot d_{Fe} = 780 \ \mu\mathrm{Wb} \tag{3.5}$$

$$\Phi_{sat-max} = \int v_p \, \mathrm{d}t = B_{sat} \cdot (a_{Fe} - a_i) \cdot d_{Fe} = 960 \ \mu\mathrm{Wb} \tag{3.6}$$

3.3.3.2 Circuit model

An equivalent model, taking into account also parasitic parameters of physical model, was implemented. Geometric values and material properties were considered. Starting from the equations of mutual coupled circuits (where primary circuit is the inner conductor and secondary the carboceramic resistors with common current return, namely the external conductor) we consider the two currents I_L and I_R and the magnetic flux Φ_L and Φ_R. So we write the system:

$$\begin{aligned} \Phi_L &= L_L I_L + M I_R \\ \Phi_R &= M I_L + L_R I_R \end{aligned} \tag{3.7}$$

The mutual inductance M between the two circuits is equal to the auto-inductance

L_R of the secondary circuit, so we obtain:

$$\Phi_L - \Phi_R = (L_L - M)I_L \tag{3.8}$$

Then we write the equations system for voltage of each circuit (where v_{ext} includes the common inductive voltage drop before and after the snubber and the resistive voltage drop on the external conductor):

$$\begin{aligned} v_L - v_{ext} &= \frac{\mathrm{d}\Phi_L}{\mathrm{d}t} + R_L i_L \\ v_R - v_{ext} &= \frac{\mathrm{d}\Phi_R}{\mathrm{d}t} + R_R i_R \end{aligned} \tag{3.9}$$

Naturally also v_L and v_R are equal so we obtain:

$$\frac{\mathrm{d}\Phi_L}{\mathrm{d}t} + R_L i_L = \frac{\mathrm{d}\Phi_R}{\mathrm{d}t} + R_R i_R \tag{3.10}$$

Rearranging:

$$\frac{\mathrm{d}(\Phi_L - \Phi_R)}{\mathrm{d}t} = R_R i_R - R_L i_L \tag{3.11}$$

So calculating derivative of eq. 3.8, equalizing with eq. 3.11 and rearranging:

$$(L_L - M)\frac{\mathrm{d}i_L}{\mathrm{d}t} + R_L i_L = R_R i_R \tag{3.12}$$

This result shows that the core snubber can be modeled as a parallel of two elements: a resistance R_R, which represents the carboceramic resistors, and a series of a resistance R_L, representing the inner conductor resistance, and an auto-inductance $L_L - M$; this accounts only for the effect of magnetic core, without the mutual inductance of air and of massive resistors. The scheme is reproduced in fig. 3.33.

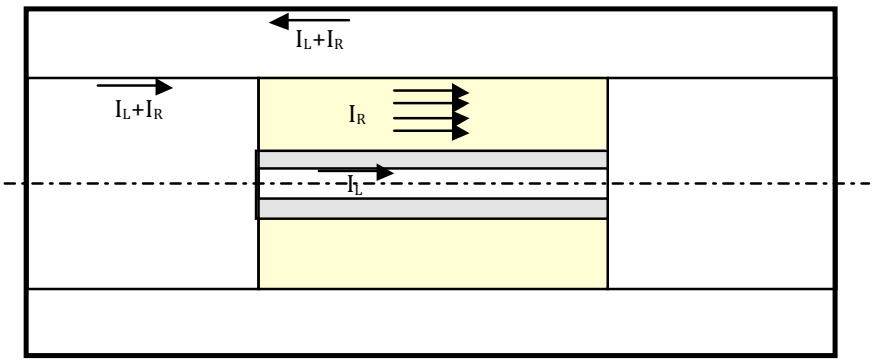

Figure 3.33: Scheme of the two mutual coupled circuits

So applying geometry the following parameters summarize the electrical model of fig. 3.34:

- $C = \dfrac{2\pi\varepsilon_0}{\ln\left(\dfrac{a_e}{a_c}\right)} \cdot d_c = 16.2$ pF

- $L = \dfrac{\mu_0}{2\pi} \ln\left(\dfrac{a_e}{a_c}\right) \cdot d_c = 19.5$ nH
- $R = \rho_a \cdot d_c \cdot \left[\dfrac{k_c(f)}{2\pi a_c \cdot s_c} + \dfrac{k_e(f)}{2\pi a_e \cdot s_e}\right] = 474\ \mu\Omega$ at $f = 0$
- $L_P = L_L - M = \dfrac{\mu(f)}{2\pi} \ln\left(\dfrac{a_{Fe}}{a_i}\right) \cdot d_{Fe} = 2.5\ \mu$H at $f = 0$
- $R_P = R_R = 13.2\ \Omega$ — $60\ \Omega$
- $R_L = \rho_a \cdot d_s \cdot \dfrac{k_i(f)}{2\pi a_i \cdot s_i} = 3.5\ \text{m}\Omega$ at $f = 0$
- $L_S = M = \dfrac{\mu_0}{2\pi}\left[\dfrac{1}{2} - \dfrac{a_{Fe}^2}{a_c^2 - a_{Fe}^2} \cdot \ln\left(\dfrac{a_c}{a_{Fe}}\right) + \ln\left(\dfrac{a_e}{a_c}\right)\right] \cdot d_s = 30$ nH
- $R_S = \rho_a \cdot d_s \dfrac{k_e(f)}{2\pi a_e \cdot s_e} = 117\ \mu\Omega$ at $f = 0$
- $C_R = \dfrac{2\pi\varepsilon_0 \cdot \varepsilon_r}{\ln\left(\dfrac{a_c}{a_{Fe}}\right)} \cdot d_s = 32.2$ pF
- $G = \dfrac{2\pi}{\rho \cdot \ln\left(\dfrac{a_c}{a_{Fe}}\right)} \cdot d_s = 0.94$ S — 0.21 S
- $C_a = \dfrac{2\pi\varepsilon_0}{\ln\left(\dfrac{a_e}{a_c}\right)} \cdot d_s = 14.6$ nF

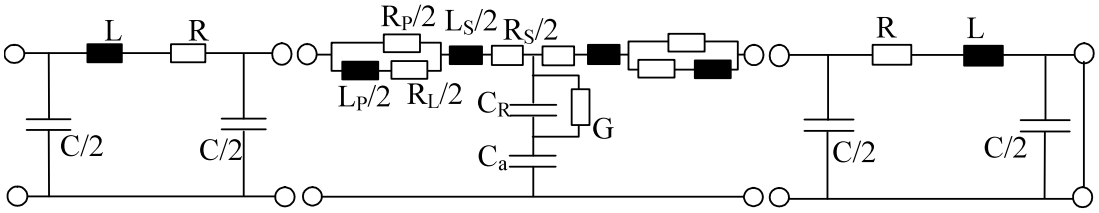

Figure 3.34: Equivalent electrical model for the DCS mock-up

The resistance are evaluated in dc conditions (that is with k_e, k_i, $k_c = 1$); "Π" cells (with C, R and L) at both ends account for parameters of coaxial line outside the inner conductor with snubber. Shunt branch in the middle "T" cell includes capacitance C_R of carboceramic resistors (coaxial capacitor), in parallel to its conductance G, and capacitance C_a of air between the external conductor and the external part of resistors. Snubber parameters are the inductance L_P (in series to the inner conductor resistance

R_L) in parallel to the resistance R_P of carboceramic resistors. R_S is the resistance of the outer return conductor. Finally, L_S takes into account both the inductances in air and of the resistors, considered as a massive conductor with uniform distribution of current.

3.3.3.3 Frequency response

The frequency response of the coaxial line – i.e. the impedance calculation – in a range of frequency between 10 kHz and 10 MHz was performed. We utilized the impedance analyzer to calculate and validate the equivalent circuit of fig. 3.34. For each frequency the values of resistances were corrected through the coefficients accounting for skin effect. First, we calculated the skin depth δ and thereafter the coefficient k_j, where j indicates each conductor (external, internal, central).

$$\delta = \sqrt{\frac{1}{\pi f \mu \gamma}} \tag{3.13}$$

$$k_j = \frac{R_\delta}{R_0} = \frac{s_j}{\delta} \text{ with } j = e,\, i,\, c \tag{3.14}$$

Of course, snubber inductance was corrected at each frequency with the value of measured permeability (fig. 3.32). Due to poor convergence in calculation, the comparison was limited to 8 MHz.

We made two series of measurement: the first with carboceramic ring resistance equal to 10 Ω (total resistance 60 Ω) and the second with 2.2 Ω (total resistance 13.2 Ω). The second case was chosen then for the following time domain tests. The software used for calculation was PowerSystem toolbox of Matlab Simulink®. Comparison between calculated and measured waveforms of modulus and phase for 60 Ω resistance coaxial line are shown in fig. 3.35 and fig. 3.36, while for 13.2 Ω are showin in fig. 3.37 and fig. 3.38.

We can point out there is a good agreement between measured and calculated modulus for snubber with total resistance 60 Ω, while phase fits within 15°. Instead using 13.2 Ω total resistance the calculation shows worse agreement for modulus and better agreement for phase. This behaviour was not well understood; in any case the agreement between measurement and model was considered enough satisfactory to characterize the impedance frequency response.

3.3.3.4 Time domain tests

The final step was the characterization of the core snubber behaviour under fast discharge operation. This was obtained by the discharge of a capacitor, pre-charged at a certain voltage level, on the coaxial line using a gas spark-gap. The capacitor was brought at different initial voltage level. A scheme of the experimental setup is shown in fig. 3.39.

For each test we made two measurements, one of voltage with a Tektronix® high voltage probe HP DPO 6015 A, with a bandwidth of 100 MHz and a scale factor 1:1000, and one of current with a Pearson® current monitor 301X, with a bandwidth of 2 MHz

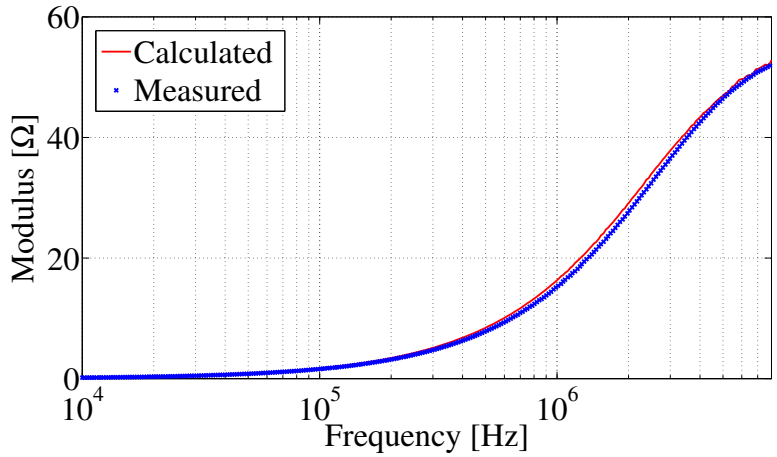

Figure 3.35: Modulus comparison between measured and calculated impedance with $R_s = 60\ \Omega$

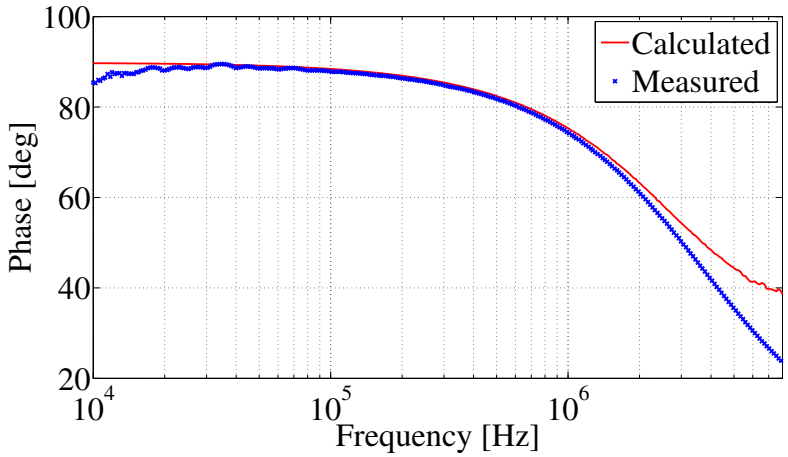

Figure 3.36: Phase comparison between measured and calculated impedance with $R_s = 60\ \Omega$

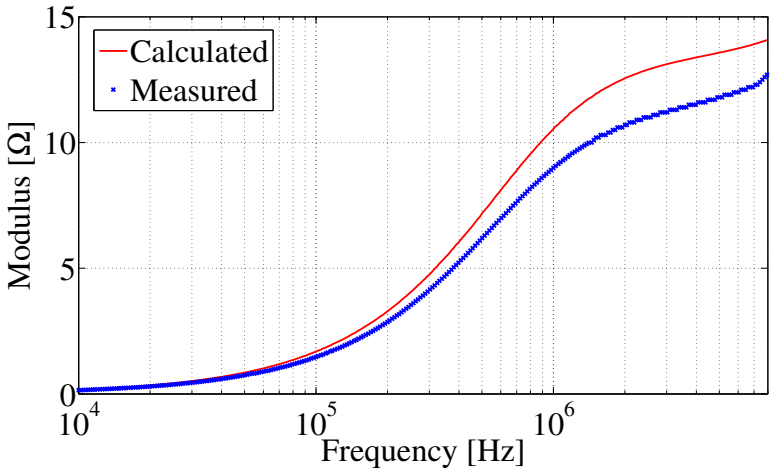

Figure 3.37: Modulus comparison between measured and calculated impedance with $R_s = 13.2\ \Omega$

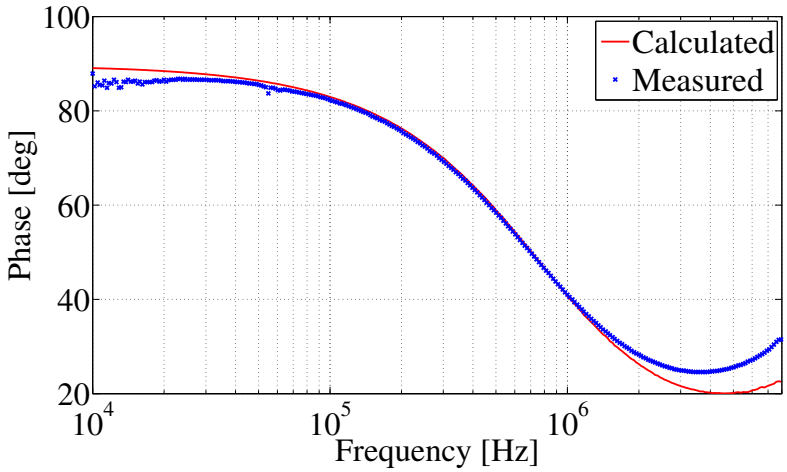

Figure 3.38: Phase comparison between measured and calculated impedance with $R_s = 13.2\ \Omega$

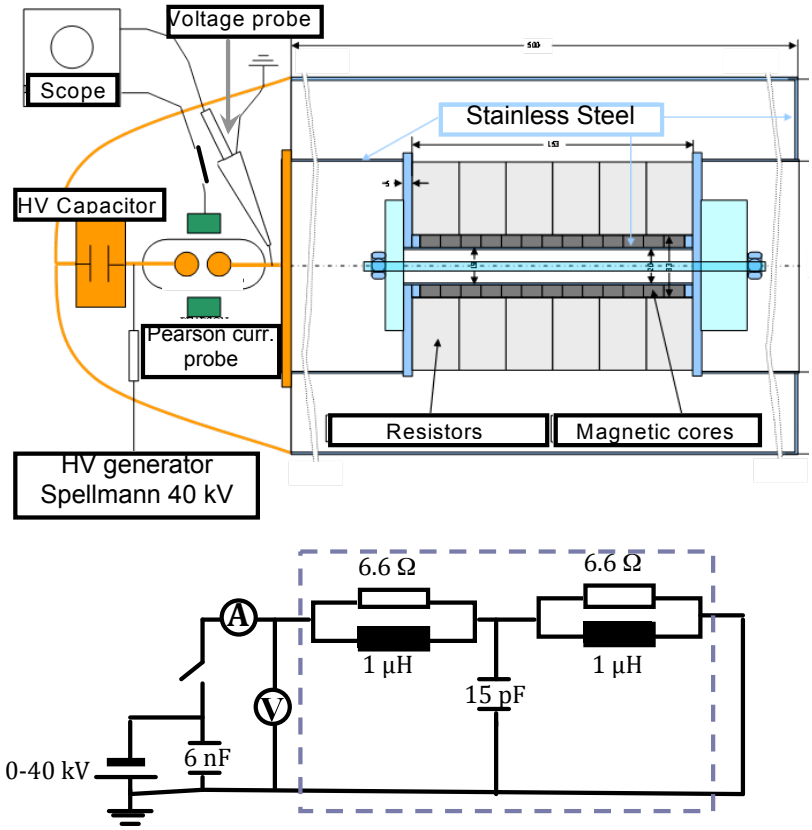

Figure 3.39: Scheme of measurement assembly for pulse tests and related equivalent circuit

and requiring an input rise time greater than 200 ns. Both measurement instruments were connected to a Tektronik® scope HP DPO 7054, with a bandwidth of 500 MHz to acquire signals. The picture in fig. 3.40 shows the assembly ready for pulse tests. To reduce the external connection inductance the closure circuit was done in such "dome" shape.

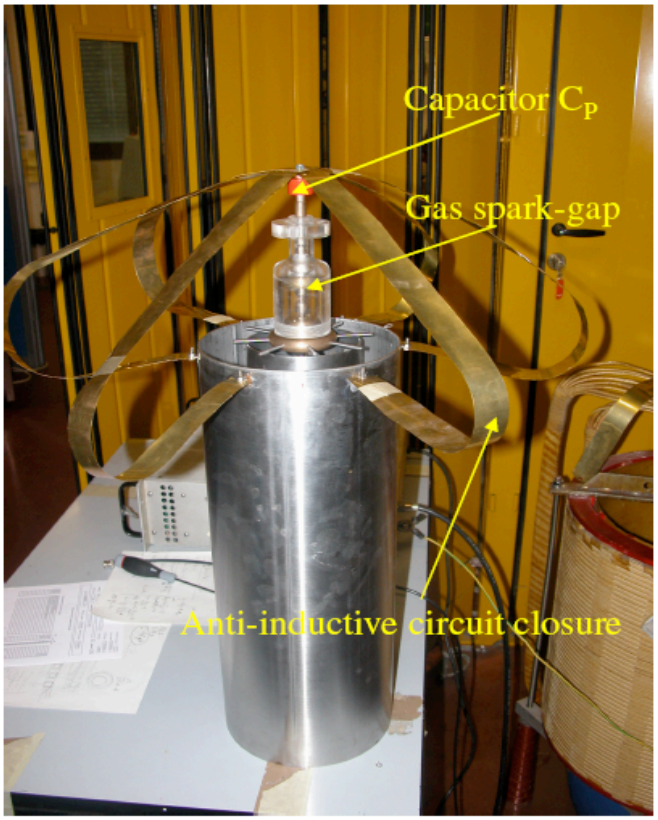

Figure 3.40: Picture of the assembly for pulse tests

The choice of capacitance value for the capacitor was done according to the following argument. As our aim is to detect the saturation condition limit, the best way to inspect the transition from linear to non-linear behaviour, caused by saturation, is to start from a strongly damped circuit, with a damping factor greater than 0.75. In this way, when the system reaches and overcomes saturation limit, as inductance decreases also damping factor decreases: so voltage starts to oscillate. The damping factor is obtained considering the simplified circuit, i.e. an $R-L$ parallel with in series the capacitance C pre-charged, ignoring the parasitic parameters:

$$\xi = \frac{1}{2}\frac{1}{R_P}\sqrt{\frac{L_P}{C_P}} > 0.75 \tag{3.15}$$

Rearranging and substituting known parameters R_P and L_P in the eq. 3.15 we calculated the maximum capacitance value for the capacitor, i.e. 6 nF. We chose then a configuration

using capacitors off-the-shelf: a parallel of 5 capacitors with a total equivalent capacitance 6 nF.

In parallel, simulations were carried out to help the results interpretation. Unfortunately it was not possible to implement a circuit with non-linear frequency-dependant parameters in time domain. So we decided to fix a value for the snubber inductance (so for magnetic permeability) and for conductor resistances (so for skin effect coefficients). We chose the values of the parameters correspondent to 5 MHz frequency, according to first tests, observing voltage rise time. Coefficients then became:

- $\mu_r = 180$
- $k_i = 2.6$
- $k_c = 5.2$
- $k_e = 7.8$

In this way, it's likely that in the first instants calculated voltage is closer to real one (because highest frequencies are acting) while after some fractions of μs there will be more difference because of larger inductance estimation (due to slower time dynamic).

From first experiences we realized soon a good agreement between measured and calculated waveforms for voltage; instead current measures were not accurate because of limited dynamic current probe properties. As a matter of fact, Pearson probe requires a rise time greater than 200 ns, while the experiment has a value lower than this specification. So current measure was disregarded.

Tests in linear behaviour We started a series of pulses starting from different capacitor voltage levels. We applied 6 kV and then 12 kV. Waveforms of calculated and measured voltages (in per unit) are plotted together in fig. 3.41.

We can point out that at the beginning there is a high-frequency oscillation: this is due to parasitic parameters of circuit and connections. However, it extinguishes quickly. There is no remarkable difference between the two measured voltages (in p.u.): it is an indicator of linearity for the system up to these voltage levels.

We calculated then the voltage integral for each set (corresponding to the flux swing on magnetic core), in order to compare the maximum value of flux with the theoretical saturation flux (eq. 3.5). Flux comparison is plotted in fig. 3.42. To calculate voltage integral we applied to the circuital model the measured voltage (fig. 3.41) and then calculated the effective voltage on the core snubber without the external voltage drop (on connections, on external air parts and on inductance in series to the capacitor). We calculated the voltage integral for this resulting waveform.

The most striking result is that slightly beyond 80 % of theoretical minimum saturation flux (i.e. 0.78 mWb) the system remains almost linear and voltage waveform is not affected by saturation effects of the core. Furthermore, it is clear that the system works as stated, because it is damped without any oscillation for all three cases.

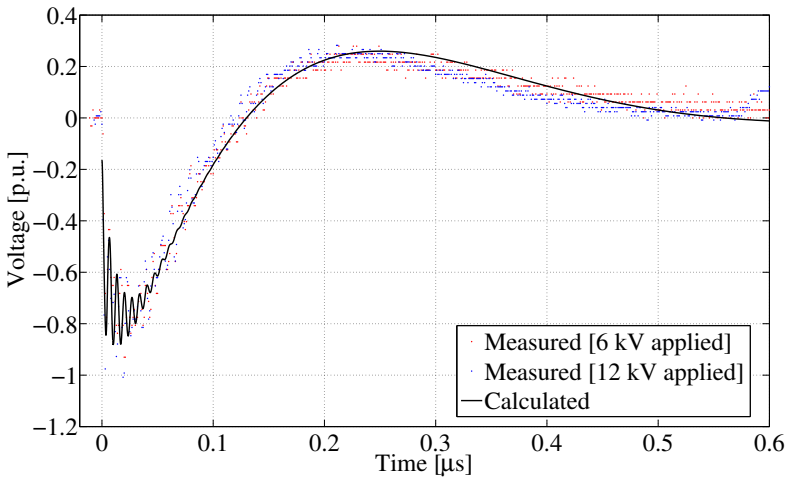

Figure 3.41: Measured and calculated voltages for a 6 nF discharge in linear condition

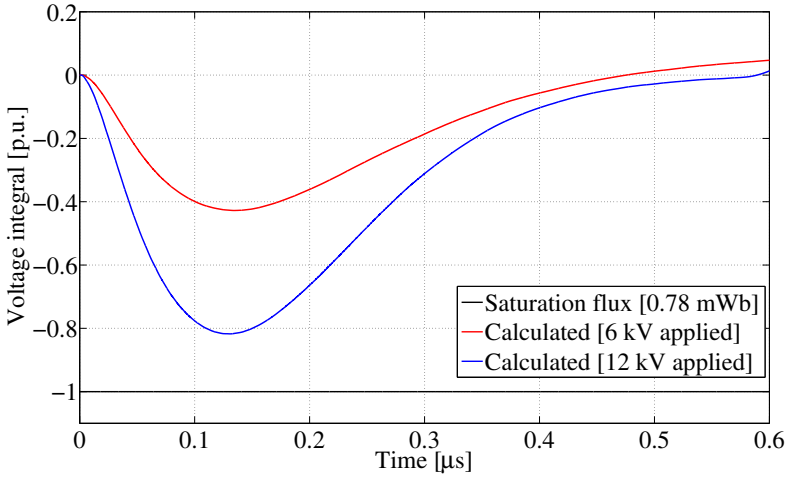

Figure 3.42: Voltage integral compared to saturation flux value for a 6 nF discharge in linear condition

Tests in saturation zone Further tests to inspect saturation limit were made. As already explained in the previous we looked for the transition from linear to saturation condition with the occurrence of an oscillation, due to reduction of inductance and consequently of the damping factor. We increased the level of applied voltage to obtain flux overcoming theoretical limit. When this happened, a different voltage shape appeared: it reached a peak with higher derivative and then started to oscillate. The behaviour is explained in fig. 3.43, where the measured voltage is compared to the calculated waveform in linear condition. When voltage integral gets out of saturation area voltage slowly starts to decrease and to damp. It must be pointed out that this behaviour occurs for predicted values of flux. Fig. 3.44 highlights this explanation.

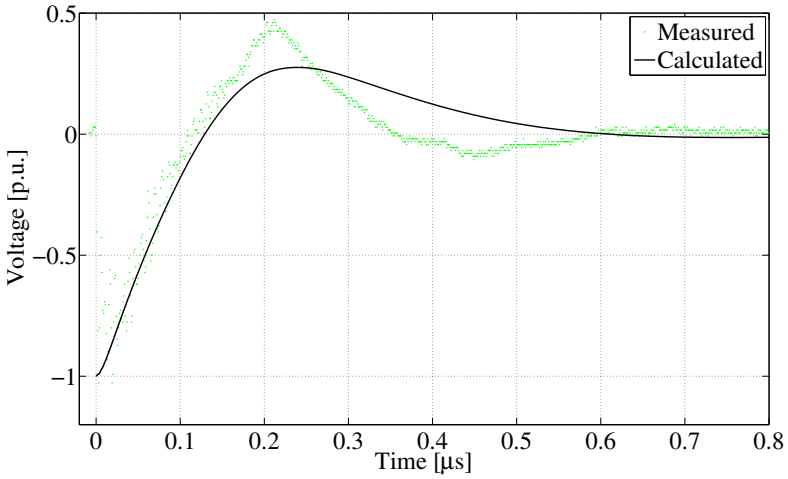

Figure 3.43: Measured and calculated voltages for a 6 nF discharge in saturation condition

Finally we did several tests to verify possible polarization effects and we found no changes between the recorded sessions: no appreciable polarization effects are present, as we expected from data-sheet specifications.

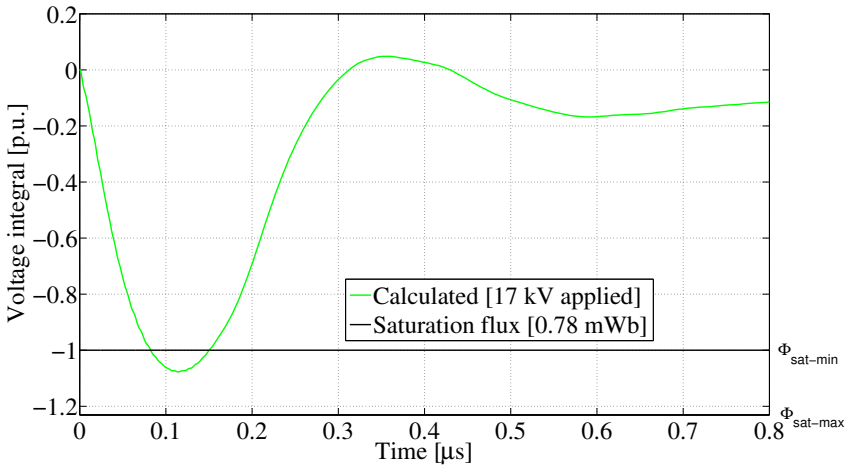

Figure 3.44: Voltage integral compared to saturation flux value for a 6 nF discharge in saturation condition

4

A comprehensive design: the SPIDER case

As for the other neutral beam experiments, a crucial problem for the SPIDER experiment is the reduction of the effects due to the breakdowns. The system is rated for an acceleration voltage of -100 kV (between extraction and grounded grid); the extraction voltage is -12 kV (between source and extraction grid) [6]. Maximum beam current is 63 A. A conceptual scheme of the power supply circuit together with the vessel and the equivalent electrical model is reported in fig. 4.1 and fig. 4.2.

4.1 Arc effect limitation strategy

The AGPS of the system has double insulation: the cold electrode (green in fig. 4.1) is insulated from the local ground (blue) and is connected to an inner screen IS (green). The inner screen is equipped in parallel with a low-resistance wire, carrying the dc current flowing into the vessel (where the current is measured). To allow the vessel current measurement the inner screen is also connected to the source tank by a screen resistor array (RS).

In case of a breakdown between the grids the first aim is the reduction of the current peak value; moreover we have to reduce also the energy transferred to the arc, responsible for the grids damage themselves. The solution includes an R–L impedance in series to the AGPS; this is provided in parallel by a clamp diode to avoid stored inductive energy to be transferred downstream. The grounded grid is connected to the inner screen through a damper resistor (DR) in order to limit the downstream capacitance energy effects. The resistor array RS contributes to limit arc energy as well: during transient because of high inductivity of the wire the current flows mainly on the screen rather than on the wire.

To achieve the target of limitation of the strong radiated electromagnetic noise due to fast transient current flowing on the TL it is necessary both to reduce the amplitude

of the current flowing on ground (common mode current) and its main frequency. The connection inside the high voltage deck HVD (the -100 kV polarized platform hosting all the power supplies for the Ion Source) is made by a 100 kV coaxial cable, covered by the outer screen OS (blue). Ringing common mode current flowing in the loop between AGPS and HVD is blocked by a core inductor (in massive blue in the picture), coaxial to the HV cable. The low magnetic coupling of outer screen OS, together with a relative low resistance (compared to earth) should allow that high-frequency return current flows mainly on this screen rather than on earth. This screen is connected to the vessel and to the screen surrounding the HVD; so it is the primary screen against EMI. It is connected in only one point to the inner (green) screen by the resistor array RS. Finally, to reduce the high-frequency ringing due to breakdown oscillations, along the HVS a number of slim high-permeability ferrite rings will be installed, acting as a distributed core snubber.

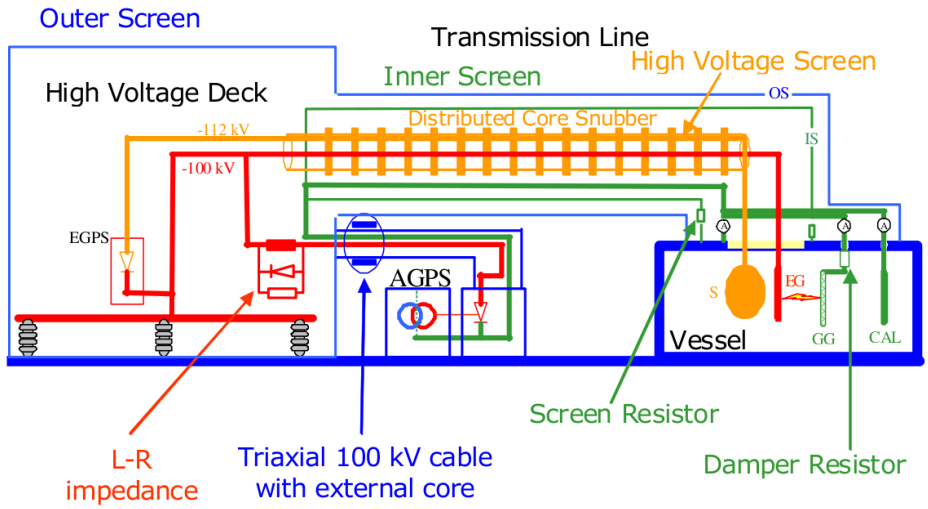

Figure 4.1: SPIDER conceptual design with protections integrated

4.2 Electrical circuit modeling

For the AGPS circuit implementation the power supply scheme of the Indian experiment SST-1 has been chosen [33]. It is constituted by a series of identical modules, each of them rated for about 1 kV and controlled independently. The configuration includes choppers on high voltage side. As stored energy on this side is very high (high value of input capacitance, almost 20 μF) the role played by the series switches (IGBT technology) is particularly important to limit the energy transferred downstream. In the analyses we considered a single stage equivalent to the series of all the modules, with one ideal switch with a prudential time switching equal to 5 μs.

The ~30 m multi-conductors TL is modeled as a series of 12 cells, 2.5 m each long, in order to consider propagation effects; all magnetic and capacitive couplings between

conductors were computed by finite elements code [26].

Due to its uncertainty the electrical arc is assumed as a normal voltage generator, i.e. a series of a constant voltage drop (100 mV) and a linear resistor (1 mΩ).

The tab. 4.1 summarizes the value of the parameters inserted in the equivalent circuit.

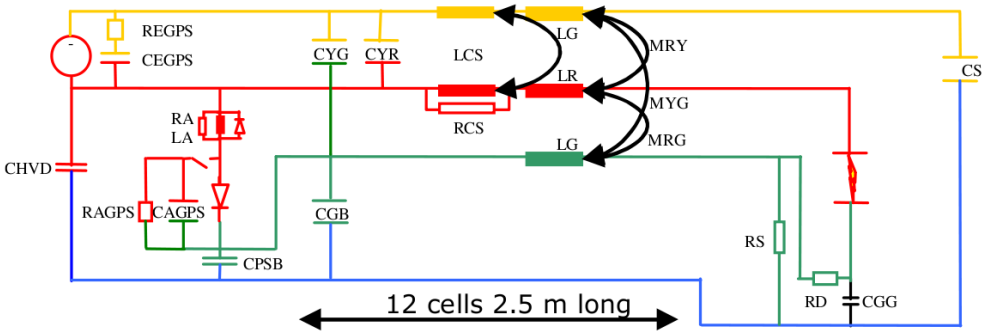

Figure 4.2: SPIDER model

A parametric study has been performed on the circuit to optimize the values of the passive elements introduced, considering the effects of breakdown. As indicators of arc damage the first and second peaks of breakdown current are considered, together with the energy transferred by arcing; for EMI the indicators are the peak of current flowing on the TL outer screen and its decay time (amplitude less than 50 A). Results are summarized in the tab. 4.2.

4.2.1 L–R input impedance

In fig. 4.3 the plot of current for different configuration of L–R impedance in series to AGPS shows the beneficial effect: being fixed the resistance R=500 Ω the best result is obtained with the inductance L=1 mH (black curve). This value is then chosen. Second current peak is strongly reduced, while first is almost unaffected. On the other hand in the first μs the current flowing on the outer screen OS (fig. 4.4) increases both in terms of peak and time length; however the adoption of the other components like damper and core snubber will be delivered also to limit this effect. Instead, after the AGPS switching intervention the overcurrent peak is moderately damped. Finally, in fig. 4.5 it is clear the strong effect of the L–R impedance on the arc energy deposition reduction (nearly by a factor 8).

4.2.2 Damping resistor

Current plotted in fig. 4.6 for different damper resistances shows the positive effect for all the indicators: both first and second current peaks are reduced, arc energy transferred by arc in the first ten microseconds (fig. 4.8) and OS current (fig. 4.7) are lowered as well.

Table 4.1: Electrical parameters for SPIDER circuital model

Name	Value	Description
CHVD	1 nF	High Voltage Deck capacitance to ground
CEGPS	1 μF	EGPS filter capacitance
REGPS	20 Ω	EGPS filter resistance
length	2.5 m	Cell length
n	2.5	Number of cores per cell
ncell	12	Total number of cells
RS	10 Ω	Resistor array IS–vessel
CGG	110 pF	Grounded grid capacitance to vessel
CSo	70 pF	Ion Source capacitance to vessel
LY	0.183 μH/m	Source conductor self-inductance
LR	0.98 μH/m	Extraction Grid conductor self-inductance
LG	0.017 μH/m	Inner Screen conductor self-inductance
MYR	0.183 μH/m	Source-Extr. Grid mutual inductance
MYG	0.019 μH/m	Source-Inner Scr. mutual inductance
MRG	0.019 μH/m	Extr. Grid-Inner Scr. mutual inductance
CYR	18.2 pF/m	Source-Extr. Grid capacitance
CYG	71.9 pF/m	Source-Inner Scr. capacitance
CGB	2550 pF/m	Inner Scr.-Outer Scr. capacitance
Rs1	0.22 mΩ/cell	Source conductor resistance per cell
Rs2	1 mΩ/cell	Extr. Grid conductor resistance per cell
Rs3	0.176 mΩ/cell	Inner Scr. conductor resistance per cell
RsGND	0.16 mΩ/cell	Outer Scr. resistance per cell
CPSB	5 nF	AGPS neutral point capacitance to ground
Lcable	2 μH	AGPS–TL cable inductance
Rcable	0.5 nF	AGPS–TL cable capacitance to neutral
RAGPS	50 kΩ	AGPS chopper resistance
CAGPS	20 μF	AGPS chopper capacitance
topen	5 μs	AGPS switching time
Rarc	1 mΩ	Arc model resistance
Earc	100 V	Arc model voltage drop
LA	10 μH – 1 mH	Snubber inductance between AGPS and TL
RA	500 Ω	Snubber resistance between AGPS and TL
CA	1 nF	Equivalent parallel capacitance of snubber L–R
RD	1 – 50 Ω	Damping resistance
LCS	1 – 10 μH/core	Inductance of magnetic cores
RCS	7 – 70 Ω/core	Equivalent parallel resistance of cores

Table 4.2: Summary of simulation results on SPIDER

L–R [μH-Ω]	DR [Ω]	DCS [μH-Ω]	1^{st} cur. pk [A]	2^{nd} cur. pk [A]	Tot. Arc En. [J]	Arc En. [J] @ 10 μs	OS cur. pk [A]	Decay [μs]
—	20	—	1200	4800	2.5	2.5	70	1.3
10-500	20	—	1200	4600	2.25	2.25	200	3
100-500	20	—	1200	2700	1.2	1.2	330	3.5
1000-500	20	—	1200	600	0.29	0.29	330	3
1000-500	—	—	1600	1000	0.69	0.35	420	7.5
1000-500	50	—	1000	500	0.23	0.23	270	2
1000-500	20	1.06–7.4	800	550	0.35	0.33	200	2.5
1000-500	20	10.6–74	400	450	0.75	0.33	100	2
1000-500	20	satur.	420	660	0.55	0.3	300	2.5

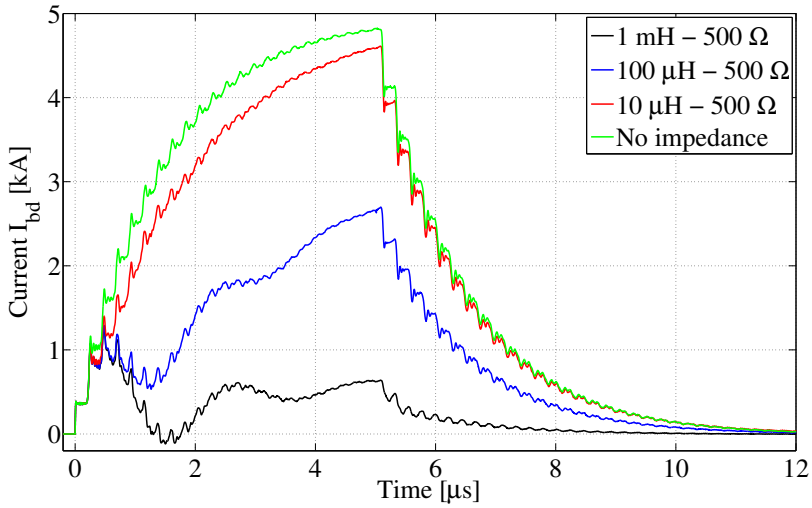

Figure 4.3: Effect of the L–R impedance on breakdown current

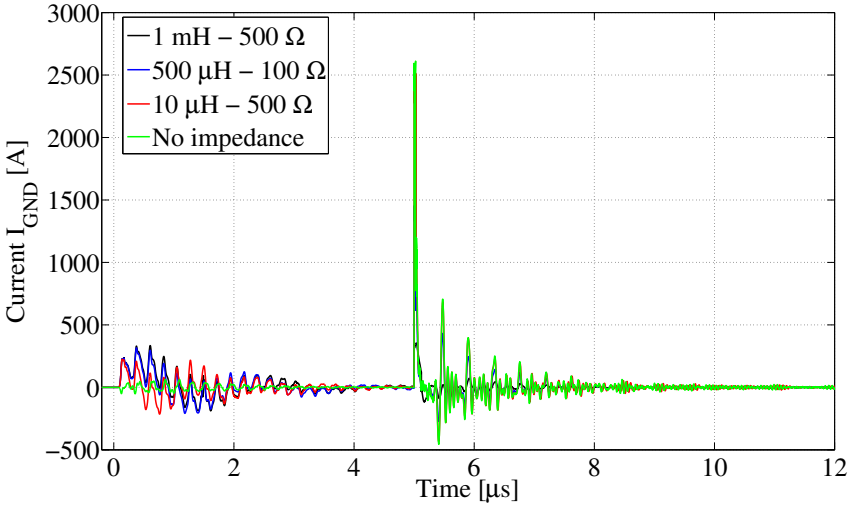

Figure 4.4: Effect of the L–R impedance on current flowing onto TL OS

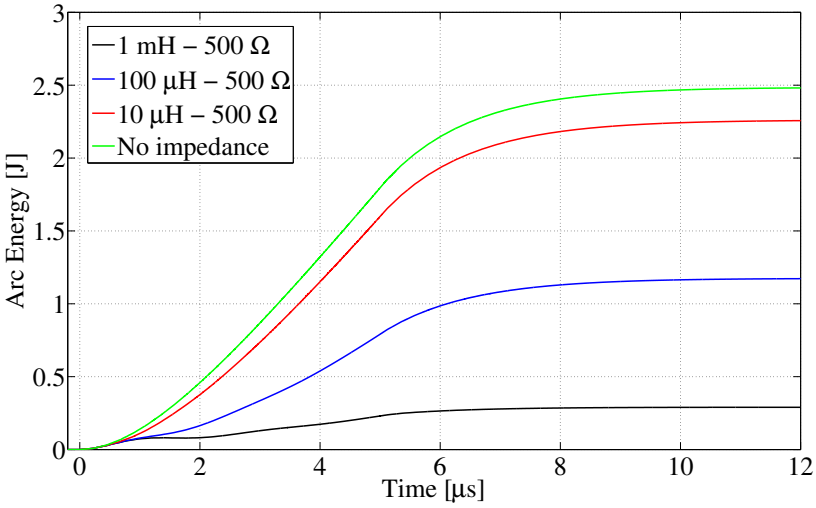

Figure 4.5: Effect of the L–R impedance on arc energy

However, the increasing of resistance enhances the voltage of the GG floating during breakdowns (fig. 4.9): from 3 kV with no DR it reaches 25 kV peak with 20 Ω and 50 kV with 50 Ω. Insulation problems can arise: an acceptable value of 20 Ω was then chosen. With such resistance, current peaks are limited below 1.3 kA, ground current within 350 A and energy is reduced up to 0.3 J.

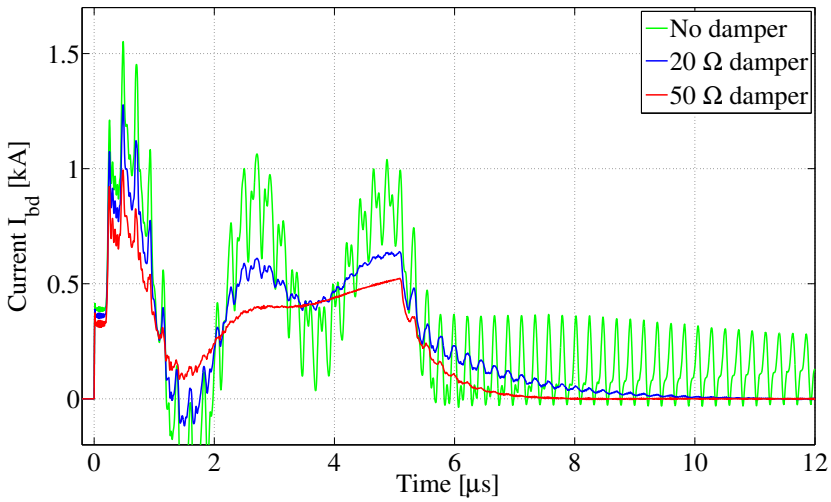

Figure 4.6: Effect of damper on breakdown current

4.2.3 Distributed Core Snubber

Finally, analyses have been carried out to study the effects of the DCS. Each core was modeled as an R–L parallel; parameters per unit length were calculated according to the paragraph 4.3.1. Two different lengths were considered in linear condition: 20 mm/core (1.06 μH–7.4 Ω) and 200 mm/core (10.6 μH–74 Ω). Results are shown in fig. 4.10, fig. 4.11, fig. 4.12. There is a positive effect in the reduction of breakdown current peaks; also OS current peaks are lowered, but the energy transferred is higher, as the higher value of TL inductivity increases the inductive stored energy and the transient time of breakdown current (up to 50 μs instead of 12 μs). However, before the first 10 μs the value of energy transferred is lower, so the effect of DCS is beneficial. Then, a further case considered the saturation characteristic of ferrite cores (for 200 mm length). When cores enter into saturation condition there's a peak for the external screen current (see red curve in fig. 4.11) and in a less severe way also for the breakdown current second peak. Also the total energy transferred is a bit higher, effect due to the strongest oscillations behaviour. In fig. 4.13 it is shown that with the saturating cores the value of flux near to saturation is reached faster than in the linear case, then we have a "flat" flux time (between 1 and 5 μs) in which cores operate near the fully saturated region; as a matter of fact, this is the region in which the behaviour is farther than linear condition (compare fig. 4.13 and fig. 4.10).

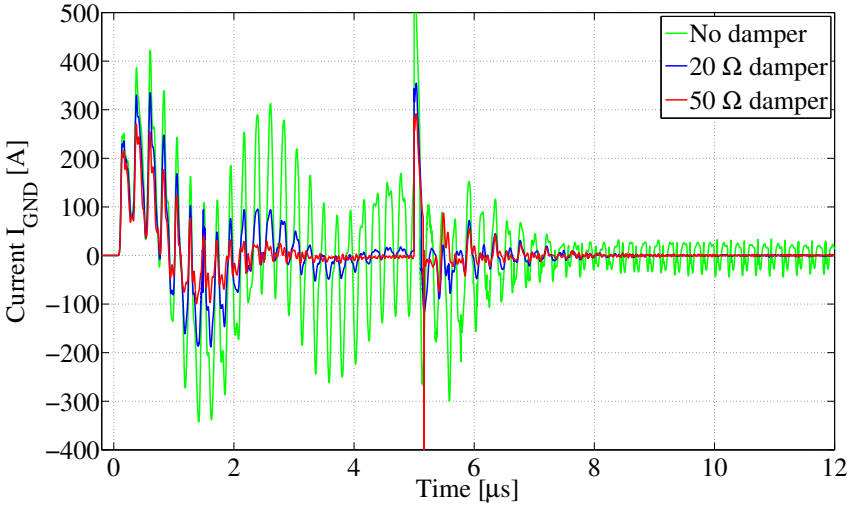

Figure 4.7: Effect of damper on current flowing onto TL OS

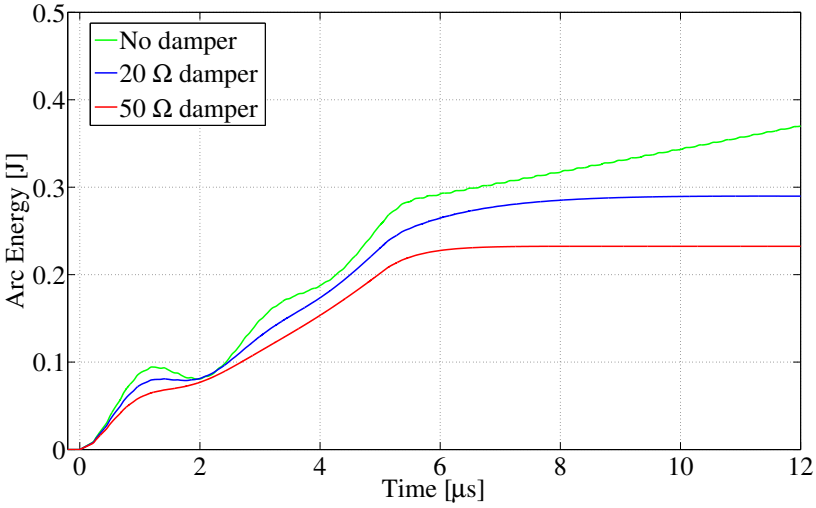

Figure 4.8: Effect of damper on arc energy

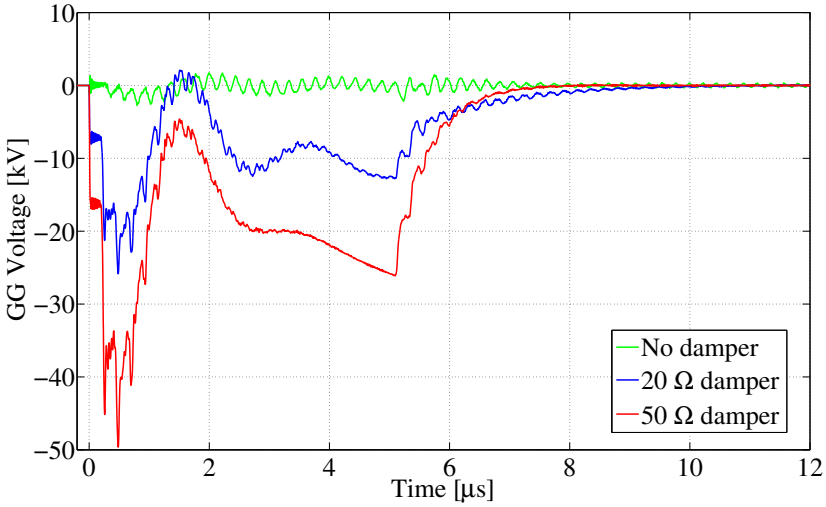

Figure 4.9: Effect of damper on grounded grid voltage

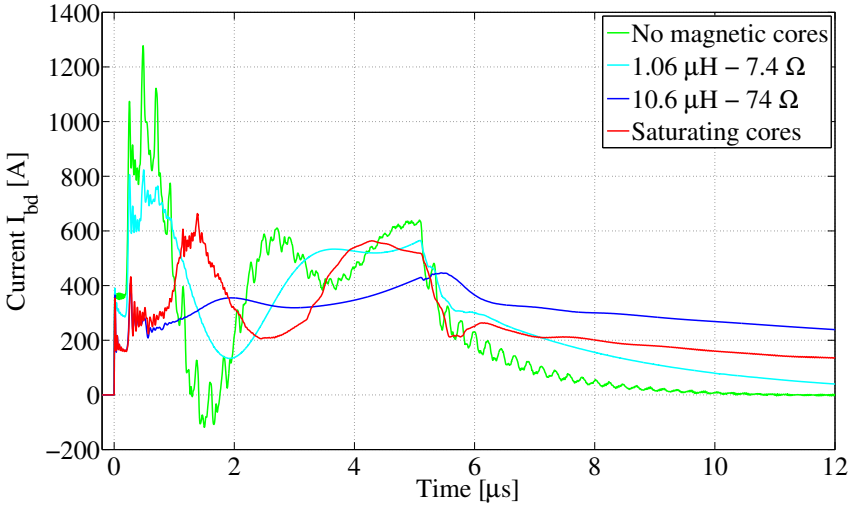

Figure 4.10: Effect of DCS on breakdown current

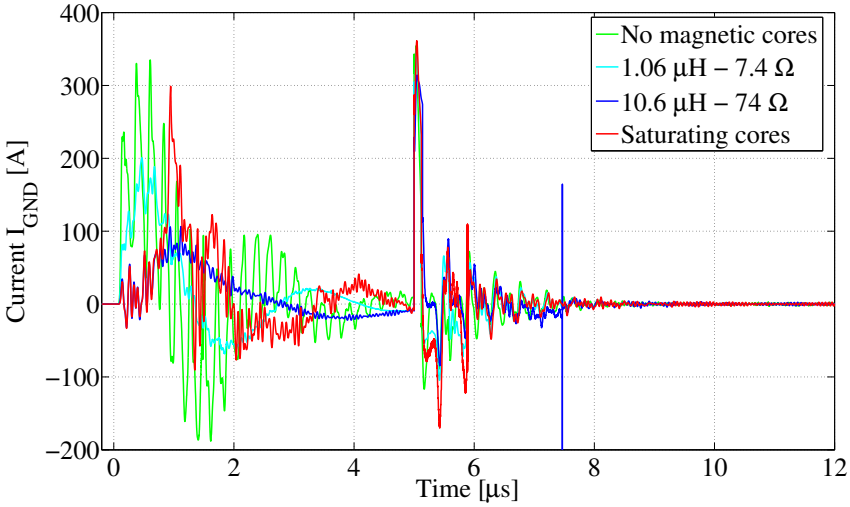

Figure 4.11: Effect of DCS on OS current

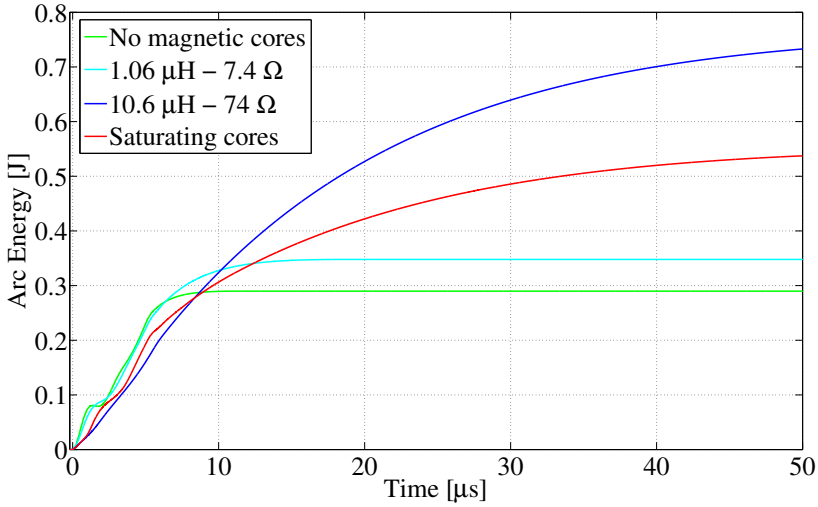

Figure 4.12: Effect of DCS on arc energy

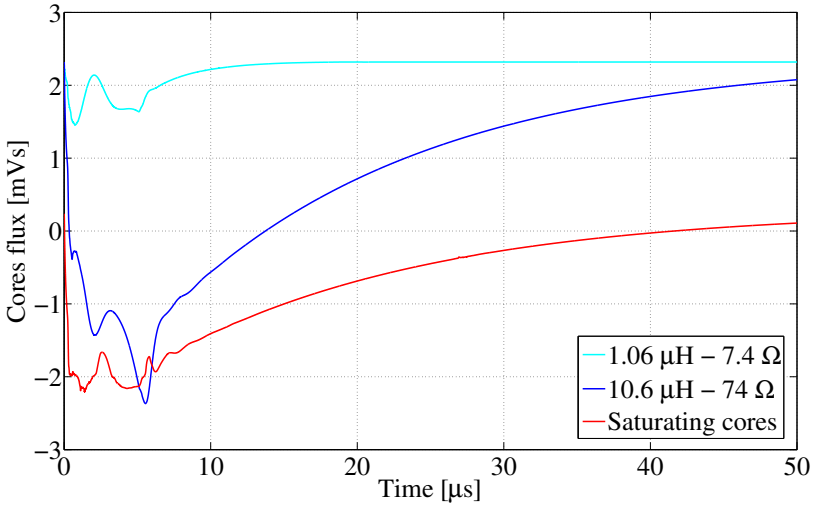

Figure 4.13: Last core of DCS flux swing

4.3 Distributed Core Snubber design

As we saw in the previous paragraph the main effect of the DCS solution is the limitation of high frequencies ringing due to the current and voltage oscillations after a breakdown. This phenomenon is responsible of the EMI effect and has to be strongly limited. This oscillations mitigation has also a positive effect on the reduction of energy transferred to the arc. On the base of the core data-sheet parameters the design description follows.

4.3.1 Magnetic cores

The material chosen to realize such cores is Metglas Finemet® [29], according to JADA experience developed for the concentrated core snubber [28, 3]. The required inductivity is approximately 10 μH/core, see 4.2.3. The core design is based on R–L parallel model, whilst the data-sheet reports the parameters referred to R–L series model. It is then necessary to proceed to the transformation according to [34]. In both core models, the equivalent inductance–resistance components are expressed as follows:

$$L_p = L_0 \cdot \mu'_p \qquad R_p = \omega \cdot L_0 \cdot \mu''_p \tag{4.1}$$

$$L_s = L_0 \cdot \mu'_s \qquad R_s = \omega \cdot L_0 \cdot \mu''_s \tag{4.2}$$

where L_0 is the inductance considered with unit permeability (air equivalent), ω is the pulsation corresponding to the frequency, and μ' and μ'' are respectively the real and imaginary permeability. Being ℓ the length of the core L_0 is evaluated as:

$$L_0 = \frac{\mu_0}{2\pi} \ln\left(\frac{r_2}{r_1}\right) \cdot \ell \tag{4.3}$$

where r_1 and r_2 are respectively the inner and outer radii of the core. In order to have the same equivalent impedance, the merit factor Q is the same for both series and parallel models, i.e.:

$$\frac{\mu_p''}{\mu_p'} = \frac{R_p}{\omega L_p} = Q = \frac{\omega L_s}{R_s} = \frac{\mu_s'}{\mu_s''}$$

This implies

$$R_p = R_s \cdot (Q^2 + 1) \quad \text{and} \quad L_p = L_s \cdot \left(1 + \frac{1}{Q^2}\right)$$

Thus the transformation for the complex permeability is:

$$\begin{aligned} \mu_p'' &= \mu_s'' \left(1 + \frac{\mu_s'^2}{\mu_s''^2}\right) \\ \mu_p' &= \mu_s' \left(1 + \frac{\mu_s''^2}{\mu_s'^2}\right) \end{aligned} \tag{4.4}$$

At the frequency foreseen for the oscillations after a breakdown (approximately 4 MHz) we obtain the following values of real and imaginary parts of equivalent series complex permeability (see fig. 4.14):

$$\mu_s' = 500 \qquad \mu_s'' = 1800$$

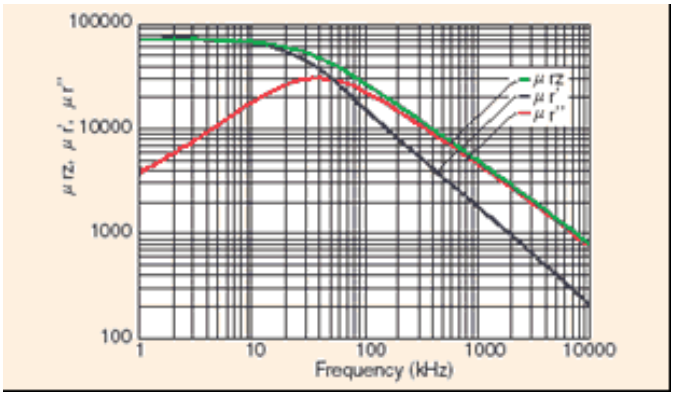

Figure 4.14: Permeability vs. frequency for Finemet cores [35]

Substituting in 4.4 we obtain (at 4 MHz):

$$\mu_p' = 7000 \quad \text{and} \quad \mu_p'' = 1950$$

Chosen radii are $r_1 = 260$ mm, inner diameter corresponding to the -112 kV screen of the transmission line plus an insulating support thickness, and $r_2 = 270$ mm, outer diameter considering a thickness of the cores equal to 10 mm. Substituting in 4.3 these parameters we obtain an inductance $L_0 = 7.55\ [\text{nH/m}] \cdot \ell$ and then in 4.1 obtaining:

$$L_p = 52.8\ [\mu\text{H/m}] \cdot \ell \quad \text{and} \quad R = 370\ [\Omega/\text{m}] \cdot \ell$$

Finally we can calculate the cores width to have the required value of inductance. In order to reach 10 μH per core this value should be $\ell = 200$ mm. Thus final parameters become:

$$\begin{aligned} L_p &= 10.6\ \mu\text{H} \\ R_p &= 74\ \Omega \end{aligned}$$

For a 30 m transmission line length we have 30 cores, so 1 core per meter.

4.3.2 Biasing circuit

As in the normal operation an equivalent negative current of ∼60 A flows in the TL, cores are polarized at a certain level of flux. The saturation magnetic flux density is $B_{sat} = 1.2$ T, according to the core data-sheet. The total saturation flux for all the cores is then:

$$\Phi_{sat} = B_{sat} \cdot \ln\left(\frac{r_{ext}}{r_{int}}\right) \cdot r_{int} \cdot \ell \tag{4.5}$$

Substituting the value we obtain $\Phi_{sat} = 70.6$ mWb. The saturation current, i.e. the maximum current corresponding to the value of saturation flux is computed from the dc core inductivity, as follows:

$$L_{dc} = \frac{\mu_0 \mu_r}{2\pi} \ln\left(\frac{r_{ext}}{r_{int}}\right) \cdot \ell \tag{4.6}$$

The value is $L_{dc} = 3.2$ mH. So the saturation current is:

$$I_{sat} = \frac{\Phi_{sat}}{L_{dc}} = 22\ \text{A}\ < 60\ \text{A}$$

The cores during breakdown would be fully saturated. Thus we need to install a depolarizing resetting circuit.

Simulations show that the flux swing is -140 mWb. If the cores are counter-biased to the limit of (positive) saturation (70 mWb), the cores operate inside the non saturation area, as shown in fig. 4.15. In fig. 4.16 the situation for the last core (the closest to the breakdown) is also shown: also in this case the core, if positively polarized, remains unsaturated.

To obtain a 70 mVs positive polarization, a circuit linked to the cores has to be provided, delivering a current: $I_{pol} = 60 + 22 = 82$ A. We can install then a power supply capable to provide 100 A – 50 V, in order to assure suitable margin. This power supply will be connected to the transmission line outer conductor potential (-112 kV). Such power supply must be protected against the overvoltage induced into the counter-biasing circuit during breakdown: in fact, the biasing system is strongly coupled with the transmission line by the cores. The proposed solution is the realization of a distributed blocking inductivity, in series to the counter-biasing circuit, which will sustain the induced voltage.

As the last section of the TL is the most stressed by the breakdown we chose this as a constraint for the protection design. The overvoltage peak value on this section is about 18.5 kV (see fig. 4.17).

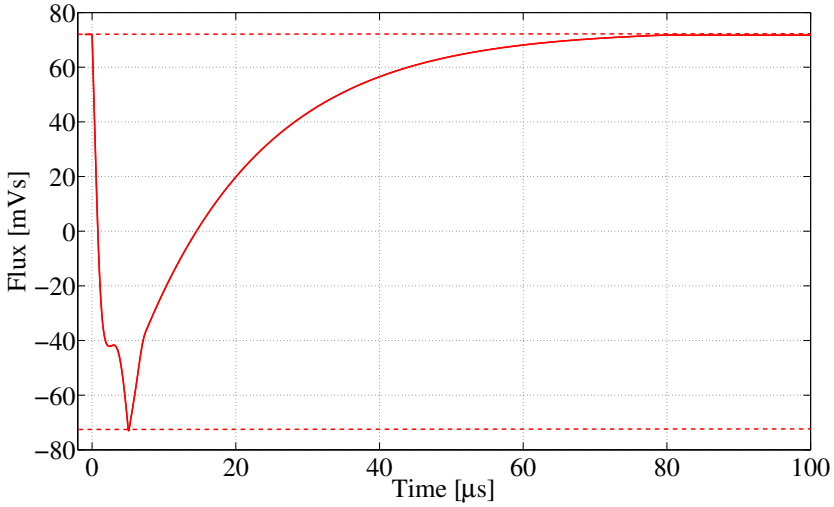

Figure 4.15: Flux swing on the overall transmission line

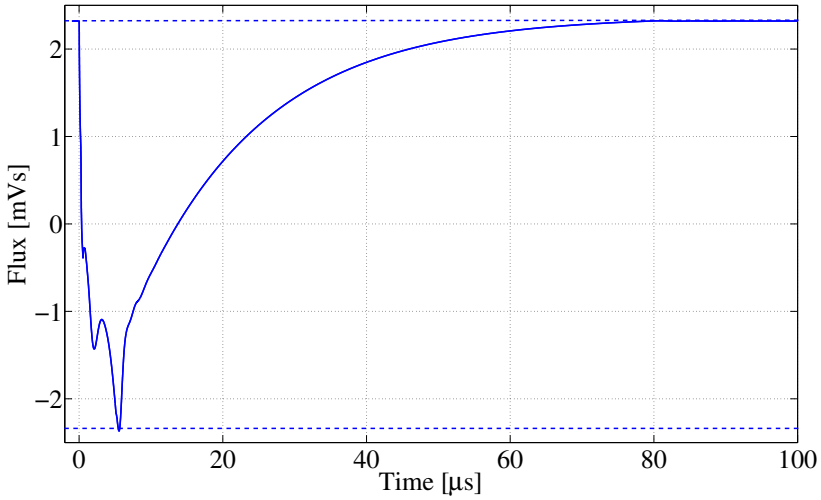

Figure 4.16: Flux swing in the last section of the TL

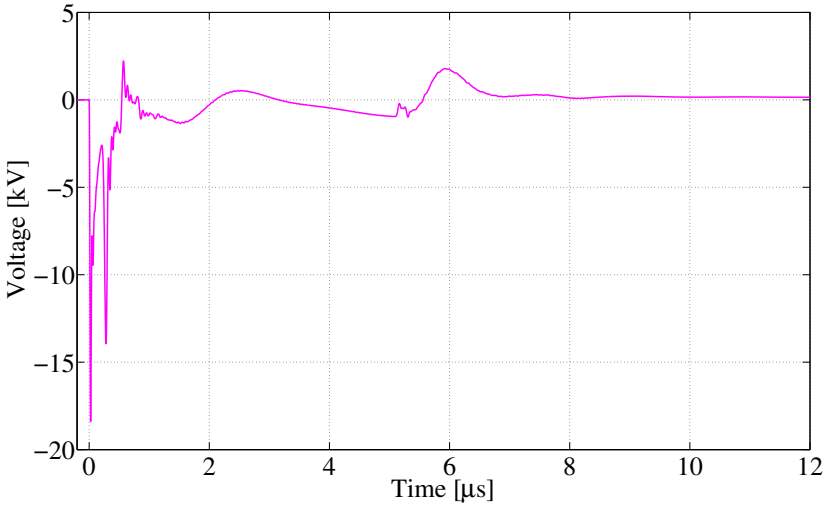

Figure 4.17: Transient voltage on the last section of the TL

An air inductance is associated to each core. Referring to fig. 4.16 and fig. 4.17 the inductance requested by the last core is calculated as follows, assuming a perfect coupling (1:1 ratio) between core and counter-biasing circuit:

$$i = I_0 + \int_0^t \frac{v}{L} dt < 0 \text{ always.} \tag{4.7}$$

Rearranging, we obtain the minimum inductance value as:

$$I_0 > \frac{1}{L} \int_0^\infty d\phi \Rightarrow L > \frac{\phi_{max} - \phi_0}{I_0} = \frac{2\Phi_{sat}}{I_0} \tag{4.8}$$

which value is $L > 57$ μH.

A possible solution proposed is to make the conductor of the resetting circuit doing some turns around the TL between two sections and above each magnetic core. The scheme is shown in fig. 4.18. In such way, the flux produced by this current is not linked with the TL, acting as a lumped inductance. We calculate the numbers of turns requested for each coil, assuming a 12.5 x 3.35 mm strap, using the short solenoid formulas, with r_0 major radius of the coil, p the width of the strap and $\ell = Np$ the length of the solenoid. The factor α due to the shortness of the solenoid is evaluated as:

$$\alpha = \sqrt{1 + \frac{1}{4 \cdot (Np/2r_0)^2}} - \frac{1}{2 \cdot (Np/2r_0)} \tag{4.9}$$

Then the inductance can be evaluated from:

$$L_{coil} = \alpha \cdot \frac{\mu_0 \cdot N^2 \cdot S}{\ell} = \alpha \cdot \frac{4\pi \cdot 10^{-7} \cdot N \cdot (\pi \cdot r_0^2)}{p} \tag{4.10}$$

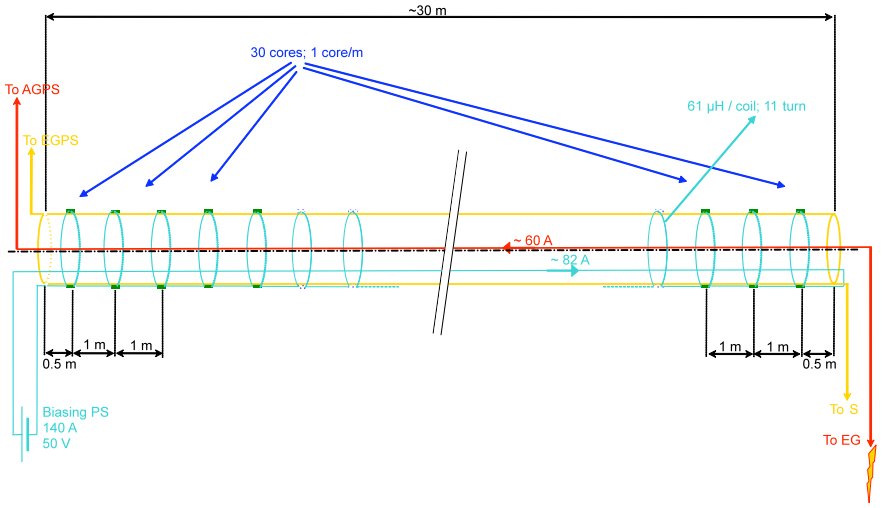

Figure 4.18: Scheme of the distributed core snubber system equipped with the biasing circuit

Substituting $N = 11$, $p = 12.5$ mm, $r_0 = 272$ mm we obtain $\alpha = 0.238$ and finally the inductance $L_{coil} = 61$ μH. This value is acceptable in comparison with the value estimated by 4.8. An additional inductivity of approximately 1 μH/m has to be applied due to the longitudinal current component.

Thus, the overall inductance of the resetting circuit is equal to 1.86 mH. A tentative layout of the structure combining core and blocking inductance is shown in fig. 4.19. In green the insulating support is shown, in blue the magnetic core and in orange the strap conductor wrapped into 11 turns and welded at both ends with the straps or bars which connect to the next core biasing. The return conductor of the biasing circuit is installed inside the TL in a proper slot and realized by an insulated cable.

4.3.2.1 Protection circuit

During the operation, SPIDER accelerator current will range between zero current and the nominal value (~60 A). Thus, if the current is below this value we have to reduce also the value of the biasing circuit current in order to maintain the cores at the positive saturation flux. In any case, in order to keep under control the overvoltages across the biasing power supply in case of forced current reversal, the solution proposed in fig. 4.20 is presented; two passive components are installed at the power supply terminal: a series diode to block the negative current and a parallel protective resistor to quickly damp the inverse current and to protect the power supply against overvoltages. A reasonable value for such a resistor is approximately 10 Ω.

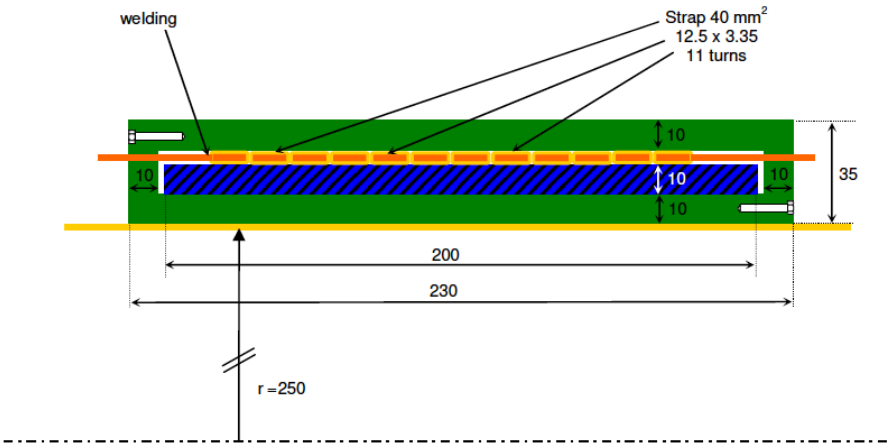

Figure 4.19: Sketch of the installation of the cores on the TL

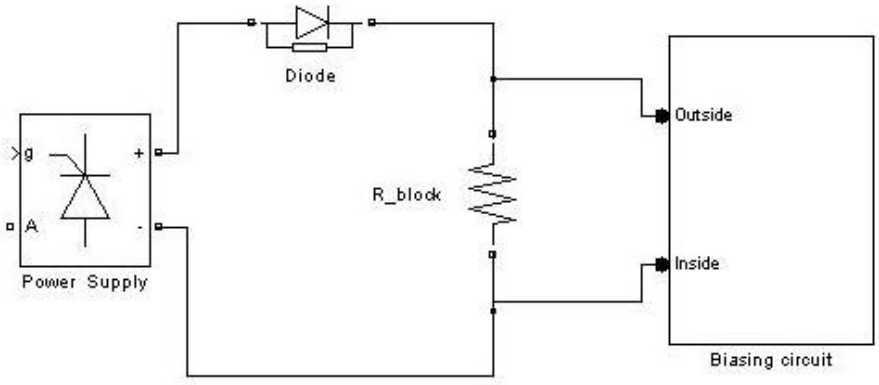

Figure 4.20: Scheme of the protection circuit against overvoltage for the core snubber biasing circuit

Conclusions

This doctoral thesis, whose related activity is inserted in the framework of the research for the ITER Neutral Beam Injection system, underlined that the electrical performances requested to the high voltage power supply system of the injector are very demanding. Hence, to avoid the degradation of voltage holding properties, the mitigation of the effects due to the unavoidable breakdowns between the accelerating grids is a crucial topic for the feasibility and reliability of the whole system. Also the limitation of electromagnetic noise has a straightforward importance.

Present solutions appear not to be completely suitable to pursue this target, as they are partially effective to limit the arc energy, which seems to be the most important electrical quantity to limit. Therefore, here some new conceptual solutions were proposed and analyzed. Their impact on the overall system was also studied with the implementation of proper circuital models.

In particular, a damping resistor was analyzed, designed and assembled. An experimental campaign was settled at the CEA Megavolt test bed in Cadarache (France) to study its effect and effectiveness. This campaign has been supported by a detailed circuit modeling which needs to be validated. It should also help the study of a proper circuital model for the long gap arc in vacuum.

The other concept, the distributed core snubber, was studied and validated in an experimental campaign on a small-scale example.

Finally both the devices were integrated in the design of the new experiment being built in Padova, i.e. a ITER NBI full-scale negative ion source. Results from simulations on equivalent circuit demonstrate their positive effect on the system. This work helped to write part of the technical specification for the experiment.

List of Figures

List of Tables

Acknowledgements

At the end of this Ph.D. there are some people I would like to thank.

First, I am glad to my tutor Antonio De Lorenzi to have helped me during these years and encouraged my research activities.

I wish to thank also all the other Ph.D. students and young researchers at Consorzio RFX, to have spent a lot of time sharing serious discussions and joking chats.

Then, I am especially grateful to my parents, to have supported my choice to undertake a Ph.D. three years ago.

Finally, I wish to give a dedication to my wife, with whom I has just started a new, exciting and wonderful story.

Bibliography

[1] EFDA, www.efda.org.

[2] ITER organization, www.iter.org.

[3] K. Watanabe et al., *Development of a dc 1 MV power supply technology for NB injectors*, IOP Nucl. Fus. **46** (2006), 332–339.

[4] A. De Lorenzi et al., *The insulation structure of the 1 MV transmission line for the ITER neutral beam injector*, Proc. of the 24th Symp. on Fus. Techn., vol. 82, October 2007, pp. 836–844.

[5] A. De Lorenzi, L. Grando, A. Pesce, P. Bettini, and R. Specogna, *Modeling of epoxy resin spacers for the 1 MV dc gas insulated line of ITER neutral beam injector system*, IEEE Trans. on Dielectrics and Electrical Insulation **16** (2009), 77–87.

[6] P. Sonato et al., *The ITER full size plasma source device design*, Proc. of the 25th Symp. on Fus. Techn., vol. 84, June 2009, pp. 269–274.

[7] H.M. Owren, W.R. Baker, K.H Berkner, D.B. Hopkins, and D.J. Massoletti, *The effect of capacitive stored energy of neutral beam accelerator performance*, Proc. of the 12th Symp. on Fus. Techn., September 1982, pp. 455–460.

[8] F. Bottiglioni and J.P. Bussac, *Energetic breakdowns and voltage hold-off between copper electrodes in vacuum*, Physica 104C (1981), 248–255.

[9] A. Masiello, A. De Lorenzi, L. Grando, and L. Svensson, *Critical issues of HV dc vacuum and pressurized gas environments for the ITER NB injector*, Proc. of the 24th Symp. on Fus. Techn., vol. 82, October 2007, pp. 819–828.

[10] L. Cranberg, *The initiation of electrical breakdown in vacuum*, J. of Appl. Phys. **23** (1952), no. 1, 518–522.

[11] F.M. Charbonnier, *A brief review of vacuum breakdown initiation process*, Proc. of the 3rd Int. Symp. on Discharges and Electrical Insulation in Vacuum, September 1968, pp. 15–34.

[12] P. Spolaore, G. Bisoffi, F. Cervellera, R. Pengo, and F. Scarpa, *The large gap case for HV insulation in vacuum*, IEEE Trans. on Dielectrics and Electrical Insulation **4** (1997), no. 4, 389–393.

[13] K. Watanabe et al., *dc voltage holding experiments of vacuum gap for high-energy ion sources*, J. of Appl. Phys. **72** (1992), no. 9, 3949–3956.

[14] P. Massmann et al., *Voltage holding and dark currents in the Cadarache 1 MV Ion Beam facility*, Proc. of 20th ISDEIV (Tours, France), 2002.

[15] A. Krylov and R. S. Hemsworth, *Gas flow and related beam losses in the ITER neutral beam injector*, Fus. Eng. and Des. **81** (2006), no. 19, 2239–2248.

[16] M. Bonin, *Modello circuitale d'arco per la simulazione del fenomeno di scarica nell'iniettore di neutri di ITER*, Degree thesis, Electrical Engineering Department, University of Padova, 2007, (in Italian).

[17] J. Reece Roth, *Industrial plasma engineering*, vol. 1, IoP, Bristol, UK, 1995.

[18] T. E. Browne, *The electric arc as a circuit element*, Journ. of Electrochemical Society **102** (1955), no. 1, 27–37.

[19] O. Morimiya, S. Sohma, T. Sugawara, and H. Mizutani, *High current vacuum arcs stabilized by axial magnetic fields*, IEEE Trans. on Power App. and Systems. **92** (1973), 1723–1732.

[20] R. Claesen and P. L. Mondino, *Jet Project – neutral beam injection and radio-frequency power supplies*, Fusion technol. **11** (1987), no. 1, 141–162.

[21] D. C. Edwards et al., *Commissioning and operation of 130 kV/130 A switched-mode HV power supplies with the upgraded JET neutral beam injectors*, Proc. of the 23th Symp. on Fus. Techn., vol. 75-79, November 2005, pp. 41–47.

[22] J. A. Carwardine, G. Pile, and T. E. Zinneman, *Management of High Current Transients in the CWDD Injector 200 kV Power System*, Proc. of the 1995 Part. Accel. Conf., vol. 2, May 1995, pp. 1242–1244.

[23] J.H. Fink, W.R. Baker, and H.M. Owren, *Analysis and application of a transformer core that acts as an arc snubber*, IEEE Trans. on Plasma Science **8** (1980), no. 1, 33–38.

[24] M. Bigi, V. Toigo, and L. Zanotto, *Protections against grid breakdowns in ITER neutral beam injector power supplies*, Proc. of the 24th Symp. on Fus. Techn., vol. 82, October 2007, pp. 905–911.

[25] K. Watanabe et al., *Design of a -1 MV dc UHV power supply for ITER NBI*, IOP Nucl. Fus. **49** (2009), no. 5, 55022 (5 pp.).

[26] M. Bigi, A. De Lorenzi, L. Grando, K. Watanabe, and M. Yamamoto, *A model for fast transient analyses of the ITER NBI power supplies and the MAMuG accelerator*, Proc. of the 25th Symp. on Fus. Techn., vol. 84, June 2009, pp. 446–450.

[27] H. Helgesen, *The voltage distribution and related problems in a magnetic core snubber during transients*, Tech. report, Internal JET report JDN/G 152, 1981.

[28] K. Watanabe et al., *Development of a high performance core snubber for high power neutral beam injectors*, Rev. of sc. instrum. **69** (1998), no. 12, 4136–4141.

[29] S. Nakajima et al., *Fe-based nanocrystalline FINEMET cores for induction accelerators*, Nucl. Instr. and Met. in Phys. Res. sect. A **331** (1993), 318–322.

[30] A. Pesce, A. De Lorenzi, and L. Grando, *A new approach to passive protections against high energy and high current breakdowns in the ITER NBI accelerator*, Proc. of the 25th Symp. on Fus. Techn., vol. 84, June 2009, pp. 1499–1504.

[31] W. Rigato et al., *Vessel design and interfaces development for the 1 MV ITER neutral beam injector and test facility*, Proc. of the 25th Symp. on Fus. Techn., vol. 84, June 2009, pp. 1606–1610.

[32] HVR international®, www.hvrint.com.

[33] U.K. Baruah et al., *Power supply system for 1000S Neutral Beam Injector*, 17th IEEE/NPSS Symp. on Fus. Eng., vol. 2, October 1997, pp. 1133–1136.

[34] J.K. Watson, *Using parallel complex permeability for ferrite chracterization*, IEEE Trans. on Magnetics **25** (1989), no. 5, 4224–4226.

[35] Hitachi Metglas®, www.metglas.com.